A Study on Quantitative Evaluation of Local Permittivity and Conductivity Using Microwave Atomic Force Microscope

Department of Mechanical Science and Engineering

Nagoya University

Bo Tong

Contents

Contents I
Chapter 1 Introduction 1
1.1 History and Developing Prospect of Atomic Force Microscopy 1
1.2 Basic Working Principles of Atomic Force Microscopy 2
1.2.1 Contact Mode 2
1.2.2 Tapping Mode 4
1.2.3 Non-contact Mode 5
1.3 Atomic Force Microscopy Combined with Electrical Property Measurement Techniques 6
1.3.1 Functional AFM for Electrical Property Measurement 7
1.3.2 Scanning Microwave Microscopy (SMM) 8
1.4 Achievements and Challenges of Microwave Atomic Force Microscopy (M-AFM) 12
1.4.1 Design, Assembling, and Principle of Microwave Atomic Force Microscopy 12
1.4.2 Scanning Microwave Image and Quantitative Evaluation of Conductivity of Bulk Metallic Materials 15
1.4.3 Challenges of Microwave Atomic Force Microscopy 16
1.5 Research Objective 17
1.6 Organization of Thesis 18
Reference 20

Chapter 2 Introduction 29
2.1 Fabrication of Slit Probe and Coaxial Probe 29
2.2 Evaluation of Slit Probe and Coaxial Probe 34
2.3 Measurement Approach for Dielectric Materials and Metallic Materials 36
Reference 39

Chapter 3 Local Permittivity Measurement of Dielectric Materials Based on Non-contact Force Curve of M-AFM.....40
3.1 Introduction.....40
3.2 Experimental Approach.....40
3.2.1 Examination of M-AFM Probe.....40
3.2.2 Force Curve Measurement.....41
3.3 Establishment of Theoretical Model under Near-field Condition.....43
3.3.1 Near-field Incident Wave and Reflected Wave.....43
3.3.2 Coulomb Interaction between Probe and Sample.....47
3.4 Quantitative Evaluation of Permittivity of Dielectric Materials.....50
3.5 Summary.....56
Reference.....57

Chapter 4 Non-contact Local Conductivity Measurement of Metallic Nanowires Based on Semi-near-field Reflection of M-AFM.....58
4.1 Introduction.....58
4.2 Experimental Approach.....58
4.3 Semi-near-field Model for Description of Reflected Microwave.....59
4.3.1 Reflection from Strips and the Substrate.....59
4.3.2 Reflection from Nanowire Sample and Evaluation of Conductivity.....63
4.4 Evaluation of Metallic Nanowire Conductivity.....67
4.4.1 Anomaly of Aluminum Nanowire.....67
4.4.2 Quantitative Evaluation Results.....71
4.5 Summary.....74
Reference.....75

Chapter 5 Theoretical Analysis and Simulation of Near-Field Microwave Distribution for M-AFM Probes.....76
5.1 Problems of Plane Wave Model and Necessity of Simulation.....76
5.2 Theoretical Analysis and Modeling.....77

5.2.1 Theoretical Model....77
5.2.2 Simulation Principle and Modelling for Probes....79
5.3 Electric Field Distribution in Absence of a Sample....83
5.3.1 Simulation Results of Slit Probe....83
5.3.2 Simulation Results of Coaxial Probe....87
5.4 Discussion for Microwave Emission Capability and Resolution....91
5.4.1 Size of Aperture....91
5.4.2 Thickness of Inner Conductor of Coaxial Probe....96
5.4.3 Length of Inner Conductor of Coaxial Probe....98
5.4.4 Comparison between Slit Probe and Coaxial Probe....101
5.5 Electric Field Distribution with Dielectric Samples and Sample Permittivity Dependence....101
5.5.1 Different Sample Property Dependence between Near Field Model and Plane Wave Model....101
5.5.2 Results of Electric Field Distribution with Dielectric Sample....103
5.6 Summary....109
Reference....110

Chapter 6 Conclusions....111
Acknowledgements....114

Chapter 1 Introduction

1.1 History and Developing Prospect of Atomic Force Microscopy

Scanning probe techniques, such as scanning tunneling microscopy (STM), scanning force microscopy (SFM), scanning near-field optical microscopy (SNOM) and scanning electrochemical microscopy (SECM), are effective evaluation methods for surface property characterization which have been applied to nanomaterials and biological materials [1-18]. Among these scanning probe instruments, atomic force microscopy (AFM) was invented in 1985 by G. Binnig, C. F. Quate and Ch. Gerber [19] and since then it has become one of the most important scanning probe microscopes giving birth to many outstanding and enlightening researches on nanoscale surface imaging [20-36]. Since the atomic force exists universally between all materials, AFM can be used to evaluate a wide class of samples including insulators and metals. By contrast, scanning tunneling microscopy (STM) and scanning electron microscopy (SEM) rely on the conductivity of the sample and cannot work for insulator samples. What is more, AFM does not always work under vacuum, which make it possible to be applied to evaluate biological samples in liquid environment [37-40]. The superiorities of AFM also contains no surface preparation, various evaluation modes and real nanoscale or even atomic/molecular scale resolution. All of these advantages have made AFM an ideal evaluation system to integrate with other evaluation techniques. In recent decades, the development of nanotechnology, surface science and molecular biology demands more multifunctional evaluation methods with a resolution of nanoscale, which has stimulated the attempt aiming at the accomplishment of various AFM based measurement systems, such as atomic force microscopy and surface-enhanced Raman spectroscopy (AFM-SERS) for chemical identification [41-43], magnetic exchange force microscopy

(MExFM) for ferromagnetism domain detection [44-46] and electrostatic force microscopy (EFM) for surface electrical potential [47-52]. Since electrical properties are the most significant characteristics related to the work functions of nanomaterials, the evaluation of electrical properties such as permittivity, conductivity and free electron concentration has attracted most attention. Besides EFM, typical instruments including conducting atomic force microscopy (C-AFM) [53,54], scanning capacity microscopy (SCM) [55,56], Kelvin-probe force microscopy (KPFM) [57,58], scanning spreading resistance microscopy (SSRM) [59,60], microwave impedance microscopy (MIM) [61-63] and near-field scanning microwave microscopy (NSMM/SMM) [64-68] have been designed and developed. All these works have implied that the integration and mutual assistance of different measurement techniques represents one of the most promising development directions of AFM and scanning probe technique.

1.2 Basic Working Principles of Atomic Force Microscopy

1.2.1 Contact Mode

As mentioned in the above section, AFM has various working modes. Classifying by scanning condition, these modes include contact mode, tapping mode and non-contact mode. Contact mode is the most direct and common mode to detect the topography of the sample surface [69-73]. In this mode, the tip scans without oscillation and hence contact mode is also called static mode. The deflection of the tip while scanning, which is detected by the laser beam reflected from the cantilever, is used as the feedback signal in a DC feedback amplifier. The feedback amplifier controls the piezoelectric sensor to modulate the vertical position of the sample holder stage according to the variation of the cantilever deflection. The voltage signal applied to the stage by the feedback amplifier is also recorded to imply the height of the sample surface, in which method the topography of the sample surface can be described. Since the tip is in close contact

with the sample surface while regular scanning, the total force on the tip is repulsive with a mean value of 10^{-9} N (see Fig. 1-1). Under ambient conditions, other forces are also applied to the sample besides the atomic force. Usually sample surfaces are covered by a meniscus layer of adsorbed water vapor and nitrogen which forms a surface tension toward the sample surface. Moreover, for semiconductor and insulator materials, electrostatic forces caused by trapped static charges also exist between the probe and sample. Experimentally, these forces can be reduced by liquid environment or vacuum to achieve a better resolution. However, an unavoidable problem of contact mode is that the normal force used for evaluation creates a frictional force which is far more destructive than the normal force especially at the boundary of a bump. It can wear both the sample and the tip and thus distort the scanning result. Attempts to avoid this problem are tapping mode and non-contact mode.

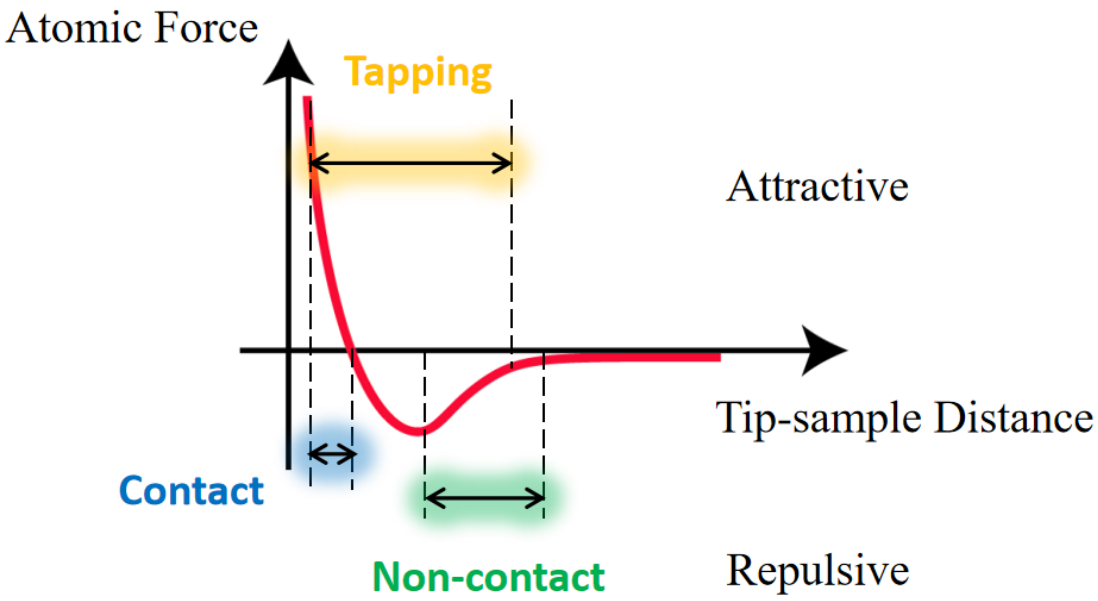

Figure 1-1: The distance dependence curve of atomic force and the corresponding working region on the curve of AFM in contact mode, tapping mode and non-contact mode.

1.2.2 Tapping Mode

Tapping mode has been a key advance for AFM to evaluate sensitive and unstable surfaces such as biological materials or small particles [74-80]. It is named tapping mode because the tip alternatively touching and lifting off from the surface of the sample at or near the cantilever's resonant frequency during scanning. Therefore, tapping mode is also called dynamic mode or intermittent contact mode and works in the intermediate region of attractive force and repulsive force (see Fig. 1-1). The oscillation of the cantilever is driven by a piezoelectric crystal and the amplitude and frequency are detected by the laser signal reflected from the cantilever, which is used for the feedback control of piezoelectric crystal. The amplitude of cantilever is over 20nm and the frequency of cantilever is from 50 kHz to 500 kHz before the tip approach the sample surface. When the measurement starts, the cantilever contacts with the surface, which reduces the oscillation because of energy loss. During the scanning, when the tip scans a bump, the amplitude of oscillation decreases, otherwise the amplitude increases when the tip meets a depression. Then the feedback loop modulate the height of sample stage to recover the amplitude and the force between the tip and sample. Therefore, tapping mode is also called amplitude modulation mode. Compared to contact mode, tapping mode has an amplitude high enough to reduce the effect of tip-sample adhesion forces. The high frequency of lifting the tip is also enough to ensure the force is vertical and thus eliminate the shear friction force to protect the tip and the sample. For the same reason, tapping mode is more stable on rough surfaces and can be applied to fragile or soft surfaces and loose films on substrate. Compared to non-contact mode, the interacting force is stronger to resist the noise and therefore the resolution is better in ambient environment. In addition, the shift between the phase signal of cantilever oscillation and the piezoelectric actuator can be recorded, which can be used to evaluate the softness of the sample material.

1.2.3 Non-contact Mode

The first topography scanning image with atomic resolution in non-contact mode was obtained on Si (111)-(7×7) surface in ultra-high vacuum (UHV) in 1995 by F. J. Giessibl [81]. In non-contact mode, the cantilever vibrates over the surface of sample at its resonant frequency and a very low amplitude within 2 nm and never touches the surface of sample. The distance between the tip and sample is about 10 nm and the interacting force between the tip and sample is attractive van der Waals forces (see Fig. 1-1). In the tuning step before measurement, the cantilever is driven by the piezoelectric crystal to vibrate at its resonant frequency f_0. The small amplitude vibration of the cantilever can be regarded as a harmonic vibration, therefore, f_0 can be described as

$$f_0 = \frac{1}{2\pi}\sqrt{\frac{k}{m}}, \tag{1-1}$$

where k is the spring constant of the cantilever and m is the equivalent mass of the cantilever, respectively. When the tip approaches the sample surface, the attractive van der Waals forces applied on the tip impacts both the amplitude and the frequency of the vibration. Usually, the bias of frequency is detected by the laser beam and used as feedback signals. Thus this mode is also called frequency modulation (FM) mode. The resonant frequency of cantilever near the sample is

$$f_0 + \Delta f = \frac{1}{2\pi}\sqrt{\frac{k + \mathrm{d}F/\mathrm{d}z}{m}}, \tag{1-2}$$

where Δf, F and z are the frequency bias, van der Waals force and tip-sample distance, respectively. Since the spring constant is much greater than the gradient of the van der Waals force, Eq. (1-2) can be approximated as

$$\frac{\Delta f}{f_0} = -\frac{1}{2k}\frac{\mathrm{d}F}{\mathrm{d}z}. \tag{1-3}$$

The gradient of van der Waals force depends on the distance to the sample, however, it can be considered to be constant within one amplitude of several nanometers. Therefore, by detecting the variation of the resonant frequency Δf, the variation of van der Waals force and distance can be detected. The topography of sample surface can be obtained during scanning by modulate the vertical level of sample stage to recover Δf to be zero. Non-contact mode was developed since it can relieve the risk of scratch damage to the sample and degradation of the tip. The probe of non-contact AFM completely works under the attractive regime of atomic force, which is more harmless than tapping mode especially for fragile materials. Moreover, it has the superiority of less chemical interaction and contaminant delivery between the tip and the reactive sample surface. However, a deficiency of non-contact mode is that van der Walls force is substantially weaker than the interaction force of contact mode or tapping mode. It makes the non-contact mode sensitive to the fluid contaminant layer and the surface tension, which has confined the application of the non-contact mode. In recent decades, non-contact mode AFM has achieved plenty of outstanding progresses [82-84] such as three-dimensional atomic force microscopy [85-87], atomic resolution image in liquids [88,89] and magnetic exchange force microscopy [44-46]. All of these efforts have greatly expanded the function and versatility of non-contact mode AFM.

1.3 Atomic Force Microscopy Combined with Electrical Property Measurement Techniques

Electrical property is one of the most valuable properties of functional materials. Especially for nanomaterials, the electrical property usually determines their sensitivity as nano-sensors or the Joule heat which affecting their performance as nano-devices. Therefore, the research on measurement method and instrument for electrical property

at nanoscale has always been attractive in the past few decades. If traditional evaluation method is applied to nanomaterials, such as four-probe method for conductivity [14-16], it would be inefficient due to the fabrication of tiny electrodes and the manipulation for electrical contact with sample. Alternatively, AFM based metrology instruments have been demonstrated to be effective to provide rapid characterization scanning images.

1.3.1 Functional AFM for Electrical Property Measurement

In the early stage, many works which attempted to expand AFM to electrical property measurement mainly focused on the direct voltage or low frequency alternating voltage condition. Among these works, electrostatic force microscopy (EFM) is the most popular one [47-52]. Using a conductive AFM probe and substrate, bias voltage can be applied between the probe and the sample, which may generate an additional electrostatic force between the tip and the sample besides the atomic force. This force variation can be detected by AFM and then converted to the capacitance of tip-sample system. Although the sample permittivity can be obtained from the capacitance, it is extracted from the electrical property of the tip-sample system instead of measuring the intrinsic value directly. Kelvin probe force microscopy (KPFM) is another functional AFM measuring electrical property based on electrostatic force [57,58]. In KPFM, the electrical property is not evaluated from additional electrostatic force directly. Instead, a bias voltage is applied between the tip and sample to generate an electrostatic force, which can offset the force due to contact potential difference. From this voltage the work function of the sample surface can be evaluated. Other similar works include conductive AFM (C-AFM), scanning spreading resistance microscopy (SSRM) and scanning capacitance microscopy (SCM) [53-56,59,60]. C-AFM and SSRM measure the tunnel current from the conductive AFM tip to the sample. From the I-V curve, C-AFM can evaluate the surface potential, namely the Schottky potential of semiconductors, and SSRM can evaluate the local carrier concentration of the materials. SCM, on the other hand, measures the gradient of capacitance with alternating voltage

of the tip-sample system. The concentration of carriers in the semiconductor sample can be evaluated. These methods usually needs contact mode or tapping mode based on their measurement mechanism, especially for C-AFM and SSRM, loading force is necessary to guarantee the perfect electrical contact for current measurement. This may cause scratch for soft or fragile surface. Also, it is usually difficult for these methods to measure the intrinsic permittivity or conductivity of the sample itself, since the bias voltage is applied for the whole tip-sample system.

1.3.2 Scanning Microwave Microscopy (SMM)

Scanning microwave microscopy (SMM) is the first attempt to implement AFM based electrical property measurement at a frequency of microwave band. It can operate in the range above 1 GHz and obtain the image of the impedance between the conductive AFM probe and sample. Combining the electrostatic force measurement with the impedance, the local changes of various materials properties such as dopant profiling, permittivity and conductivity can be evaluated [64-68]. The designs of different SMMs mainly contain two types, one of which is resonator SMM and the other is transmission line SMM. The resonator SMM works at a fixed frequency which depends on the geometry of the resonator cavity. The change of the sample electrical property will change the reflected signal and thus will be detected through the bias of the resonant frequency and quality factor. By simply monitoring the off-resonant response near the maximum slope of the response curve, these systems are sensitive to small changes. On the other hand, the transmission line SMM is composed of an AFM and a vector network analyzer (VNA). Comparing to the resonator SMM, transmission line SMM can work in a wide range of frequency from 1 GHz to 20 GHz and thus is considered to have wider application and be more promising.

The schematic of transmission line SMM is shown as Fig. 1-2. Besides the basic function of AFM, the VNA of transmission line SMM can apply a microwave signal to the tip of a metallic probe and detect the scattering parameter S_{11} between sample and

probe. The relationship between the impedance of the sample Z_S and the measured scattering parameter $S_{11,m}$ can be described as

$$S_{11,m} = e_{00} + e_{01}\frac{S_{11,a}}{1-e_{11}S_{11,a}}, \tag{1-4}$$

and

$$S_{11,a} = \frac{Z_S - Z_V}{Z_S + Z_V}. \tag{1-5}$$

Here, Z_V is the impedance of the VNA which is known and $S_{11,a}$ is the realistic value of S_{11}, respectively. e_{00}, e_{01} and e_{11} are three complex parameters which can be determined by calibration. In calibration, the electrostatic force F_e between the tip and the sample is measured versus the tip-sample distance z. The force has a relationship with the capacitance C between the tip and the sample as

$$F_e(z) = \frac{1}{4}\frac{\mathrm{d}C(z)}{\mathrm{d}z}V_0^2\cos(2\omega t), \tag{1-6}$$

where V_0 and ω are the amplitude and frequency of the microwave signal, respectively. On the other hand, the capacitance C determines the impedance Z_S as

$$Z_S(z) = \frac{1}{i\omega C(z)}. \tag{1-7}$$

In this way, the dependence of impedance Z_S on the tip-sample distance z can be obtained from Eqs. (1-6) and (1-7). Therefore, by simultaneously measuring the approach curves of $S_{11,m}(z)$ and $F_e(z)$ of a calibration material, e_{00}, e_{01} and e_{11} can be determined by fitting Eqs. (1-4) and (1-5). On the contrary, when evaluating the

permittivity of a sample, the measurement result of $S_{11,m}$ image can be converted to the capacitance between the sample and the tip using these equations. The capacitance is composed of three parts, which are the capacitance between the apex and the sample, the capacitance between the cone and the sample, and the stray capacitance (see Fig. 1-2). They can be represented as

$$C_{\text{apex}}(z) = \frac{2\pi\varepsilon_r R}{\left(\log\left(\tan\frac{\theta}{2}\right)\right)^2}\log\frac{h+\varepsilon_r z}{h+\varepsilon_r(R+z)-\varepsilon_r R\sin\theta}, \tag{1-8}$$

$$C_{\text{cone}}(z) = \frac{2\pi\varepsilon_r}{\left(\log\left(\tan\frac{\theta}{2}\right)\right)^2}\times\left(z\log\frac{H\varepsilon_r}{h+z\varepsilon_r+R\varepsilon_r(1-\sin\theta)}-\right.$$
$$\left.\frac{1}{\varepsilon_r}\left(\frac{h}{\varepsilon_r}+R\left(1-\sin\frac{1}{\theta}\right)\right)\times\log\left(\frac{h}{\varepsilon_r}+z+R(1-\sin\theta)\right)\right) \tag{1-9}$$

and

$$C_{stray}(z) = c_{stray}z + c\,, \tag{1-10}$$

respectively. Here, R, θ and H are the curvature radius of the apex, aperture angle of the cone and the height of the cone, respectively. h and ε_r are the thickness and the permittivity of the sample. c_{stray} is the slope of the stray capacitance. By fitting the approaching curve of the capacitance $C(z) = C_{\text{apex}} + C_{\text{cone}} + C_{\text{stray}}$ at a certain point on the sample surface to be evaluated, R, c_{stray} and ε_r can be obtained. Finally, the capacitance image converted from the measured $S_{11,m}$ image can be further converted to the permittivity image of the sample, and the quantitative imaging of permittivity is realized.

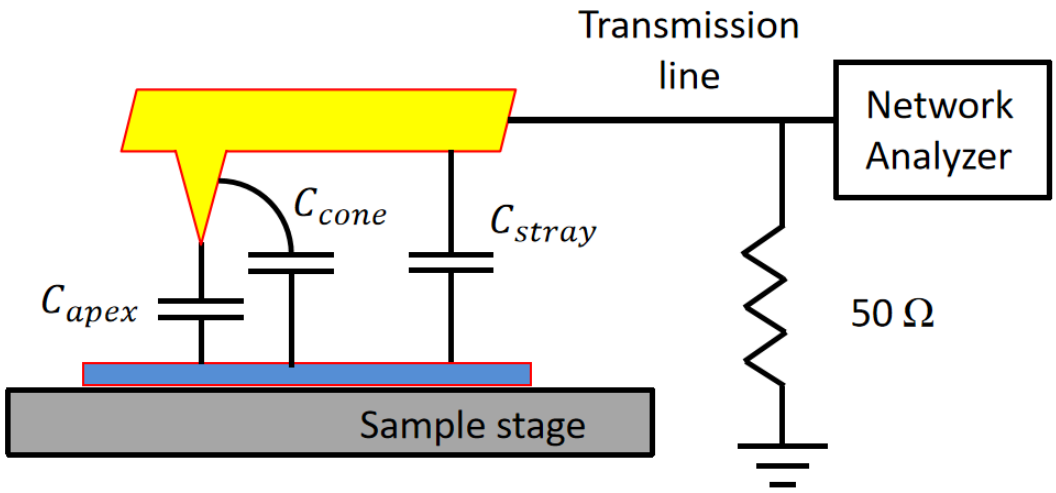

Figure 1-2: The schematic of transmission line SMM

Another development is to apply SMM to tapping mode, which can reduce the contact between the tip and sample [61-63]. Besides the contact damage, measurement under contact mode usually induces large scale of noise. The measured impedance becomes a relative value as shown by Eq. (1-4) due to the process to alleviate the noise. The long-winded technique of SMM to extract the quantitative information and the critical components for quantitative determination are also sensitive to the environment variation caused by the tip-sample contact during long time scale scanning. MIM, however, can detect the absolute value of the impedance between the tip and the sample by the distance modulation and demodulation of the microwave signal measure while probe tapping. The electronic drifts and other environmental variation during the scanning also do not impact the quantitative imaging since the tapping frequency or amplitude of the cantilever is modulated constantly while scanning and detecting. In their further work, the quartz tuning fork oscillator with a metallic wire tip stick to the prong was introduced for the tapping system, which can provide lower loss for microwave transmission at ultra-low temperature. It does not need the razor feedback to modulate the tapping, which simplifies the structure and gives MIM better compatibility. What is more, since the dissipation of the tuning fork oscillation is monotonic versus the tip-sample distance, the modulation can still remain stable even when the roughness of

the sample surface is comparable to the amplitude of the probe. By analyzing the imaginary part and the real part of the scanned tip-sample impedance image, the permittivity image and the conductivity image of the sample can be obtained.

1.4 Achievements and Challenges of Microwave Atomic Force Microscopy

1.4.1 Design, Assembling, and Principle of Microwave Atomic Force Microscopy

Although quantitative evaluation of local electrical properties can be achieved by SMM under contact mode (non-contact quantitative evaluation needs contact calibration) and tapping mode, non-contact quantitative evaluation is still indispensable for the materials which are sensitive to the pollution or the chemical interaction caused by the contaminant on the probe. Also, since the probes cannot emit microwave by itself, the measurement relies on the probe-sample system, rather than only the intrinsic property of the sample. Actually, microwave measurement technique itself was proved to be an effective non-contact and non-destructive measurement method in the field of bulk material electrical property evaluation [90-92]. It can provide the electrical information of the materials in a various range of frequency region through the reflection signal at the surface, which is more competitive than direct current measurement. Therefore, it is believed to have the potential to couple with the highly compatible AFM and to realize thorough quantitative non-contact evaluation of intrinsic sample electrical properties at nanoscale.

For this purpose, microwave atomic force microscopy (M-AFM) was first designed by combining a w-band microwave system and non-contact AFM by Ju and his team [93-99]. A novel probe for M-AFM, which can emit microwave by itself without the

help of a sample, was designed and fabricated. It is essential for the measurement to get rid of the dependence on tip-sample system. The schematic of the probe and the microwave system is as shown by Fig. 1-3. The gold films covered on both sides of the probe serve as a homogeneous parallel plate condenser wave guide. A silt-like structure across the gold film at the tip apex of the probe is fabricated as the aperture of microwave. It is connected to the wave guide and microwave system by an exposed coaxial cable on the probe holder. In the microwave system, a microwave signal with a frequency of 16.67 GHz is first produced by a generator. Then the microwave signal transmits through a six-time frequency multiplier and the frequency of the output signal is extended to 94 GHz. The extended microwave signal propagates into an isolator and a circulator. The isolator protects the input signal and the circulator can separate the reflection signal. After that the microwave signal is emitted at the aperture of the M-AFM probe by the parallel plate structure. When a sample is placed under the tip, the microwave reflected by the sample surface transmits back to the M-AFM probe and the circulator. The reflection signal separated by the circulator is finally received by a detector. The output voltage of the detector is used to create the microwave image corresponding to the position information recorded by the AFM scanner.

In measurement, the distance between the tip of M-AFM probe and the sample is controlled to be constant by the feedback system during scanning, which is named as standoff distance. Therefore, reflection of microwave is not affected by the probe-sample distance. The only variable that affects the reflection is the reflection coefficient of the sample. If the power of the microwave emitted at the tip of the probe remains constant, the reflection microwave is proportional to Γ, the reflection coefficient of the sample. On the other hand, the power of the microwave emitted at the tip is evaluated to be around -20 dBm, which indicates that the diode detector works in a small signal range. In this case, the output voltage V_1 of the diode detector is determined by the square of the input voltage V_0 as

$$V_1 = k_0 |V_0|^2 + b_0 . \tag{1-11}$$

Here, the two unknown parameters k_0 and b_0 are performance constants of the detector. They can be determined by the calibration using two samples with known conductivity. Since V_1 is proportional to Γ as explained above, Eq. (1-11) can be rewritten as

$$V_1 = k_0 \left|\Gamma\right|^2 + b_0 . \tag{1-12}$$

For good conductors, Γ only depends on the conductivity σ of the sample as

$$\left|\Gamma\right| = \left| \frac{1-\sqrt{\sigma \,/\, j\omega\varepsilon_0}}{1+\sqrt{\sigma \,/\, j\omega\varepsilon_0}} \right|, \tag{1-13}$$

where ε_0, ω, and j are the permittivity of free space, angular frequency of the microwave signal and the imaginary unit, respectively. According to Eq. (1-13), the conductivity of sample can be finally determined as

$$\sigma = \omega\varepsilon_0 \frac{4\left|\Gamma\right|^2 - \left(\left|\Gamma\right|^2 + 1\right)^2}{\left(\left|\Gamma\right|^2 + 1\right)\sqrt{4\left|\Gamma\right|^2 - \left(\left|\Gamma\right|^2 - 1\right)^2} - 4\left|\Gamma\right|^2}. \tag{1-14}$$

For dielectric or isolating materials, the permittivity can also be evaluated using a similar process. The only unknown parameters to be calibrated in this evaluation method are k_0 and b_0, which can be obtained using two samples with known conductivity.

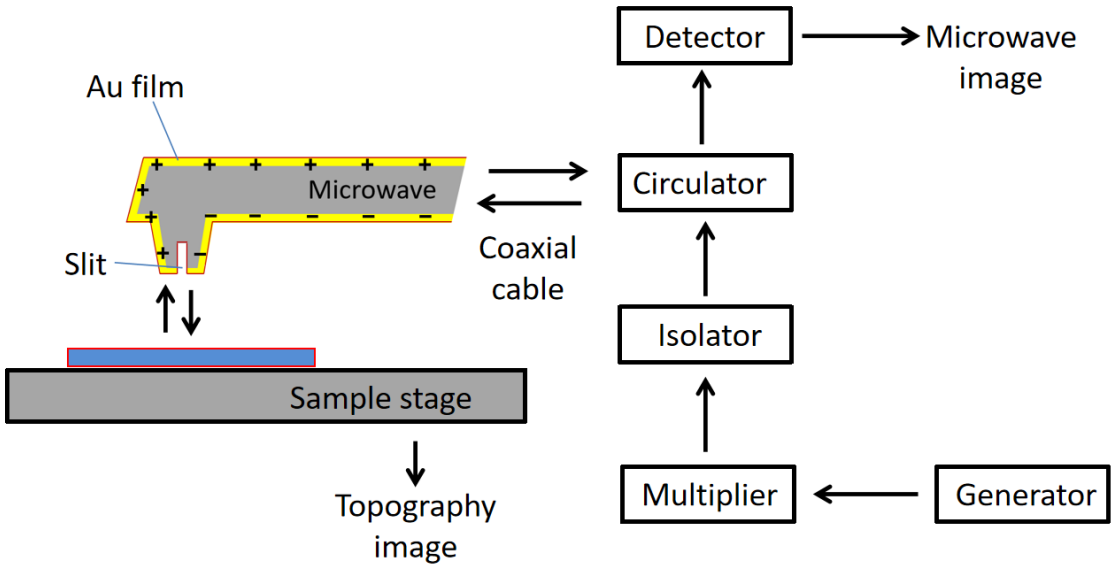

Figure 1-3: The schematic of the slit probe and reformed microwave system of M-AFM

1.4.2 Scanning Microwave Image and Quantitative Evaluation of Conductivity of Bulk Metallic Materials

In the initial work, characterization of topography and electrical property of different materials was achieved by M-AFM [95]. A sample of glass substrate with 200 nm thick gold film was fabricated by photolithography and electron beam (EB) evaporation. The two images were measured simultaneously within one scanning and the two results were consistent with each other. It demonstrates the ability of the M-AFM probe to emit microwave and also demonstrates that M-AFM can distinguish different materials by microwave. From the profile section data of the two images, the spatial resolution of the M-AFM probe is approximately to be 120 nm.

The quantitative evaluation of conductivities of several metallic materials were also achieved by M-AFM in non-contact mode by L. Zhang in 2011 [96]. According to Eqs. (1-12) and (1-14) in the above section, the local conductivities of cobalt, zinc, and

aluminum slabs were calculated from the reflection signal voltage extracted from the microwave image. The calibration materials were copper and lead. The error of the evaluated results were 7.24%, 2.03%, and 11.6% for cobalt, zinc, and aluminum, respectively. It demonstrates that for bulk metallic materials, M-AFM can evaluated the local conductivity in a relatively high accuracy even though the calculation model is based on plane wave approximation.

1.4.3 Challenges of Microwave Atomic Force Microscopy

Although M-AFM has successfully realized the non-contact quantitative local conductivity evaluation of bulk metallic materials, there still exists some non-negligible challenges before we could expand the application of M-AFM to semiconductor or nanomaterials. Firstly, the distance between the sample and probe (standoff distance) vastly impacts the intensity of microwave applied on the sample and received by the tip. For M-AFM, the microwave between the tip of probe and sample induces a new electromagnetic force. The variation of local electrical property may affect this force and thus affects the standoff distance. For metallic materials, this effect is not obvious because all metals have a reflection coefficient close to 1. However, for insulator and dielectric materials, the reflection coefficients have a wider range, which makes the standoff distance more different and thus impacts the received reflection signal. Another problem is that, for samples with various shapes such as nanowire samples with different diameters, the microwave spatial distribution between the tip and sample no longer remains constant. The intensity of the reflection signal also depends on the shape of the sample. In these cases, the plane wave model is not enough to describe the microwave distribution between the tip and the sample and a more refined near field model is expected. Therefore, a study on the tip- sample interaction becomes necessary for the development of M-AFM.

1.5 Research Objective

The author of this thesis aimed at expanding the application of M-AFM and improving the theoretical framework of measurement method. For this purpose, a near-field model describing the electrical field distribution of microwave between the tip and sample surface needs to be established first. Using this near-field model, the mechanism of the effect of microwave on the force interaction between the tip and sample can be further discussed. The next target of this thesis is to quantitatively describe its dependence on the tip-sample distance. Based on this effect, the author will try to develop a new method for the quantitative evaluation of permittivity of dielectric and insulator materials, which would not suffer from a variation of the standoff distance.

Another issue in this thesis is about the evaluation of metallic nanowire samples. If the evaluated sample is not flat, the spatial distribution of the microwave between the tip and sample also depends on the shape of the sample surface. Therefore, the goal is to discuss the reflected wave of metallic nanowire based on both the law of reflection and the near-field approximation, and thereby establish a theoretical model including the diameter of the nanowire for the evaluation of nanowire samples.

Finally, as the theoretical basis of this thesis, the near-field distribution of microwave between the tip and the sample surface need to be demonstrated. Since it is difficult to measure the electrical field distribution near the tip and inside the sample in experiment, which only exists within a nano-scale space, it will be investigated adequately using finite element method (FEM) simulation. The simulation result is expected to provide reliable evidence for the quantitative evaluation as well as for the fabrication and improvement of the probe.

1.6 Organization of Thesis

The rest contents of this thesis are organized as follows.

Chapter 2 is about the experiment approach of this thesis. The fabrication of two kinds of M-AFM probes using photo lithography, electron beam (EB) evaporation and focus ion beam (FIB) etching were introduced, and their performances were compared. It was explained that the two probes were used for dielectric materials and metallic materials, respectively, due to their features. The most suitable measurement modes of dielectric materials and metallic materials were also discussed.

In Chapter 3 the development of a quantitative evaluation method for insulator materials was reported. The electrical interaction caused by microwave was analyzed and an analytical expression was derived for quantitative evaluation. In experiment, the force curves of Si, Al_2O_3, Ge and ZrO_2 with and without microwave were measured under non-contact mode. The variation of force caused by microwave was extracted and the local permittivity of these materials were quantitatively determined based on the analytical expressions.

In Chapter 4, on the other hand, the quantitative evaluation method for conductivity was improved for metallic nanowire samples based on a semi-near-field model. Firstly, the reason that thorough near field model is not effective for metallic materials was explained. Therefore, a semi-near-field model combining the law of reflection and near field approximation was set up as the improvement of traditional plane wave model. Then the non-contact microwave image of Al, Ag and Cu nanowire were measured on a Pt substrate with Au strips, which was designed to contribute to calibration and thus make it possible to achieve the evaluation within one scanning. Similarly, we also demonstrated that the quantitative evaluation of conductivity of metallic nanowires were successfully realized using semi-near-field model.

Chapter 5 mainly focused on the simulation study of the field distribution of M-AFM probes using finite element method (FEM). In order to describe the field distribution of the microwave between probe and sample, a refined model with near field approximation was put forward. Based on this theoretical model, the incident waves

emitted from a slit probe and a coaxial probe were calculated and compared to their simulation results to verify the near-filed model. In addition, the effect of structure parameters of the two probes on microwave emission were also studied by FEM simulation in order to determine the optimal design of the probes. To demonstrate the rationality of near field model for quantitative evaluation, the slit probe was simulated with different dielectric samples, and the results were found to correspond to near field model rather than plane wave model.

Finally, in Chapter 6 we summarize the work of this thesis and give the conclusions.

References

1) G. Friedbacher, and F. Harald. Classification of scanning probe microscopies. *Pure Appl. Chem.* **71**, 1337-1357 (1999).
2) G. Binnig, H. Rohrer, Ch. Gerber, and E. Weibel. Surface studies by scanning tunneling microscopy. *Phys. Rev. Lett.* **49**, 57–61 (1982).
3) D. A. Bonnell. Scanning Tunneling Microscopy and Spectroscopy, Theory, Techniques and Applications. *VCH Publishers Inc, New York* (1993).
4) Ph. Avouris, and I.-W. Lyo. Probing and inducing surface chemistry on the atomic scale using the STM. *AIP Conf. Proc.* **241**, 283–297 (1992).
5) S. F. Alvarado. Tunneling potential barrier dependence of electron spin polarization. *Phys. Rev. Lett.* **75**, 513–516 (1995).
6) R. Möller, S. Akari, C. Baur, B. Koslowski, and K. Dransfeld. Scanning tunneling microscopy and photons. *AIP Conf. Proc.* **241**, 314–327 (1992).
7) T. Sakurai, T. Hashizume, Y. Hasegawa, I. Kamiya, N. Sano, K. Yokoyama, H. Tanaka, I. Sumita, and S. Hyodo. New versatile room–temperature fifield ion scanning tunneling microscopy. *J. Vac. Sci. Technol.* **A8**, 324–326 (1990).
8) D. Anselmetti, M. Dreier, R. Lüthi, T. Richmond, E. Meyer, J. Frommer, and H.-J. Güntherodt. Biological materials studied with dynamic force microscopy. *J. Vac. Sci. Technol.* **B12**, 1500–1503 (1994).
9) R. Lüthi, E. Meyer, L. Howald, H. Haefke, D. Anselmetti, M. Dreier, M. Ru¨etschi, T. Bonner, R. M. Overney, J. Frommer, and H.-J. Güntherodt. Progress in noncontact dynamic force microscopy. *J. Vac. Sci. Technol.* **B12**, 1673–1676 (1994).
10) M. Dreier, D. Anselmetti, T. Richmond, U. Dammer, and H.-J. Gu¨ntherodt. Dynamic force microscopy in liquids. *J. Appl. Phys.* **76**, 5095–5098 (1994).
11) D. Sarid. Scanning Force Microscopy. *Oxford University Press, New York* (1991).
12) D. W. Pohl, L. Novotny. Near-field optics: Light for the world of NANO. *J. Vac. Sci. Technol.* **B12**, 1441–1446 (1994).
13) J. Koglin, U. C. Fischer, H. Fuchs. Material contrast in scanning near-field optical

microscopy at 1–10 nm resolution. *Phys. Rev. B* **55**, 7977–7984 (1997).

14) N. F. van Hulst, F. B. Segerink, F. Achten, B. Bögler. Evanescent-field optical microscopy: Effects of polarization, tip shape, and radiative waves. *Ultramicroscopy* **42–44**, 416–421 (1992).
15) M. Specht, J. D. Pedarnig, W. M. Heckl, T. W. Hänsch. Scanning plasmon near-field microscope. *Phys. Rev. Lett.* **68**, 476–479 (1992).
16) A. J. Bard, F.-R. F. Fan, J. Kwak, O. Lev. Scanning electrochemical microscopy. Introduction and principles. *Anal. Chem.* **61**, 132–138 (1989).
17) A. J. Bard, P. R. Unwin, D. O. Wipf, F. Zhou. Scanning electrochemical microscopy. *AIP Conf. Proc.* **241**, 235–247 (1992).
18) A. J. Bard, F.-R. F. Fan, D. T. Pierce, P. R. Unwin, D. O. Wipf, F. Zhou. Chemical imaging of surfaces with the scanning electrochemical microscope. *Science* **254**, 68–74 (1991).
19) G. Binnig, C. F. Quate, and Ch. Gerber. Atomic force microscope. *Phys. Rev. Lett.* **56**, 930 (1986).
20) D. Rugar, and H. Paul. Atomic force microscopy. *Phys. Today* **43**, 23-30 (1990).
21) F. J. Giessibl. Advances in atomic force microscopy. *Rev. Mod. Phys.* **75**, 949 (2003).
22) P. Eaton, and P. West. Atomic force microscopy. *Oxford University Press, Oxford* (2010).
23) J. Frommer. Scanning tunneling and atomic force microscopy in organic chemistry. *Angew. Chem.* **104**, 1325–1357 (1992).
24) S. N. Magonov. Surface characterization of materials at ambient conditions by scanning tunneling microscopy (STM) and atomic force microscopy (AFM). *Appl. Spectrosc. Rev.* **28**, 1–121 (1993).
25) H. Fuchs. Atomic force and scanning tunneling microscopy of organic surfaces. *J. Mol. Struct.* **292**, 29–47 (1993).
26) F. J. Giessibl. Atomic force microscopy in ultrahigh vacuum, *Jpn. J. Appl. Phys.* **33**, 3726–3734 (1994).
27) F. J. Giessibl. High-speed force sensor for force microscopy and profilometry

utilizing a quartz tuning fork. *Appl. Phys. Lett.* **73**, 3956–3958 (1998).

28) F. J. Giessibl, A direct method to calculate tip-sample forces from frequency shifts in frequency-modulation atomic force microscopy. *Appl. Phys. Lett.* **78**, 123–125 (2001).

29) F. J. Giessibl, H. Bielefeldt, S. Hembacher, and J. Mannhart, Imaging of atomic orbitals with the atomic force microscope—experiments and simulations. *Ann. Phys.* **10**, 887–910 (2001).

30) S. Hembacher, F. J. Giessibl, and J. Mannhart. Evaluation of a force sensor based on a quartz tuning fork for operation at low temperatures and ultra-high vacuum. *Appl. Surf. Sci.* **188**, 445–449 (2002).

31) M. Herz, F. J. Giessibl, and J. Mannhart. Probing the shape of atoms in real space. *Phys. Rev. B* **68**, 045301 (2003).

32) H. Hölscher, W. Allers, U. D. Schwarz, A. Schwarz, and R. Wiesendanger. Calculation of the frequency shift in dynamic force microscopy. *Appl. Surf. Sci.* **140**, 344–351 (1999).

33) H. Hölscher, A. Schwarz, W. Allers, U. D. Schwarz, and R. Wiesendanger, Quantitative analysis of dynamic-forcespectroscopy data on graphite(0001) in the contact and noncontact regimes. *Phys. Rev. B* **61**, 12 678–12 681 (2000).

34) P. M. Hoffmann, S. Jeffery, J. B. Pethica, H. Özgür Özer, and A. Oral. Energy dissipation in atomic force microscopy and atomic loss processes. *Phys. Rev. Lett.* **87**, 265502 (2001).

35) P. M. Hoffmann, A. Oral, R. A. Grimble, H. Özgür Özer, S. Jeffrey, and J. B. Pethica. Direct measurement of interatomic force gradients using an ultra-low-amplitude atomic force microscope. *Proc. Math. Phys. Eng. Sci.* **457**, 1161–1174 (2001).

36) M. Gauthier, R. Perez, T. Arai, M. Tomitori, and M. Tsukada. Interplay between nonlinearity, scan speed, damping, and electronics in frequency modulation atomic force microscopy. *Phys. Rev. Lett.* **89**, 146104 (2002).

37) G. Friedbacher, T. Prohaska, and M. Grasserbauer. Surface analysis with atomic force microscopy through measurement in air and under liquids. *Mikrochim. Acta*

113, 179–202 (1994).

38) J. Hu, X. D. Xiao, D. F. Ogletree, and M. Salmerón. Imaging the condensation and evaporation of molecularly thin films of water with nanometer resolution. *Science* **268**, 267 (1995).

39) J. Hu, X. D. Xiao, and M. Salmerón. Scanning polarization force microscopy: A technique for imaging liquids and weakly adsorbed layers. *Appl. Phys. Lett*. **67,** 476-478 (1995).

40) G. Gramse, M. A. Edwards, L. Fumagalli, and G. Gomila, Theory of amplitude modulated electrostatic force microscopy for dielectric measurements in liquids at MHz frequencies. *Nanotechnology* **24**, 415709 (2013).

41) M. S. Anderson. Locally enhanced Raman spectroscopy with an atomic force microscope. *Appl. Phys. Lett.* **76**, 3130-3132 (2000).

42) R. M. Stöckle, Y. D. Suh, V. Deckert, and R. Zenobi. Nanoscale chemical analysis by tip-enhanced Raman spectroscopy. *Chem. Phys. Lett.* **318**, 131-136 (2000).

43) N. Hayazawa, Y. Inouye, Z. Sekkat, and S. Kawata. Near-field Raman scattering enhanced by a metallized tip. *Chem. Phys. Lett.* **335**, 369-374 (2001).

44) U. Kaiser, A. Schwarz, and R. Wiesendanger. Magnetic exchange force microscopy with atomic resolution. *Nature* **446**, 522 (2007).

45) C. Lazo, V. Caciuc, H. Hölscher, and S. Heinze. Role of tip size, orientation, and structural relaxations in first-principles studies of magnetic exchange force microscopy and spin-polarized scanning tunneling microscopy. *Phys. Rev. B* **78**, 214416 (2008).

46) F. Pielmeier, and F.J. Giessibl. Spin resolution and evidence for superexchange on NiO (001) observed by force microscopy. *Phys. Rev. Lett.* **110**, 266101 (2013).

47) B. D. Terris, J. E. Stern, D. Rugar, and H. J. Mamin. Contact electrification using force microscopy. *Phys. Rev. Lett.* **63**, 2669 (1989).

48) D. W. Abraham, C. Williams, J. Slinkman, and H. K. Wichramasinghe. Lateral dopant profiling in semiconductors by force microscopy using capacitive detection. *J. Vac. Sci. Technol. B* **9**, 703 (1991).

49) D. W. Abraham, and H. K. Wichramasinghe. High resolution atomic force

microscopy potentiometry. *J. Vac. Sci. Technol. B* **9**, 1559 (1991).

50) S. Kitamura and M. Iwatsuki. High-resolution imaging of contact potential difference with ultrahigh vacuum noncontact atomic force microscope. *Appl. Phys. Lett.* **72**, 3154 (1998).

51) P. Girard. Electrostatic force microscopy: principles and some applications to semiconductors. *Nanotechnology* **12**, 485 (2001).

52) G. Gramse, I. Casuso, J. Toset, L. Fumagalli, and G. Gomila, Quantitative dielectric constant measurement of thin films by DC electrostatic force microscopy. *Nanotechnology* **20**, 395702 (2009).

53) A. Olbrich, B. Ebersberger, and C. Boit. Conducting atomic force microscopy for nanoscale electrical characterization of thin SiO2. *Appl. Phys. Lett.* **73**, 3114 (1998).

54) D. J. Wold, and C. D. Frisbie. Fabrication and characterization of metal−molecule−metal junctions by conducting probe atomic force microscopy. *J. Am. Chem. Soc.* **123**, 5549-5556 (2001).

55) J. J. Kopanski, J. F. Marchiando, and J. R. Lowney. Scanning capacitance microscopy measurements and modeling: Progress towards dopant profiling of silicon. *J. Vac. Sci. Technol. B* **14**, 242 (1996).

56) Y. Naitou, H. Arimura, N. Kitano, S. Horie, T. Minami, M. Kosuda, H. Ogiso, T. Hosoi, T. Shimura, and H. Watanabe. Charge trapping properties in TiO2/HfSiO/SiO2 gate stacks probed by scanning capacitance microscopy. *Appl. Phys. Lett.* **92**, 012112 (2008).

57) U. Zerweck, C. Loppacher, T. Otto, S. Grafström, and L. M. Eng. Accuracy and resolution limits of Kelvin probe force microscopy. *Phys. Rev. B*, **71**, 125424 (2005).

58) W. Melitz, J. Shen, A. C. Kummel, and S. Lee. Kelvin probe force microscopy and its application. *Surf. Sci. Rep.* **66**, 1-27. (2011).

59) P. Eyben, M. Xu, N. Duhayon, T. Clarysse, S. Callewaert and W. Vandervorst. Scanning spreading resistance microscopy and spectroscopy for routine and quantitative two-dimensional carrier profiling. *J. Vac. Sci. Technol. B* **20**, 471-478 (2002).

60) L. Zhang, K. Ohuchi, K. Adachi, K. Ishimaru, M. Takayanagi, and A. Nishiyama. High-resolution characterization of ultrashallow junctions by measuring in vacuum with scanning spreading resistance microscopy. *Appl. Phys. Lett.* **90**, 192103 (2007).

61) K. Lai, W. Kundhikanjana, H. Peng, Y. Cui, M. A. Kelly, and Z. X. Shen. Tapping mode microwave impedance microscopy. *Rev. Sci. Instrum.* **80**, 043707 (2009).

62) Y. T. Cui, E. Y. Ma, and Z. X. Shen. Quartz tuning fork based microwave impedance microscopy. *Rev. Sci. Instrum.* **87**, 063711 (2016).

63) X. Wu, Z. Hao, D. Wu, L. Zheng, Z. Jiang, V. Ganesan, Y. Wang, K. Lai. Quantitative measurements of nanoscale permittivity and conductivity using tuning-fork-based microwave impedance microscopy. *Rev. Sci. Instrum.* **89**, 043704 (2018).

64) A. Karbassi, D. Ruf, A. D. Bettermann, C. A. Paulson, D. W. van der Weide, H. Tanbakuchi, and R. Stancliff. Quantitative scanning near-field microwave microscopy for thin film dielectric constant measurement. *Rev. Sci. Instrum.* **79**, 094706 (2008).

65) A. Imtiaz, T. M. Wallis, and P. Kabos. Near-field scanning microwave microscopy: An emerging research tool for nanoscale metrology. *IEEE Microw. Mag.* **15**, 52-64 (2014).

66) G. Gramse, M. Kasper, L. Fumagalli, G. Gomila, P. Hinterdorfer, and F. Kienberger. Calibrated complex impedance and permittivity measurements with scanning microwave microscopy. *Nanotechnology* **25**, 145703 (2014).

67) G. Gramse, E. Brinciotti, A. Lucibello, S. B. Patil, M. Kasper, C. Rankl, R. Giridharagopal, P. Hinterdorfer, R. Marcelli and F. Kienberger. Quantitative sub-surface and non-contact imaging using scanning microwave microscopy. *Nanotechnology* **26**, 135701 (2015).

68) S. S. Tuca, G. Badino, G. Gramse, E. Brinciotti, M. Kasper, Y. J. Oh, R. Zhu, C. Rankl, P. Hinterdorfer and F. Kienberger. Calibrated complex impedance of CHO cells and E. coli bacteria at GHz frequencies using scanning microwave microscopy. *Nanotechnology* **27**, 135702 (2016).

69) F. J. Giessibl, and G. Binnig. True atomic resolution on KBr with a low-temperature

atomic force microscope in ultrahigh vacuum. *Ultramicroscopy* **42-44**, 281–286 (1992).

70) F. Ohnesorge, and G. Binning. True atomic resolution by atomic force microscopy through repulsive and attractive forces. *Science* **260**, 1451–1456 (1993).

71) T. Miyamoto, R. Kaneko, and S. Miyake. Tribological characteristics of amorphous carbon films investigated by point contact microscopy. *J. Vac. Sci. Technol.* **B9**, 1336–1339 (1991).

72) P. Maivald, H.-J. Butt, S. A. C. Gould, C. B. Prater, B. Drake, J. A. Gurley, V. B. Elings, and P. K. Hansma. Using force modulation to image surface elasticities with the atomic force microscope. *Nanotechnology* **2**, 103–106 (1991).

73) R. M. Overney, T. Bonner, E. Meyer, M. Rüetschi, R. Lüthi, L. Howald, J. Frommer, H.-J. Güntherodt, M. Fujihira, and H. Takano. Elasticity, wear, and friction properties of thin organic films observed with atomic force microscopy. *J. Vac. Sci. Technol.* **B12**, 1973–1976 (1994).

74) Q. Zhong, D. Inniss, K. Kjoller, and V. B. Elings. Fractured polymer/silica fiber surface studied by tapping mode atomic force microscope. *Surf. Sci. Lett.* **290**, L688–L692 (1993).

75) K. Umemura, H. Arakawa, and A. Ikai. High resolution imaging of cell surface using a tapping–mode atomic force microscopy. *Jpn. J. Appl. Phys.* **11B**, L1711–L1714 (1993).

76) P. K. Hansma, J. P. Cleveland, M. Radmacher, D. A. Walters, P. E. Hillner, M. Bezanilla, M. Fritz, D. Vie, H. G. Hansma, C. B. Prater, J. Massie, L. Fukunaga, J. Gurley, and V. Elings. Tapping mode atomic force microscopy in liquids. *Appl. Phys. Lett.* **64**, 1738–1740 (1994).

77) C. A. J. Putman, K. O. van der Werf, B. G. De Grooth, N. F. Van Hulst, and J. Greve. Tapping mode atomic force microscopy in liquid. *Appl. Phys. Lett.* **64**, 2454–2456 (1994).

78) T. Shibata-Seki, W. Watanabe, and J. Masai. Imaging of cells with atomic force microscopy at a tapping mode. *J. Vac. Sci. Technol.* **B12**, 1530–1534 (1994).

79) C. A. J. Putman, K. O. van der Werf, B. G. de Grooth, N. F. van Hulst, and J. Greve.

Viscoelasticity of living cells allows high resolution imaging by tapping mode atomic force microscopy. *Biophys. J.* **67**, 1749–1753 (1994).

80) S. H. Leuba, G. Yang, C. Robert, B. Samori, K. van, Holde, J. Zlatanova, and C. Bustamente. Three-dimensional structure of extended chromatin fibers as revealed by tapping-mode scanning force microscopy. *Proc. Natl. Acad. Sci.* **91**, 11621–11625 (1994).
81) F. J. Giessibl. Atomic resolution of the silicon (111)-(737) surface by atomic force microscopy. *Science* **267**, 68–71 (1995).
82) S. Morita, R. Wiesendanger, and E. Meyer. Noncontact atomic force microscopy. *Springer, Berlin* (2002).
83) S. Morita, F. J. Giessibl, and R. Wiesendanger. Noncontact atomic force microscopy Vol. 2. *Springer, Berlin* (2009).
84) S. Morita, F. J. Giessibl, E. Meyer, and R. Wiesendanger. Noncontact atomic force microscopy Vol. 3. *Springer, Berlin* (2015).
85) B. J. Albers, T. C. Schwendemann, M. Z. Baykara, N. Pilet, M. Liebmann, E. I. Altman, and U. D. Schwarz. Three-dimensional imaging of short-range chemical forces with picometre resolution. *Nat. Nanotechnol.* **4**, 307-310 (2009).
86) M. Z. Baykara, O. E. Dagdeviren, T. C. Schwendemann, H. Mönig, E. I. Altman, and U. D. Schwarz. Probing three-dimensional surface force fields with atomic resolution: Measurement strategies, limitations, and artifact reduction. Beilstein J. Nanotechnol. **3**, 637-650 (2012).
87) C. Moreno, O. Stetsovych, T. K. Shimizu, and O. Custance. Imaging three-dimensional surface objects with submolecular resolution by atomic force microscopy. *Nano Lett.* **15**, 2257-2262 (2015).
88) T. Fukuma, K. Kobayashi, K. Matsushige, and H. Yamada. True atomic resolution in liquid by frequency-modulation atomic force microscopy. *Appl. Phys. Lett.* **86**, 193108 (2005).
89) N. Kobayashi, H. Asakawa, and T. Fukuma. Nanoscale potential measurements in liquid by frequency modulation atomic force microscopy. *Rev. Sci. Instrum.* **81**, 123705 (2010).

90) Y. Ju, K. Inoue, M. Saka, and H. Abé. Contactless measurement of electrical conductivity of semiconductor wafers using the reflection of millimeter waves. *Appl. Phys. Lett.* **81**, 3585-3587 (2002).
91) Y. Ju, Y. Hirosawa, H. Soyama, and M. Saka. Contactless measurement of electrical conductivity of Si wafers independent of wafer thickness. *Appl. Phys. Lett.* **87**, 162102 (2005).
92) L. Liu, and Y. Ju. Nondestructive measurement and high-precision evaluation of the electrical conductivity of doped GaAs wafers using microwaves. *Rev. Sci. Instrum.* **81**, 124701 (2010).
93) Y. Ju, T. Kobayashi, and H. Soyama. Development of a nanostructural microwave probe based on GaAs. *Microsyst. Technol.* **14**, 1021-1025 (2008).
94) Y. Ju, M. Hamada, T. Kobayashi, and H. Soyama. A microwave probe nanostructure for atomic force microscopy. *Microsyst. Technol.* **15**, 1195-1199 (2009).
95) L. Zhang, Y. Ju, A. Hosoi, and A. Fujimoto. Microwave atomic force microscopy imaging for nanometer-scale electrical property characterization. *Rev. Sci. Instrum.* **81**, 123708 (2010).
96) L. Zhang, Y. Ju, A. Hosoi, and A. Fujimoto. Microwave atomic force microscopy: quantitative measurement and characterization of electrical properties on the nanometer scale. *Appl. Phys. Express* **5**, 016602 (2011).
97) L. Zhang, Y. Ju, A. Hosoi, and A. Fujimoto. Measurement of electrical properties of materials under the oxide layer by microwave-AFM probe. *Microsyst. Technol.* **18**, 1917-1922 (2012).
98) L. Zhang, A. Hosoi, and Y. Ju, A Study on Spatial Resolution of the Microwave Atomic Force Microscope Imaging Affected by Scanning Speed. *Mater. Sci. Forum* **750**, 200-203 (2013).
99) L. Zhang, Y. Song, A. Hosoi, Y. Morita, and Y. Ju. Microwave atomic force microscope: MG63 osteoblast-like cells analysis on nanometer scale. *Microsyst. Technol.* **22**, 603-608 (2016).

Chapter 2 Probe Fabrication and Experiment Approach

2.1 Fabrication of Slit Probe and Coaxial Probe

Two kinds of probe were designed for M-AFM so that it can be adapted to different needs, one is slit structured probe and the other is coaxial structured probe. The schematics of the two probes are shown in Fig. 2-1 (a) and (b), respectively. The slit probe was designed to combine the structures of both the AFM probe and parallel-plate transmission line [1,2,3]. The scanning electron microscopy (SEM) image of the slit probe in different fabrication steps are shown in Fig. 2-2 (a)-(d). To reduce the attenuation of microwave propagation inside the probe, a non-doped GaAs wafer, which is a semi-insulator material, was used as the structural material of the probe. By photolithography and wet etching, the probes were fabricated from a piece of non-doped GaAs wafer. The probe holder with a 17-μm-thick cantilever and a 6-μm-long sharp tip were fabricated using photolithography and wet-etching processes (see Fig. 2-2 (a) and (b)). To fabricate the waveguide which can confine the microwave inside the probe, both surfaces of the tip side and reverse side of the probe were coated with 50 nm Au films by electron beam evaporation. These films served as the two electrodes of a parallel-plate transmission line (see Fig. 2-2 (c)). To allow microwave emission at the tip, the two films were connected to each other at the end of the cantilever, and a 50-nm-wide slit was fabricated using a focused ion beam (FIB) etching across the tip of the probe (see Fig. 2-2 (d)). We should note that, although perfect symmetry of the tip is difficult to achieve at the nanoscale level, the theoretical model introduced in the next chapter indicates that the asymmetry of the tip would not affect the measurement accuracy if only the two sides of the split tip have the same length.

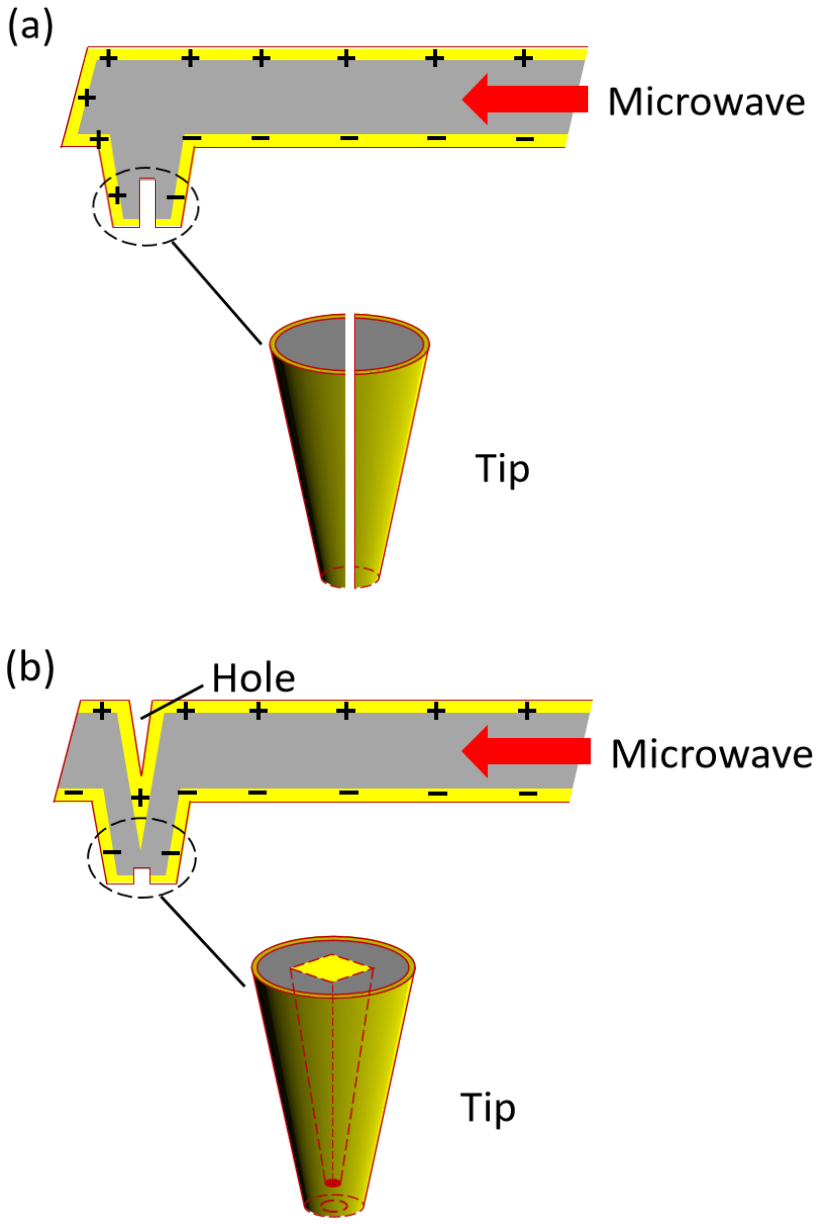

Figure 2-1: The schematics of slit probe (a) and coaxial probe (b).

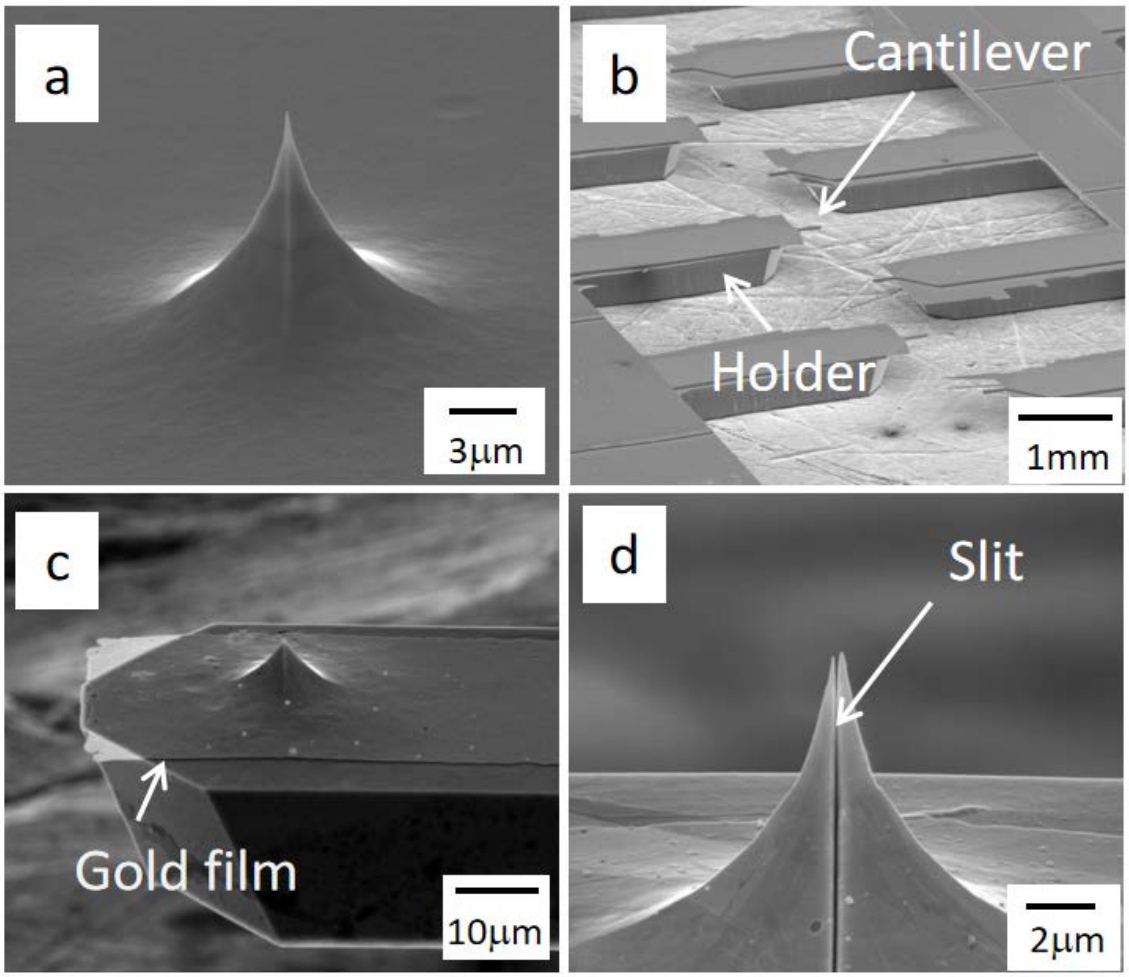

Figure 2-2: The SEM image of the slit probe: (a) fabrication of the tip; (b) fabrication of the holder and cantilever; (c) coating of the Au film; (d) fabrication of the slit.

On the other hand, for the coaxial probe, the holder and the cantilever were similar to those of the silt probe, but the tip was designed based on the coaxial transmission line as shown in Fig. 2-1 (b) [4]. Unlike the slit probe which may leak the microwave from the whole slit across the cantilever, the coaxial probe has a more closed structure which can confine the microwave inside the gold film of the tip until it is emitted at the end of the tip. Also, the coaxial probe works at transverse electromagnetic (TEM) mode, and the cutoff frequency does not exist, which means the coaxial probe can deliver more microwave power to the aperture of the tip in a small dimension. Therefore, the coaxial

probe has a stronger emission power and consequently resulting in an increase in the measurement sensitivity.

To emphasize the difference between slit probe and coaxial probe, the SEM images of the tip of the coaxial probe are shown in Fig. 2-3. After the tip, cantilever and holder of the probe were fabricated in the same way of the slit probe, a pyramid hole with a depth of 22.5 μm was dug on the reverse surface by FIB etching at the position of the tip (See Fig. 2-3 (a)). The alignment was performed based on the position from the edge of the cantilever. Then 50 nm Au films were coated on both sides of the probe surface by electron beam evaporation, which is also the same as the fabrication of slit probes. The Au films on the tip and in the pyramid-hole serve as the outer conductor and inner conductor of the coaxial structure, respectively, as shown by Fig. 2-1 (b). Finally, using FIB etching a 50 nm hole was fabricated at the end of the tip through the Au film, which serves as the aperture to emit microwave (See Fig. 2-3 (b)). Since a feature of the sample with a dimension smaller than the aperture cannot be truthfully detected, the aperture was fabricated as small as possible to improve the resolution.

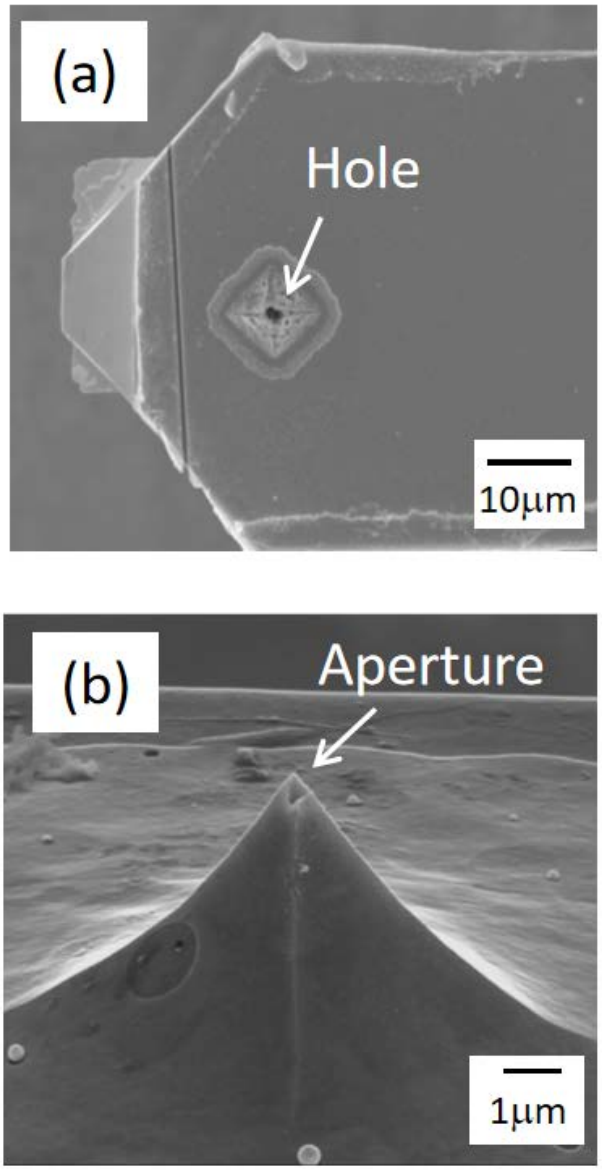

Figure 2-3: The SEM images of coaxial probe: (a) the pyramid hole on the back side of the cantilever; (b) the small aperture on the tip.

2.2 Evaluation of Slit Probe and Coaxial Probe

To compare the sensitivity and resolution of the coaxial probe and the slit probe, the reflection experiment was conducted on a GaAs substrate with Au strips using a 94-GHz microwave for the two probes. The schematic of the experiment is shown in Fig. 2-4, which is the same as the setup introduced in Chapter 1 [3]. The width of GaAs and Au regions are 3.5 μm and 8.5 μm, respectively. The scanning results of 10×10 μm^2 microwave image by the two probes are shown in Fig. 2-5. It can be obviously observed that the image of coaxial probe has a higher contrast than that of the slit probe. $|(V_{\mathrm{GaAs}} - V_{\mathrm{Au}})/(V_{\max} - V_{\min})|$, which represents the relative output voltage variation from GaAs region to Au region, is 0.37 for coaxial probe and 0.25 for slit probe. This indicates that the sensitivity of coaxial probe is 1.48 times higher than that of the slit probe. On the other hand, the spatial resolution can be evaluated from the cross section curve corresponding to the red arrow of the scanning image. The horizontal length of the slope region which depicts the edge of the Au strip represents the resolution. It can be observed that the resolution of the coaxial probe was evaluated as 720 nm, which is lower than that of the slit probe being 440 nm. It is because that the aperture of slit probe which has a simpler structure can be fabricated smaller than the coaxial probe.

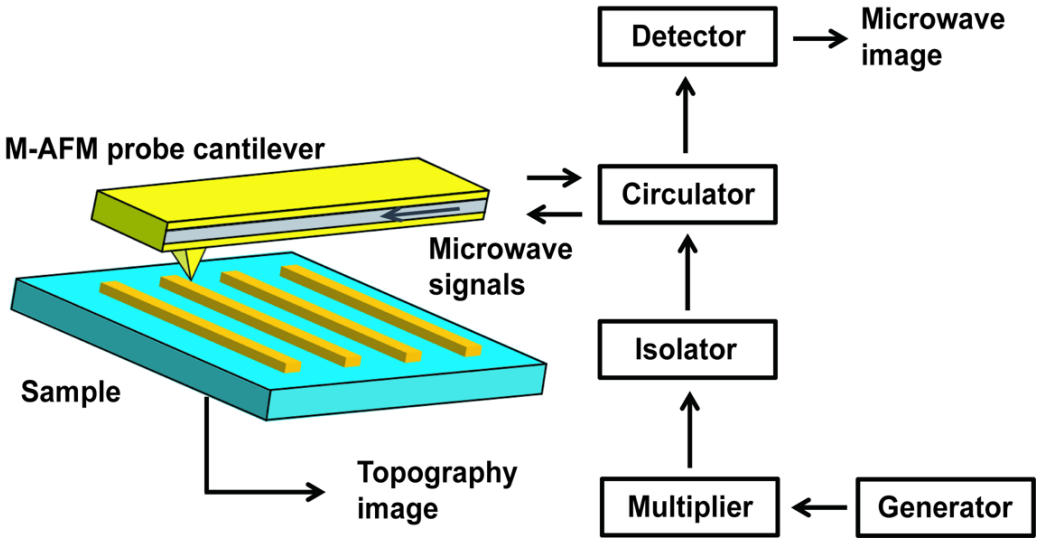

Figure 2-4: The schematic of the cross section of slit probe.

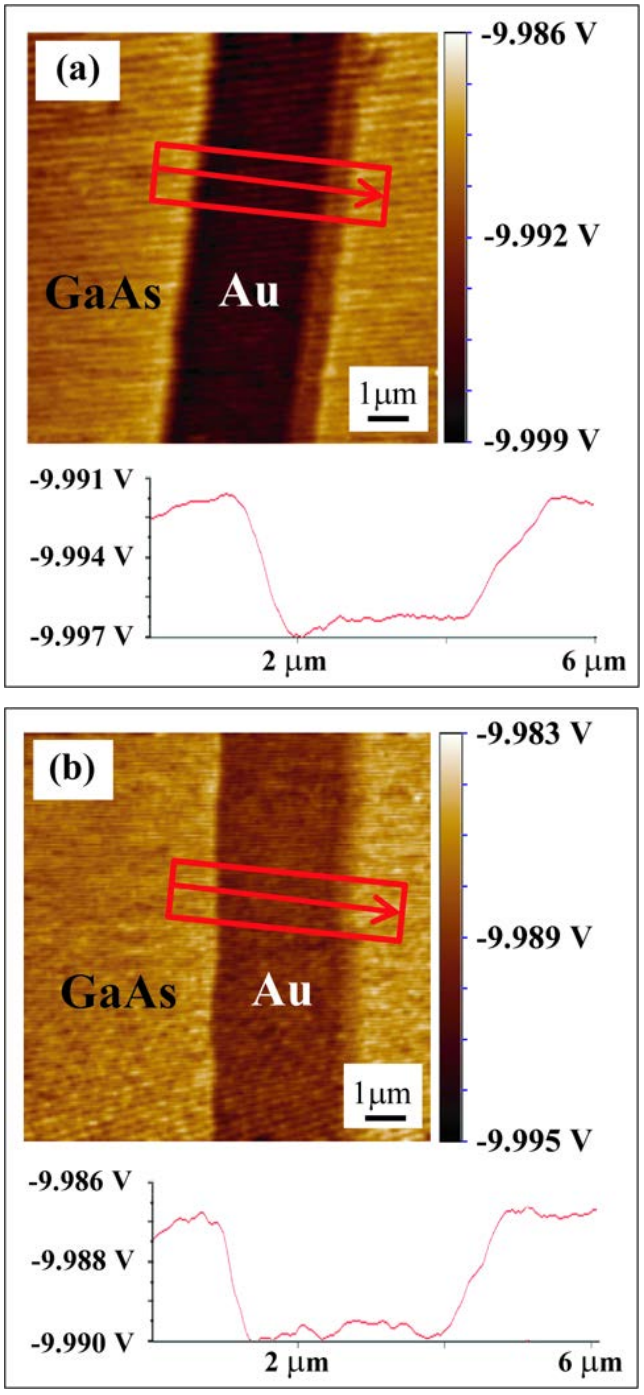

Figure 2-5: The scanning microwave images of Au strip on GaAs substrate by coaxial probe (a) and slit probe (b) [4].

2.3 Measurement Approach for Dielectric Materials and Metallic Materials

In previous development of M-AFM, the measurement was based on the non-contact scanning mode as introduced in Chapter 1 [3]. Besides the contact, tapping and non-contact scanning modes which scan the topography of sample surface, AFM also has another measurement mode named force curve mode [5]. The experimental setup of this mode is the same as the scanning modes above. The difference is that it measures the distance dependence of interaction force between the tip and sample at a certain point. In this mode, the probe of AFM moves along the vertical direction of the sample surface instead of the horizontal direction as shown by Fig. 2-6. The force curve measurement also has contact mode and non-contact mode. Similar to topography scanning, the cantilever does not vibrate in contact force curve mode. The deformation of the cantilever is recorded by the AFM, which is used to calculate the force between the tip and sample. On the other hand, in non-contact force curve mode before measurement, the natural frequency of cantilever is obtained by tuning. Then the probe is lowered to approach the sample while vibrated at its nature frequency. When the amplitude of vibration is detected to decrease, it means the resonance frequency has changed because external force has appeared. Then the approaching is stopped and the measurement begins. In measurement, the probe moves from up to down based on the setup positions relative to the approach point and the variation of resonance frequency as a function of tip-sample distance is recorded for the evaluation of force. Here, since it is non-contact mode, the measured distance is relative value at first. The absolute value is determined by fitting the force curve. In this way, the curve of the tip-sample atomic force depending on the tip-sample distance is obtained as the output of this mode. In this thesis, we use the non-contact mode to realize the non-contact quantitative evaluation.

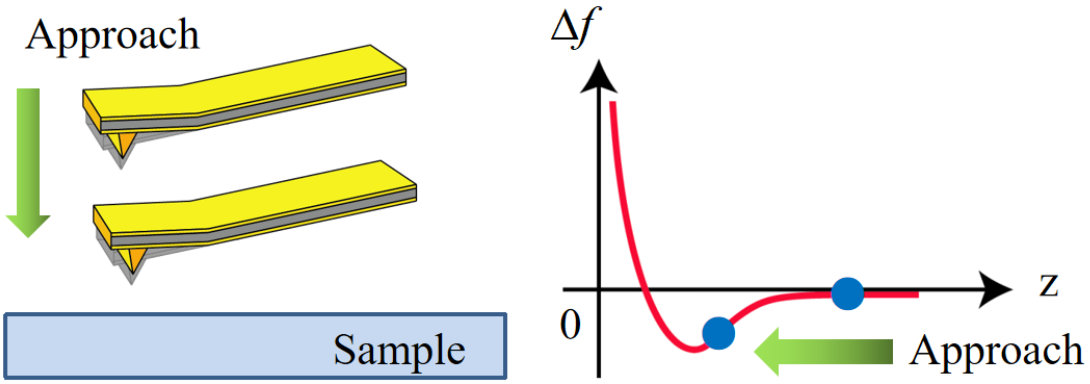

Figure 2-6: The schematic of force curve mode.

The force curve measurement in non-contact mode is very meaningful for the quantitative evaluation of M-AFM since it can provide the necessary distance information for the evaluation of near field microwave distribution. Because the microwave generates a new electromagnetic interaction between the tip and sample, the tip-sample distance, which is the standoff distance in scanning mode, may be affected by this force. For different materials, the difference in local electrical property may also cause the difference of the tip-sample electric force and thus alter the standoff distance. Theoretically, the electric field of reflected microwave, which determines the electric force, depends on the polarization of the sample. In the case of dielectric materials, the bounded charges are polarized in different extent according to the permittivity. However, in the case of metallic materials, there exists sufficient free charges and they can reach the same electrostatic equilibrium state, that is, no electric field inside metallic materials. It means that polarization charge of different metals has almost no relation with the conductivity of the material. Therefore, the reflected microwave of dielectric materials depends on the electrical property of the sample much more strongly than metallic materials do. It means that when we need to calibrate the reflected signal, it can not be ensure that the standoff distance is always a consistent for different dielectric materials. This brings a problem in measurement accuracy because in near-field range the wave

intensity decrease with distance. The incident wave arrived at the sample surface, which is exactly what we need to calibrate, strongly depends on the standoff distance. The prerequisite of calibration is that the incident wave arriving at the sample surface every time is constant. Therefore, accurate calibration is almost impossible for dielectric materials and this brings error. Using force curve measurement, in which method the distance dependence of near-field microwave is under quantitative consideration through curve fitting, it will provide a higher measurement accuracy than measuring the reflected signal in scanning mode. In conclusion the force curve mode is more appropriate for the permittivity evaluation of dielectric materials. It should be pointed out that although a direct current signal can also realize a similar force measurement, microwave signal or even higher frequency can deliver a stronger electric field to the aperture of the probe. In M-AFM, the two electrodes of microwave circuit are not on two sides of the probe-sample system but both are on the probe. The microwave signal is delivered to the probe by wave guide and emitted by the probe itself independently. Therefore, there exist a cutoff frequency in this microwave system and signal under this frequency can hardly be transmitted. Also, the microwave method has the potential to provide the sample property in a wide range of frequency.

However, although the force curve measurement can provide the information of distance dependence, it cannot be applied to the conductivity evaluation of metallic materials. As explained in the above section, unlike dielectric materials which have a wide range of reflection coefficients, the reflection coefficients of different metallic materials are all very close to 1. It means that in experiment the tip-sample interaction force caused by microwave is even less sensitive to the difference of materials than the reflected microwave itself. Therefore, we have to measure the slight difference of reflected wave through the electrical signal of lock-in amplifier to improve the sensitivity. As a result, the non-contact scanning mode is optimal for conductivity evaluation of metals. For the same reason, we use coaxial probes for evaluation of metals to improve the measurement sensitivity, while slit probes which are easier to be fabricated with higher resolutions are used for the evaluation of dielectric materials.

References

1) Y. Ju, T. Kobayashi, and H. Soyama. Development of a nanostructural microwave probe based on GaAs. *Microsyst. Technol.* **14**, 1021-1025 (2008).
2) Y. Ju, M. Hamada, T. Kobayashi, and H. Soyama. A microwave probe nanostructure for atomic force microscopy. *Microsyst. Technol*. **15**, 1195-1199 (2009).
3) L. Zhang. A study on the development microwave atomic force microscopy, Master thesis (Nagoya University, Nagoya, Japan, 2012)
4) T. Hirabayashi. Development of coaxial structured probe of microwave atomic force microscopy, Master thesis (Nagoya University, Nagoya, Japan, 2018)
5) F. J. Giessibl. Advances in atomic force microscopy. Rev. Mod. Phys. **75(**3), 949 (2003).

Chapter 3 Local Permittivity Measurement of Dielectric Materials Based on Non-contact Force Curve of M-AFM

3.1 Introduction

In this chapter, we develop a non-contact and quantitative method for the local permittivity measurement of dielectric materials to expand the function of M-AFM. A theoretical model based on near-field approximation was developed to describe the effect of a microwave on the interaction between a probe and a sample. Since the information about distance dependence is important for dielectric materials, the measurement is based on the non-contact force curve mode. We successfully measured the force curves of Si, Al_2O_3, Ge, and ZrO_2 using a slit structured M-AFM probe and observed the variation in the force caused by the microwave. According to the established theoretical model, a quantitative non-contact evaluation of the local permittivity of dielectric materials was performed.

3.2 Experimental Approach

3.2.1 Examination of M-AFM Probe

To confirm that the slit probe used in this study can emit microwave, the reflection experiment was conducted using a 94-GHz microwave. In this experiment, a Si substrate with Au strips was fabricated by photolithography and electron-beam (EB)

evaporation. It was scanned by M-AFM in non-contact scanning mode. The strips of the sample were a regular cuboid array with a height of 1.2 μm, width of 2 μm, and interspace gap of 8 μm. Fig. 3-1 shows the scanning results of the topography (a) and microwave image (b) of the test sample. It is found that the microwave image corresponds well with the topography image, and the voltage difference between the Si substrate and Au stripe was approximately 2.1 mV. The result indicates that a microwave can be successfully emitted to the sample surface and then received by the probe.

3.2.2 Force Curve Measurement

In the permittivity measurement, commercial slab samples of Si, Ge, and ZrO_2 with a thickness of 1 mm were prepared. An Al_2O_3 film sample was fabricated on a glass substrate with a thickness of more than 500 nm using EB evaporation. All of these samples were regarded as bulk materials in the experiment. For each sample, the resonant-frequency variation in the probe versus the distance between the probe and sample was measured under the non-contact force curve mode. The movement range of the probe was from -2 nm to 15 nm. Here, the distance was not the absolute tip-sample distance, but the distance from the position that the tip stopped after approaching process. The absolute tip-sample distance was obtained by fitting the force curves. Every single frequency-variation curve was measured under three conditions: no microwave and with 5-dBm and 10-dBm microwaves. The power of microwave referring to the source power. The measurement was conducted in air, and the environmental temperature and relative humidity were 20.0 °C and 50%, respectively. To ensure that the electric-field intensity at the tip of the probe is the same in all measurements, the results are measured using the same probe.

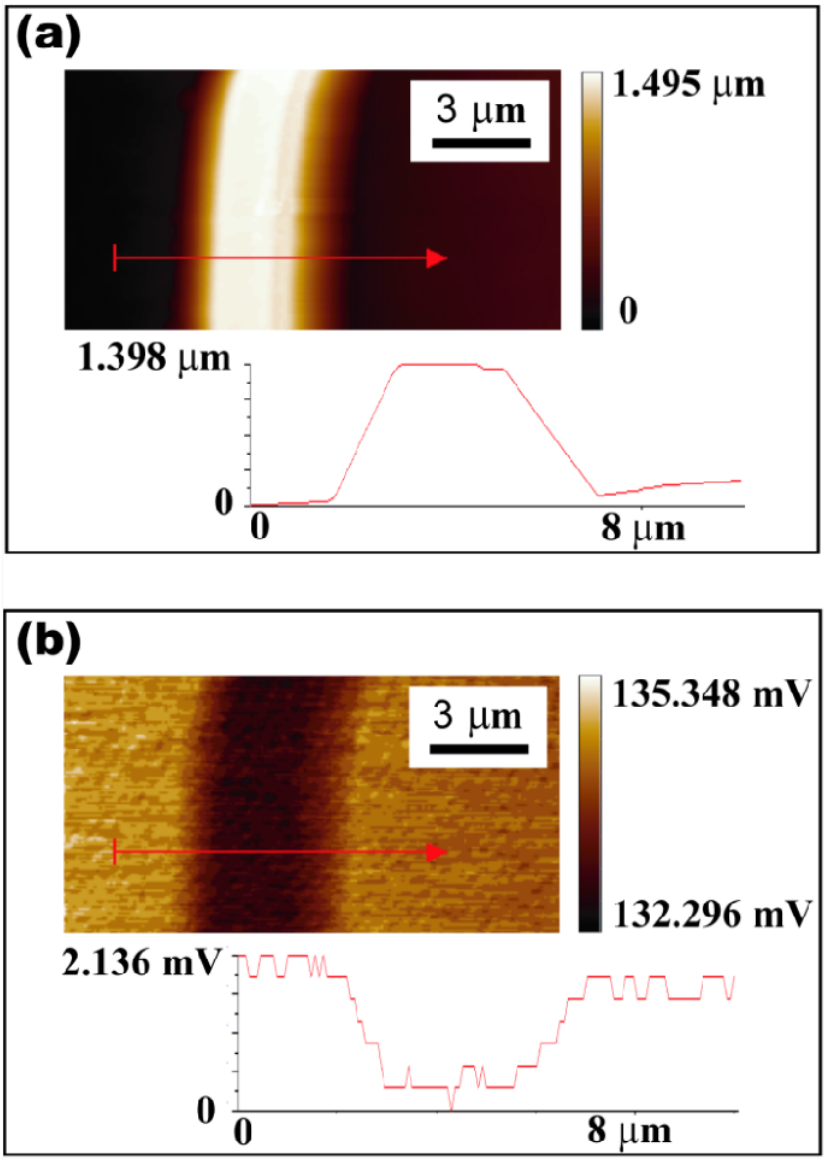

Figure 3-1: The scanning results of (a) topography and (b) microwave images of the Au striped test sample.

3.3 Establishment of Theoretical Model under Near-field Condition

3.3.1 Near-field Incident Wave and Reflected Wave

According to Maxwell equation, there are two origins of electric field: one is charge and the other is alternating magnetic field. The former one and the latter one correspond to the divergence and curl of electric field, respectively. For electromagnetic wave propagated to a place far away from its field source, including plane wave and spherical wave, the electric field is generated by magnetic field. It is also called radiation field. However, for the field close to the source such as an antenna, the electric field is generated by the charge on it. This field is the near field. The near field alternates with the charge and thus generates alternating magnetic field. Then the alternating magnetic field in addition generates alternating electric field and propagates to the far field to become the radiation field. The essential difference of near field and radiation field is that, near field is generated directly by the charge on the source and described by the divergence equation in Maxwell equations, while radiation field is generated by the alternation magnetic field and described by the curl equation in Maxwell equations. This results in an important difference that near field decays with the inverse square of the distance but radiation field can propagate to far field.

The schematic of the near field microwave distribution is as shown in Fig. 3-2. When a microwave is delivered to the slit of the M-AFM probe, which is similar to a parallel-plate waveguide, alternating charges exist on the surface of the gold film. Since the tip-sample distance is within several nanometer, while the wave length of microwave is about 3 mm, the electric field of microwave emitted to the surface of sample should be calculated by charges on the tip to describe the near field distance dependence. In addition, since the tip-sample distance is only 10^{-6} times of the wave length, the phase difference within this region is no more than $2\pi/10^{6}$, which can be

neglected. It means within this extremely short distance, the electric field can be regarded as “action at a distance”. Once the value of charge varies, its electric field varies with it instantly. Therefore, in near-field approximation the electric field of microwave emitted from the aperture can be regarded as a quasi-static field generated by the charges on the tip at every instant [1]. Because the tip of the probe is sharp enough, only the charge at the end of the tip is dominant. As a result, the emitted microwave can be calculated as the electric field of a pair of sinusoidally alternating point charges located at the end of the two tips with opposite electricity. The frequency of charges is the frequency of the microwave. Since all the field and charge discussed in this near-field area have the same phase at the same instant, we are only interested in the amplitude. In the rest part of this thesis, all the fields and charges discussed are their amplitudes. In this case, if the electric field amplitude at the middle of the dipole is designated as E_0, the amplitude of the equivalent charges can be determined as follows:

$$q_0 = \frac{\pi}{2} w^2 \varepsilon_0 E_0 , \tag{3-1}$$

where w is the width of the slit and ε_0 is the permittivity of free space.

The case is similar for the reflected wave. When a microwave is transmitted across a dielectric sample, the atoms in the sample are polarized and the bounded electrons are forced to vibrate under the alternating electric field of microwave. These vibrating electrons and their nucleus form alternating polarization charges as shown in Fig. 3-3(a), and thus generate electric field, which is the near field of reflected wave. The electric field thus generates alternating magnetic field and propagates to far field as radiation field. Again because of the nanometer scale tip-sample distance, the reflected wave received by the tip of probe can be regarded as a quasi-static field generated by the polarization charges at every instant. Usually, a flat sample with relative permittivity ε_r can be considered infinite and isotropic compared with the size of the probe. The thickness of the samples are far larger than the tip-sample distance, which can be regarded as infinite as well. If a single point charge is located above the surface at distance z_0, according to

the conclusion of classic electromagnetism, the electric field of the polarized charge above the interface can be calculated using image charge q_1 below the interface at distance $-z_0$ [1], i.e.,

$$q_1 = -\frac{\varepsilon_r - 1}{\varepsilon_r + 1} q_0 . \tag{3-2}$$

The image charge of the polarization charge are as shown in Fig. 3-3 (b).

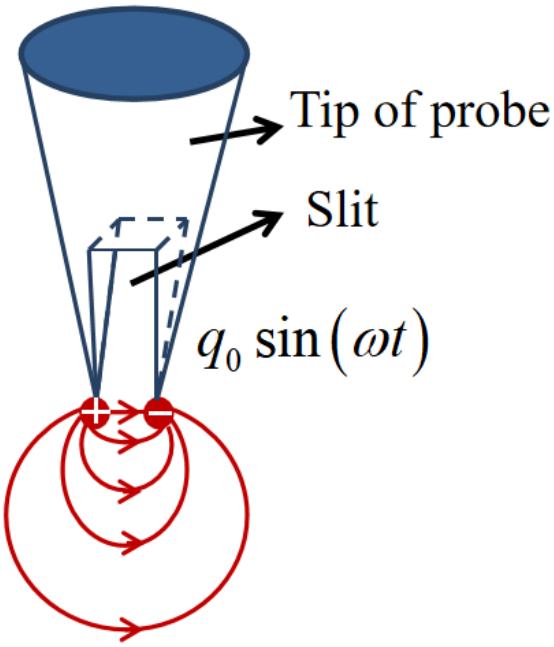

Figure 3-2: The schematic of the near-field distribution of the microwave emitted by a slit probe.

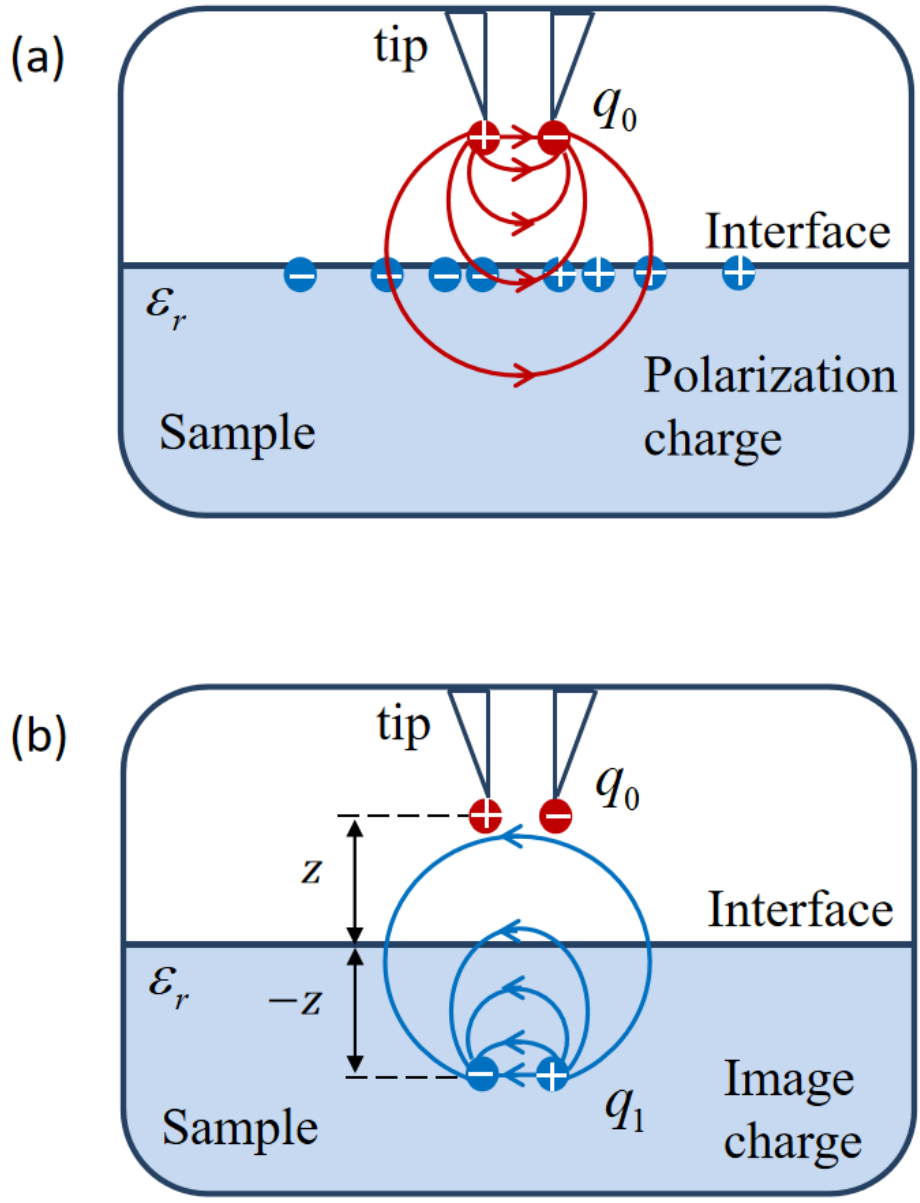

Figure 3-3: The schematic of the near-field distribution of reflected wave: (a) the polarization charge on the surface of the sample; (b) the image charge of polarization charge and near-field distribution of reflected wave.

3.3.2 Coulomb Interaction between Probe and Sample

It can be predicted that the charges at the tip of the probe and in the sample may create another Coulomb force, in addition to the atomic force between the probe and sample. Using the image charge model in the above section to describe the near-field distribution, the additional electromagnetic interaction between the probe and sample caused by the microwave can be calculated using Coulomb law as

$$F_{\mathrm{M0}} = -\frac{\varepsilon_r - 1}{\varepsilon_r + 1}\frac{\pi\varepsilon_0 w^4 E_0^2}{16}\left\{\frac{1}{4z^2} - \frac{2z}{\left(4z^2 + w^2\right)^{\frac{3}{2}}}\right\}, \tag{3-3}$$

where z is the distance between the probe and sample. By considering time-dependent microwave $E_0 \sin \omega t$, the force should also be a time-dependent force as $F_{\mathrm{M0}} \sin^2 \omega t$. Because the frequency of cantilever vibration f_0 (~100 kHz) is much lesser than the microwave frequency ω (94 GHz), the time-dependent force functions as its root mean square value, i.e.,

$$F_{\mathrm{M}} = \frac{F_{\mathrm{M0}}}{2}. \tag{3-4}$$

On the other hand, atomic force F_A between the probes (with different regular shapes) and sample has different distance dependence. The atomic force of a cuboid probe is proportional to z^{-3}, whereas those of a spherical probe and a pyramid/cone-like probe are proportional to z^{-2} and z^{-1} [2,3], respectively. By considering the irregularity of a typical probe, the sum of these three terms, which contains all of these characteristics, can provide a reliable measurement. Therefore, the atomic force can be expressed as

$$F_{\mathrm{A}} = A_1 z^{-1} + A_2 z^{-2} + A_3 z^{-3}. \tag{3-5}$$

In the non-contact mode, the probe cantilever vibrates at its natural frequency, and the amplitude is limited to a few nanometers. When the probe approaches the sample, the atomic force influences this vibration. In small-amplitude approximation, the atomic force can be regarded as linear, and the relationship between the resonance-frequency variation of the cantilever Δf and the gradient of the atomic force along the z direction $\mathrm{d}F_{\mathrm{A}}/\mathrm{d}z$ can be expressed as follows [4]:

$$\Delta f = -\frac{f_0}{2k}\frac{\mathrm{d}F_A}{\mathrm{d}z}, \tag{3-6}$$

where k and f_0 are the spring constant and natural frequency of the cantilever, respectively. Here, we need to point out that the condition $\Delta f \ll f_0$ should be satisfied. Therefore, according to Eqs. (3-5) and (3-6), the gradient of the atomic force can be obtained as the following equation by measuring the variation in the resonance frequency:

$$-\frac{\mathrm{d}F_{\mathrm{A}}}{\mathrm{d}z} = \frac{2k}{f_0}\Delta f = A_1' z^{-2} + A_2' z^{-3} + A_3' z^{-4}. \tag{3-7}$$

Here, parameters A_1', A_2', and A_3' can be obtained by fitting the force curve measured under the no microwave condition. When a microwave is applied, the gradient of the resulting force should also be included, i.e.

$$\Delta f' = -\frac{f_0}{2k}\left(\frac{\mathrm{d}F_{\mathrm{A}}}{\mathrm{d}z} + \frac{\mathrm{d}F_{\mathrm{M}}}{\mathrm{d}z}\right). \tag{3-8}$$

Finally, according to Eqs. (3-3), (3-4), (3-7), and (3-8), the gradient of the force

mentioned above can be expressed as follows:

$$\frac{2k}{f_0}\Delta f' = A_1' z^{-2} + A_2' z^{-3} + A_3' z^{-4} + M \cdot H(z). \tag{3-9}$$

Here, parameter M and distance dependence $H(\mathrm{z})$ are expressed as

$$M = \frac{\varepsilon_r - 1}{\varepsilon_r + 1}\frac{\pi\varepsilon_0 w^4 E_0^2}{16} \tag{3-10}$$

and

$$H(z) = \frac{1}{2z^3} + \frac{2w^2 - 16z^2}{\left(4z^2 + w^2\right)^{\frac{5}{2}}}. \tag{3-11}$$

The parameter M can be determined by fitting the force curve measured in the presence of a microwave. Parameters A_1', A_2', and A_3' in Eq. (3-9) have been already obtained from the fitting result of Eq. (3-7). In Eq. (3-10), because the intensity of electric field E_0 cannot be directly measured, calibration is necessary. If the force curve of a material with known permittivity ε_{r1} is measured and parameter M_1 is obtained, relative permittivity ε_{r2} of an unknown material can be calculated from its parameter M_2 as follows:

$$\frac{M_1}{M_2} = \frac{\varepsilon_{r1} - 1}{\varepsilon_{r1} + 1} \cdot \frac{\varepsilon_{r2} + 1}{\varepsilon_{r2} - 1}. \tag{3-12}$$

3.4 Quantitative Evaluation of Permittivity of Dielectric Materials

According to the derivation above, the procedure of obtaining sample permittivity from force curve can be summarized as three steps. First, convert the frequency variation of probe to force gradient. Then fitting the curves with and without microwave to calibrate the zero-distance level and obtain the parameter *M* in Eq. 3-9. Finally, the permittivity of sample can be obtained with the aid of calibration material by Eq. 3-12.

Fig. 3-4 shows the results of the variation in the cantilever resonant frequency of Si, Al_2O_3, Ge, and ZrO_2 measured with no microwave and with 5-dBm and 10-dBm microwaves. It is shown that, under the condition without a microwave, the resonance frequencies of the probe for all materials decrease, which indicate that the atomic forces are attractive forces according to Eq. (3-6). Under the 5-dBm and 10-dBm microwave conditions, the curves present further decrease, indicating that the microwave-induced forces are also attractive. The variations in the frequencies are all less than 20 Hz, which satisfies the conditions in Eqs. (3-6) and (3-8). Therefore, the frequency variations can be converted into the gradient of the force by multiplying a coefficient $2k/f_0$, where $k = 182.6\ \mathrm{N/m}$, as calculated from the Young's modulus and geometric dimensions of the cantilever. $f_0 = 183.1\ \mathrm{kHz}$ is obtained from the tuning curve measured in the experiment.

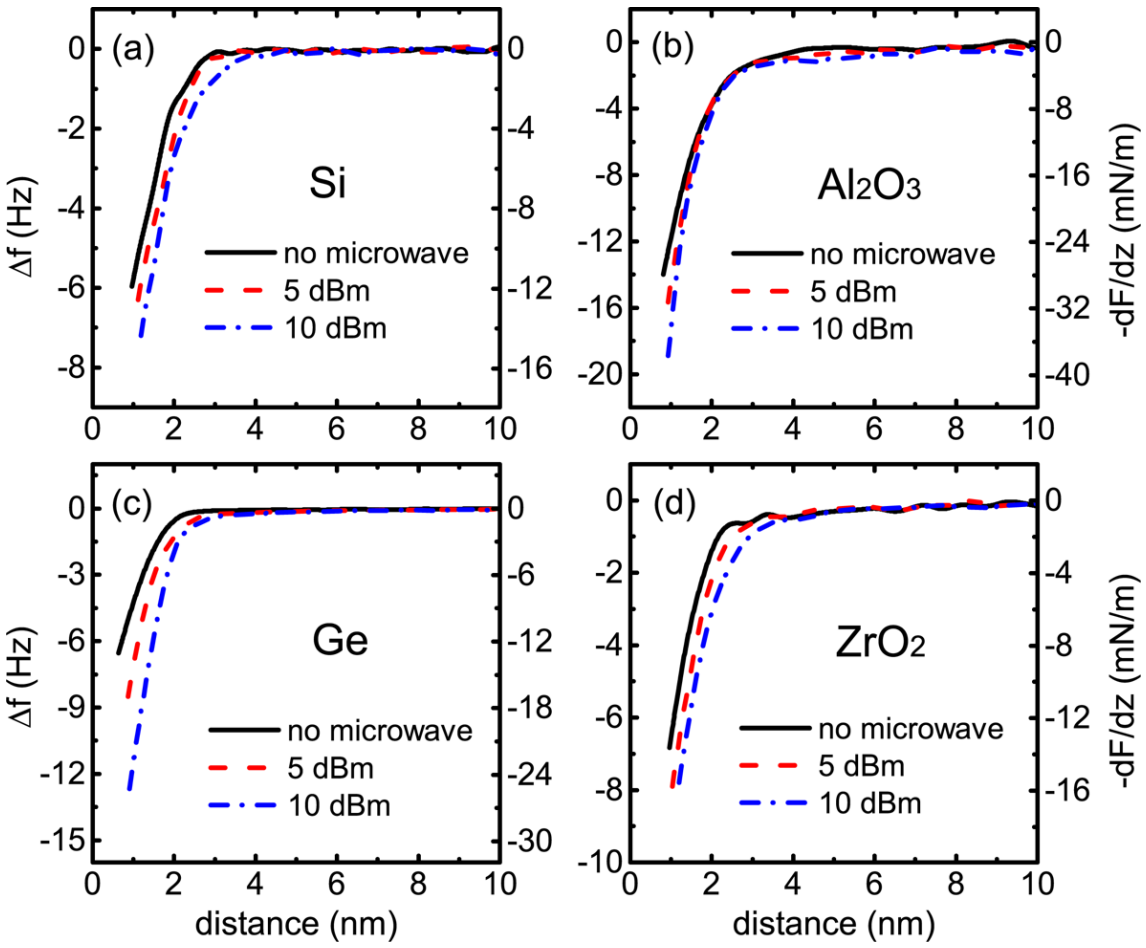

Figure 3-4: Force curve measurement results of Si, Al_2O_3, Ge and ZrO_2 with different microwave conditions.

To extract parameters $M_{5\,\mathrm{dBm}}$ and $M_{10\,\mathrm{dBm}}$, the curves without and with the microwaves are fitted using the following expressions:

$$-\frac{\mathrm{d}F_{\mathrm{A}}}{\mathrm{d}z} = A_1'\left(z+z_0\right)^{-2} + A_2'\left(z+z_0\right)^{-3} + A_3'\left(z+z_0\right)^{-4} \tag{3-13}$$

and

$$-\frac{\mathrm{d}F_{\mathrm{A}}}{\mathrm{d}z} - \frac{\mathrm{d}F_{\mathrm{M}}}{\mathrm{d}z} = A_1'\left(z+z_0\right)^{-2} + A_2'\left(z+z_0\right)^{-3} + A_3'\left(z+z_0\right)^{-4} + M\cdot H\left(z+z_0\right) \tag{3-14}$$

according to Eqs. (3-7) and (3-9), respectively. The parameter z_0 in Eqs. (3-13) and (3-14) is a fitting parameter that calibrates the zero-distance level of each measured force curve. The fitting results are shown in Fig. 3-5 following the measurement result. Using measured parameter M of Si and its nominal permittivity ($\varepsilon_r = 11$) in the calibration, the permittivity values of Al_2O_3, Ge, and ZrO_2 are obtained from their measured parameter M according to Eq. (3-12). Moreover, according to the calibration mentioned above, the amounts of power emitted at the tip are evaluated to be −29.9 and −21.0 dBm for the 5-dBm and 10-dBm source power, respectively. It is found that the attenuation of the 10-dBm source power is lower than that of the 5-dBm source power. The main reason is considered to be due to the enhancement effect of the electric field induced by the interaction between the tip and sample. Because of the Coulomb interaction, the charge on the tip is attracted by the charge in the sample to concentrate at the apex of the tip, which enhances the electric field near the tip of the probe. Therefore, the higher power induces a stronger attractive interaction and thus induces a stronger enhancement effect on the electric field, which results in a larger effect to compensate the attenuation of the power.

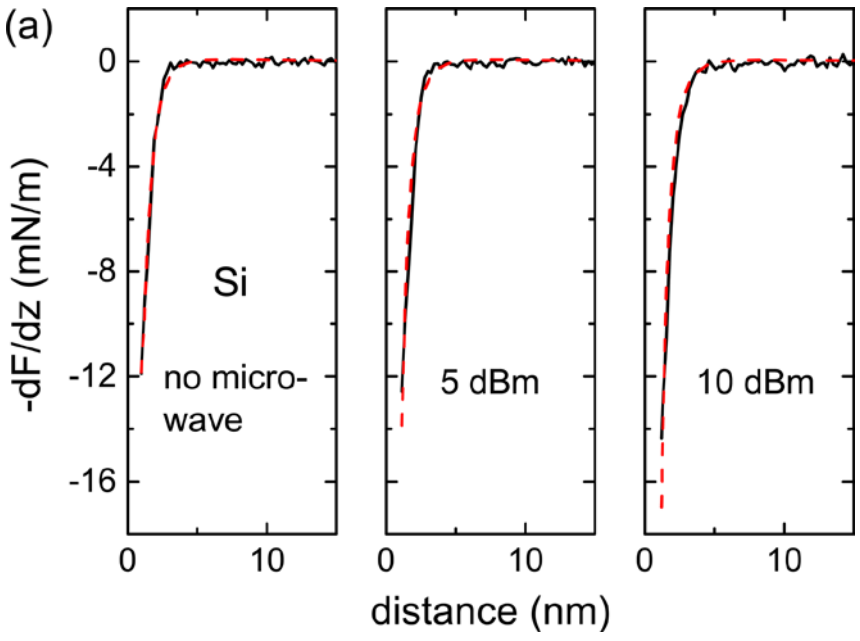

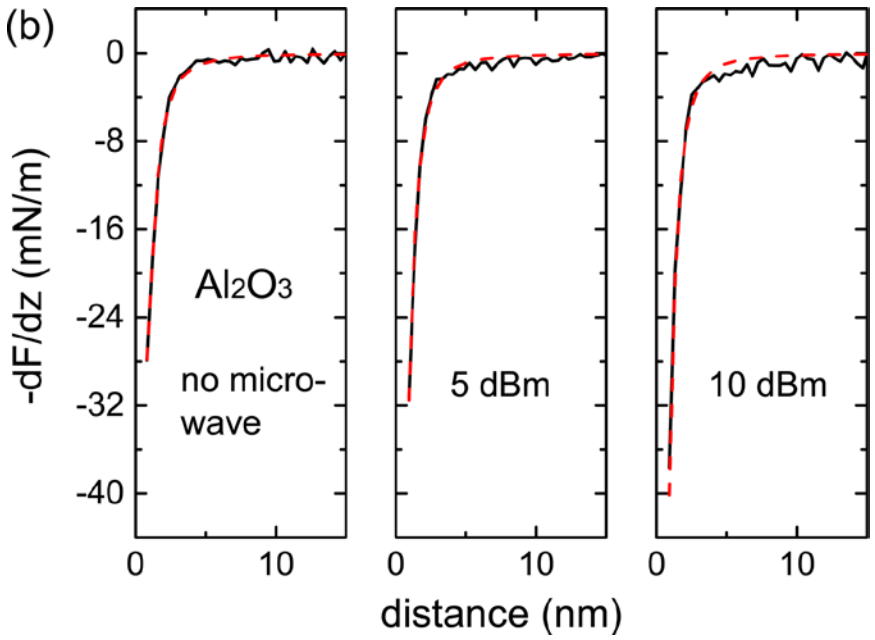
(b)
-dF/dz (mN/m)
0
-8
-16
-24
-32
-40
Al2O3
no micro-
wave
5 dBm
10 dBm
0
10
distance (nm)

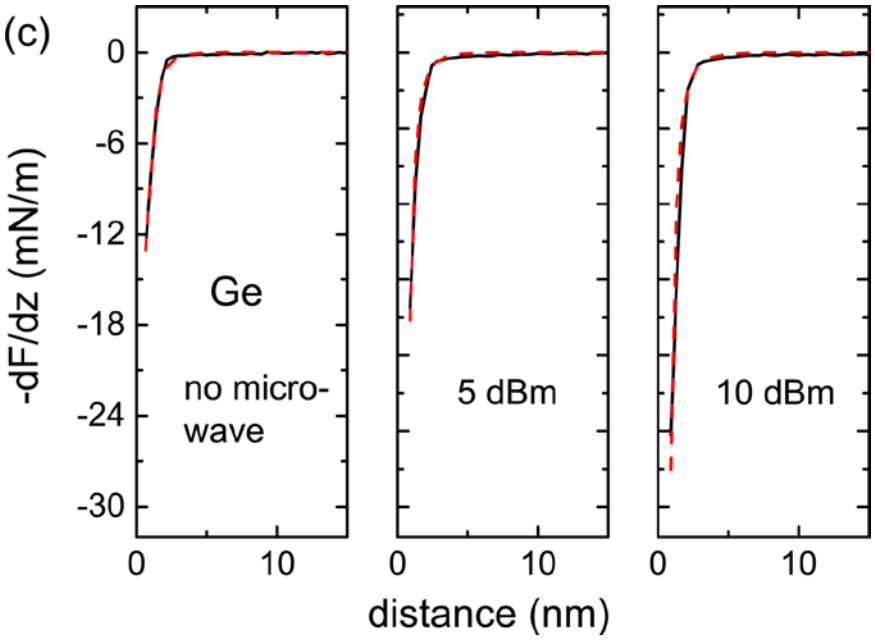
(c)
-dF/dz (mN/m)
0
-6
-12
-18
-24
-30
Ge
no micro-
wave
5 dBm
10 dBm
0
10
distance (nm)

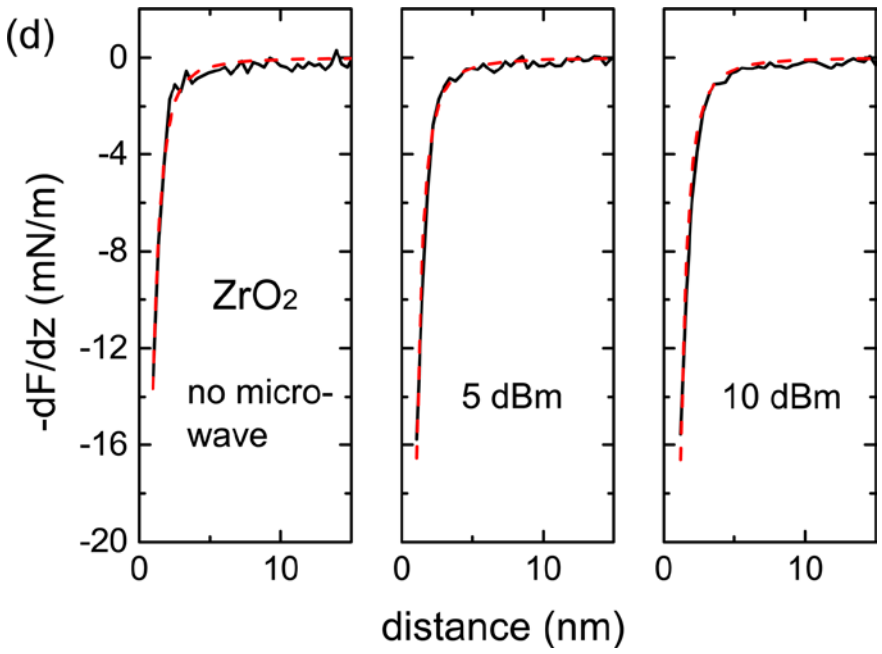

Figure 3-5: Fitting results of Si, Al_2O_3, Ge and ZrO_2 force curves.

The evaluated permittivity of these three materials versus their nominal values is shown in Fig. 3-6. The error bars of each material reflect the results of three measurements. We believe that the scatters of the measurement results are mainly due to the uncertainty of the tip–sample distance. Accurately determining this distance in the non-contact mode is difficult, but it can be improved by repeating the measurement. Fig. 3-6 shows that the deviations in the evaluated permittivity from the nominal value for Al_2O_3, Ge, and ZrO_2 are 7.320%, 10.583%, and 4.324% at 5 dBm and 8.436%, 5.987%, and 7.760% at 10 dBm, respectively. We consider that the deviations are induced by the several assumptions in the theoretical model. First, the microwave is assumed to be unrelated to the atomic force. However, because the microwave electric field induces additional potential to the electrons of the sample, which certainly perturbs their Hamiltonian, the London force between the probe and sample is also affected. Another reason is that the electric-field distribution at the tip of the probe is considered as a pair of opposite point charges based on near-field approximation to obtain a simple

analytical expression. Modeling the tip as a spherical apex and determining the radius using a simulation, as reported in Refs. [5] and [6], would yield a more refined charge distribution at the tip. Therefore, improving the accuracy of the distance dependence of the electromagnetic force and thus improving the accuracy of the dielectric properties of the test samples would be possible.

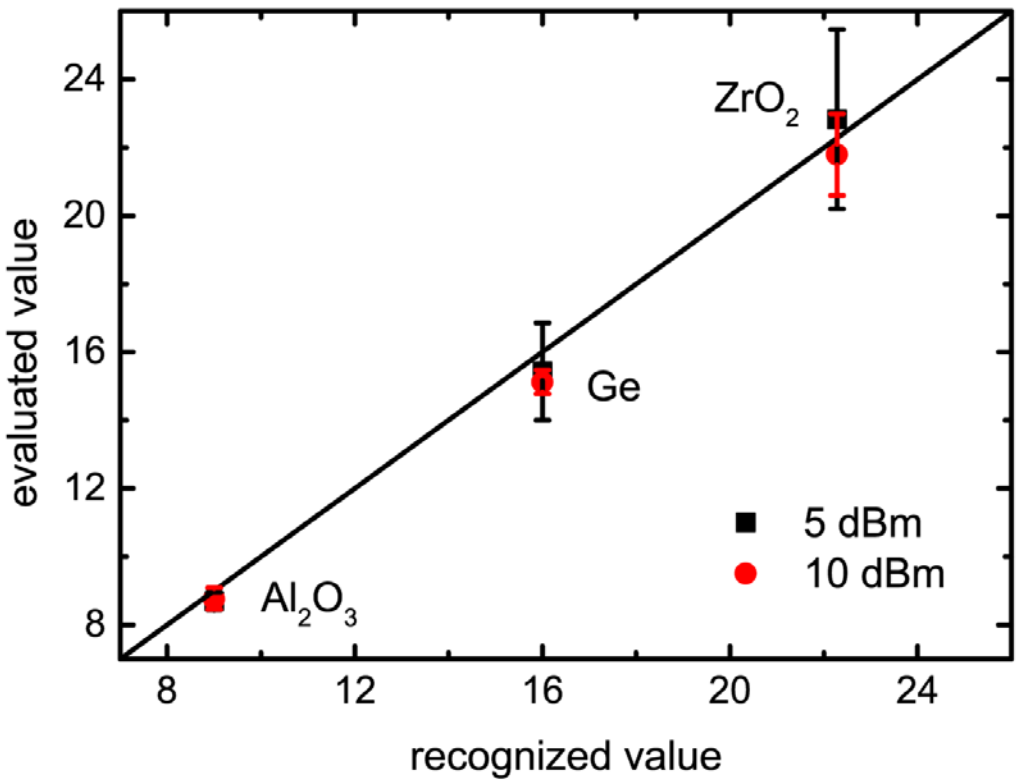

Figure 3-6: Comparison between the measured sample permittivity and their nominal values.

3.5 Summary

In this study, the effect of microwaves on the force interaction between the tip of a probe and a sample was analyzed by approximating the microwave as an electric field of a pair of sinusoidally alternating charges with opposite signs. According to this model, a quantitative distance dependence was obtained, which provided a prerequisite theoretical support for a non-contact evaluation in a near-field region. Moreover, the force gradient curves between the probe and four samples with no microwave and with 5-dBm and 10-dBm microwaves were measured using a nanometer-scale M-AFM probe in the non-contact force curve mode, and the variation in the force curves caused by the microwave was observed. By fitting the measurement results, the local permittivity values of Al_2O_3, Ge, and ZrO_2 were quantitatively obtained, which provide a new possibility for a non-contact quantitative evaluation of the local permittivity of dielectric materials.

References

1) R. P. Feynman, R. B. Leighton, and M. Sands. The Feynman Lectures on Physics: Mainly Electromagnetism and Matter Vol. 2. *Addison-Wesley, Reading*, (1977).
2) S. I. Zanette, A. O. Caride, V. B. Nunes, G. L. Klimchitskaya, F. L. Freire, and R. Prioli. Theoretical and experimental investigation of the force‐distance relation for an atomic force microscope with a pyramidal tip. *Surf. Sci.* **453**, 75-82 (2000).
3) H. J. Butt, B. Cappella, and M. Kappl. Force measurements with the atomic force microscope: Technique, interpretation and applications. *Surf. Sci. Rep.* **59**, 1-152 (2005).
4) F. J. Giessibl. Advances in atomic force microscopy. *Rev. Mod. Phys.* **75**, 949 (2003).
5) G. Gramse, E. Brinciotti, A. Lucibello, S. B. Patil, M. Kasper, C. Rankl, R. Giridharagopal, P. Hinterdorfer, R. Marcelli, and F. Kienberger. Quantitative sub-surface and non-contact imaging using scanning microwave microscopy. *Nanotechnology* **26**, 135701 (2015).
6) X. Wu, Z. Hao, D. Wu, L. Zheng, Z. Jiang, V. Ganesan, Y. Wang, and K. Lai. Quantitative measurements of nanoscale permittivity and conductivity using tuning-fork-based microwave impedance microscopy. *Rev. Sci. Instrum.* **89**, 043704 (2018).

Chapter 4 Non-contact Local Conductivity Measurement of Metallic Nanowires Based on Semi-near-field Reflection of M-AFM

4.1 Introduction

In the last chapter, the evaluable material of M-AFM was expanded from metal to dielectric material. In this chapter, the evaluation method for conductivity of metallic materials was developed in order to apply it from bulk materials to nanowires. As explained in Chapter 2, we used a coaxial probe in this study and the microwave images and topography images were simultaneously obtained for three metallic nanowires in non-contact scanning mode. A semi-near-field model was established to describe the distribution of electric field between the probe and the sample, which depends on the diameter of the nanowire. Based on this model, the local conductivities of metallic nanowires on the nanometer-scale were quantitatively evaluated in a single scan, using a metal strip substrate to calibrate the reflected signal.

4.2 Experiment Approach

In the measurement experiment, Al, Ag and Cu nanowires with diameters of 660 nm, 240 nm and 720 nm were prepared, respectively. Each sample was scanned under non-contact mode on a Pt substrate with Au strips, which can contribute to the calibration of reflected signal. Both the width and the interval of the strips were 5 μm. The scanning speed was 3 μm/s and the scanning area was 10×10 μm^2 for the Ag nanowire and 20×20 μm^2 for the Al and Cu nanowires, based on their sizes. A TEM

microwave having 10 dBm source power was applied to the probe by a generator as input signal. The frequency was set to be 94 GHz to match the optimum transmission frequency of the wave guide [1,2]. The microwave reflected by the sample is received by a detector, and as explained in Chapter 1 the output voltage of the detector can be represented as

$$V = k_0 \left|E\right|^2 + b_0 . \tag{4-1}$$

Here E is the intensity of reflected signal and k_0, b_0 are constant parameters of the detector. The measurement was conducted in air and the environmental temperature and the relative humidity is 20.0 ℃ and 50%, respectively.

4.3 Semi-near-field Model for the Description of Reflected Microwave

4.3.1 Reflection from Strips and the Substrate

As explained in Chapter 3, the electric fields of the incident and reflected microwave are within near-field range and the spatial distribution of microwave should be described by a near-field model to improve accuracy. At every instant the electric field of the incident and reflected microwave can be approximated as quasi-static fields produced by the original charge on the probe and the polarization charge on the sample, respectively. Again, the polarization charge can still be described using the image charges model [3]. Here, we still refer to the amplitude since there is no phase difference within the near-field range. If a single point charge q_1 is located above the surface of a metallic flat sample at a distance z_1, the image charge q_2 and its position can be decided as

$$q_2 = -q_1 \tag{4-2}$$

and

$$z_2 = z_1, \tag{4-3}$$

respectively. Here, z_2 is the distance of image charge q_2 from the surface. Here a prerequisite is that the metallic sample should be grounded. It is realized in experiment by using a metallic sample stage which is connected with the M-AFM housing and the ground. Therefore, when the probe is located over the strips or the substrate, which can be regarded as an infinite and isotropic plane within the size of the tip, the image charge of every charge element on the tip determined by Eqs. (4-2) and (4-3) forms a simple mirror-symmetrical image of the tip. In this experiment, since the length of the tip is much larger than the diameter of the aperture, the boundary area near the aperture can be approximated to a regular coaxial structure, and charges mainly exist on the outer surface of the inner conductor and the inner surface of the outer conductor. Thus, the image charges should have the same double-tube-like distribution, as shown in Fig. 4-1.

However, it should be pointed out that in this thorough near field model the image charge is independent from the conductivity of the sample, because all metals reach the same electrostatic equilibrium state at every instant regardless of their conductivities. It means this model can only describe the distribution of the electrical field for metallic materials. In order to describe the conductivity dependence of the reflected wave, the reflection coefficient Γ of the sample, which is derived from the Maxwell equations, is introduced to establish a semi-near-field model. On the surface of metallic materials, the reflected wave E_1 and the incident wave E_0 should obey the law of reflection as [4]

$$\Gamma = \frac{E}{E_0} = \frac{1-\sqrt{\sigma / j\omega\varepsilon_0}}{1+\sqrt{\sigma / j\omega\varepsilon_0}}, \tag{4-4}$$

where j, ε_0, σ, and ω are the imaginary unit, permittivity of vacuum, conductivity of sample and frequency of the microwave, respectively. Combining Eq. (2) and Eq. (4), the image charge depending on both the tip-sample distance and conductivity of material can be represented as

$$q_2 = -|\Gamma| q_1. \tag{4-5}$$

Consequently, considering q_1 as a charge element on the tip, the reflected microwave can be calculated as the electric field integral of q_2 using the Coulomb law. Therefore, the reflected wave from a flat metallic surface has the following form:

$$E_{\text{sub}} = \frac{|\Gamma|}{4\pi\varepsilon_0}\left\{\int_{z_a}^{z_b} \frac{\rho_{i1}\left(z_0+z_{i1}\right)dz_{i1}}{\left[\frac{w_{i1}^2}{4}+\left(z_0+z_{i1}\right)^2\right]^{3/2}} + \int_{z_c}^{z_d} \frac{\rho_{o1}\left(z_0+z_{o1}\right)dz_{o1}}{\left[\frac{w_{o1}^2}{4}+\left(z_0+z_{o1}\right)^2\right]^{3/2}}\right\}, \tag{4-6}$$

where z_{i1}, ρ_{i1} and w_{i1} are the vertical distance of a charge element on the inner conductor from a nanowire surface, the linear charge density along the inner conductor and the diameter of the inner conductor, respectively. ρ_{i1} and w_{i1} are the corresponding quantities for the outer conductor. z_0 is the vertical distance of the tip apex from the substrate surface. z_a, z_b, z_c, and z_d represent the boundary region from the apex of the inner conductor and the outer conductor, as shown in Fig. 4-1. Here, the calculated electrical field is the reflected wave at the center of the tip, which represents the signal received by the probe and propagated to the detector. It should be mentioned that although z_0 is not constant in the experiment because of the vibration of the probe working in non-contact mode, it can be considered as a constant by using

its average value. As the final reflected signal detected by the detector is converted to a direct-current voltage signal via a rectification amplifier, the measured signal only corresponds to the microwave signal obtained at the average position of the tip vibration. Based on the conservation of charge, the charge density on the boundary area of the tip follows

$$\rho_{i1}\left(z_b - z_a\right) = -\rho_{o1}\left(z_d - z_c\right). \tag{4-7}$$

In calculation, the depth of the boundary area is considered to be the same as the width of the aperture, which implies that $z_b - z_a = z_d - z_c = w_{o1}$.

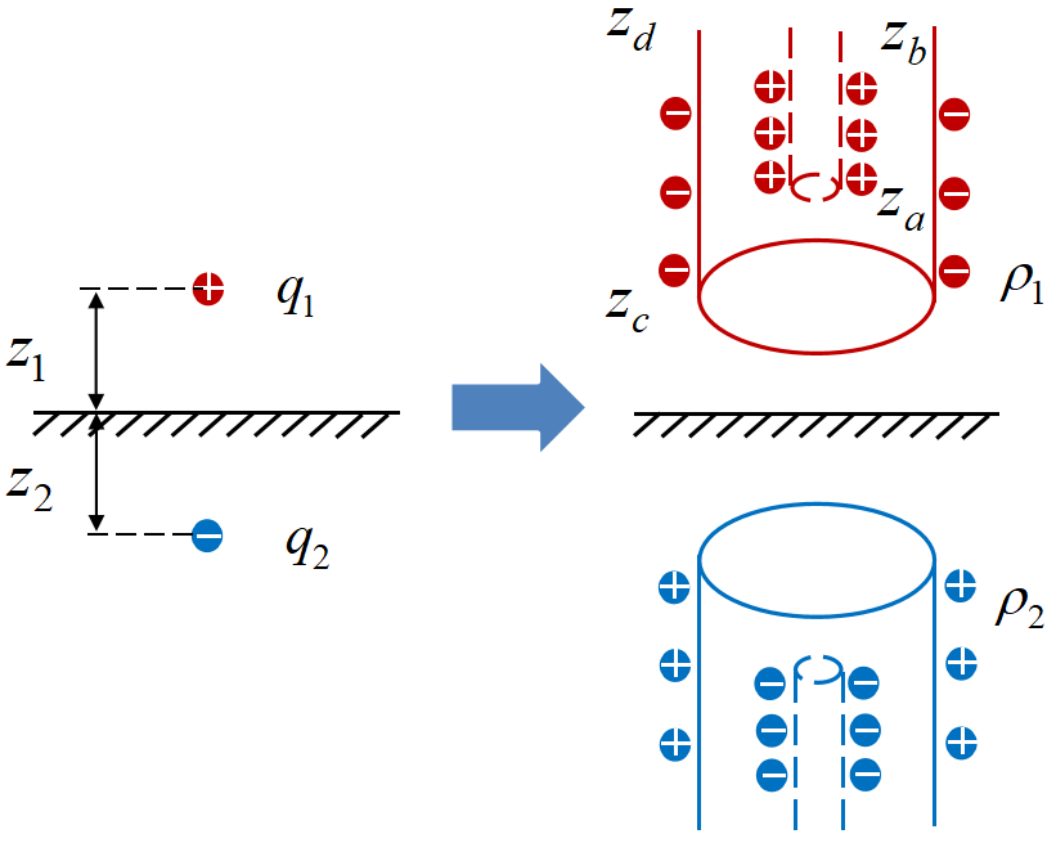

Figure 4-1: The schematic of image charge of a coaxial probe on a flat surface.

4.3.2 Reflection from Nanowire Sample and Evaluation of Conductivity

When the probe is located over a metallic nanowire sample, the distribution of reflected microwave deforms because of the curved surface. However, it is impossible to find an image charge to represent the electric field of the polarization charges on a surface of cylinder. Since this method is a local evaluation, only the local area of the nanowire right under the tip is evaluated. Therefore, if the diameter of the nanowire is $2r$, the surface can be approximated to be a spherical surface with the same diameter. If a single point charge is located above a metallic sphere surface, Eqs. (4-2) and (4-3) which describes the image charge should be rewritten as

$$q_2 = -\frac{r}{z_1 + r} q_1 \tag{4-8}$$

and

$$z_2 = \frac{z_1 r}{z_1 + r}, \tag{4-9}$$

respectively. Next, introducing the reflection coefficient of the sample to this model, Eq. (4-5) can be rewritten as

$$q_2 = -\frac{r}{z_1 + r} |\Gamma| q_1 . \tag{4-10}$$

In this case, the image charges of the charge elements on the probe turn out to be a double-trumpet-like distribution as shown in Fig. 4-2. The double-trumpet-like distribution can be described by the following equations. If z_{i1}, ρ_{i1} and w_{i1} express

the vertical distance of a charge element on the inner conductor from a nanowire surface, the linear charge density along the inner conductor and the diameter of the inner conductor, respectively, the corresponding quantities of its image charge element in the nanowire sample, which are represented as z_{i2}, ρ_{i2} and w_{i2}, can be calculated as

$$z_{i2} = r - \frac{r^2\left(r + z_{i1}\right)}{\left(w_{i1}/2\right)^2 + \left(r + z_{i1}\right)^2}, \tag{4-11}$$

$$\rho_{i2} = \frac{r}{\sqrt{\left(w_{i1}/2\right)^2 + \left(r + z_{i1}\right)^2}}\rho_{i1}, \tag{4-12}$$

and

$$w_{i2} = \frac{r^2}{\left(w_{i1}/2\right)^2 + \left(r + z_{i1}\right)^2}w_{i1}. \tag{4-13}$$

The corresponding quantities of the outer conductor z_{o2}, ρ_{o2} and w_{o2} also have the same relationship with z_{o1}, ρ_{o1} and w_{o1}. Therefore, using Coulomb law the reflected wave from a nanowire sample has the following form:

$$E_{\text{wire}} = \frac{|\Gamma|}{4\pi\varepsilon_0}\left\{\int_{z_a}^{z_b}\frac{\rho_{i2}\left(z_0 + z_{i2}\right)\mathrm{d}z_{i1}}{\left[\frac{w_{i2}^2}{4} + \left(z_0 + z_{i2}\right)^2\right]^{3/2}} + \int_{z_c}^{z_d}\frac{\rho_{o2}\left(z_0 + z_{o2}\right)\mathrm{d}z_{o1}}{\left[\frac{w_{o2}^2}{4} + \left(z_0 + z_{o2}\right)^2\right]^{3/2}}\right\}. \tag{4-14}$$

Finally, by substituting Eq. (4-1) into (4-6), the relation between the output voltage of the detector and reflection coefficient of the substrate and Au strip can be expressed as

$$V = k_1 k_{\text{sub}} \left|\Gamma\right|^2 + b_0, \tag{4-15}$$

while the corresponding relation for a nanowire sample is

$$V = k_1 k_{\text{wire}} \left|\Gamma\right|^2 + b_0. \tag{4-16}$$

Here, k_1 represents a performance parameter of M-AFM which is determined by k_0 and the charge on the tip. k_{sub} and k_{wire}, however, represent the near field effect on the spatial distribution and can be calculated by the geometric parameter of the probe and sample as

$$k_{\text{sub}} = \left\{ \int_{z_a}^{z_b} \frac{\left(z_0 + z_{i1}\right)/\left(z_b - z_a\right) \mathrm{d}z_{i1}}{\left[\frac{w_{i1}^2}{4} + \left(z_0 + z_{i1}\right)^2\right]^{3/2}} - \int_{z_c}^{z_d} \frac{\left(z_0 + z_{o1}\right)/\left(z_d - z_c\right) \mathrm{d}z_{o1}}{\left[\frac{w_{o1}^2}{4} + \left(z_0 + z_{o1}\right)^2\right]^{3/2}} \right\}^2 \tag{4-17}$$

and

$$k_{\text{wire}} = \left\{ \int_{z_a}^{z_b} \frac{r}{\sqrt{\frac{w_{i1}^2}{4} + \left(r + z_{i1}\right)^2}} \frac{\left(z_0 + z_{i2}\right) / \left(z_b - z_a\right) \mathrm{d}z_{i1}}{\left[\frac{w_{i2}^2}{4} + \left(z_0 + z_{i2}\right)^2\right]^{3/2}} \right.$$

$$\left. - \int_{z_c}^{z_d} \frac{r}{\sqrt{\frac{w_{o1}^2}{4} + \left(r + z_{o1}\right)^2}} \frac{\left(z_0 + z_{o2}\right) / \left(z_d - z_c\right) \mathrm{d}z_{o1}}{\left[\frac{w_{o2}^2}{4} + \left(z_0 + z_{o2}\right)^2\right]^{3/2}} \right\}^2 , \qquad (4\text{-}18)$$

respectively. In experiment, the charge on the tip strongly depends on the probe and the wave guide; k_0 and b_0 in Eq. (4-1) are also affected by the environment. Therefore, k_1 and b_0 have to be calibrated for every measurement. In order to simplify the calibration, the striped substrate composed of two reference materials with known conductivities was scanned together with nanowire samples. Using the conductivities of the two reference materials, their theoretical value of $|\Gamma|^2$ can be calculated by Eq. 4-4. k_{sub} and k_{wire} can be calculated by the structure parameters of the probe using Eqs. (4-17) and (4-18). Then k_1 and b_0 can be calibrated using Eqs. (4-15) from the measured voltage of the reference materials on the substrate. Then, $|\Gamma|^2$ of the nanowire samples can be evaluated based on their measured voltages using Eqs. (4-16), thereby conductivities of these materials can be obtained from Eq. (4-4).

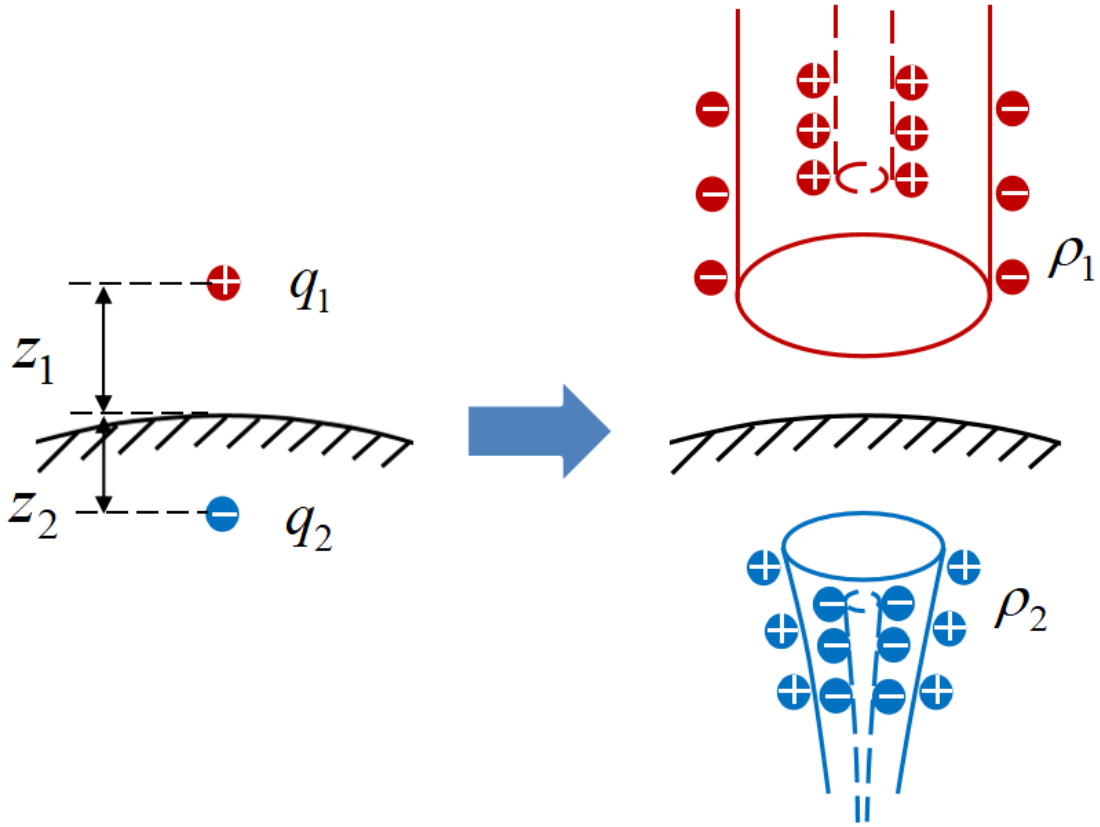

Figure 4-2: The schematic of image charge of a coaxial probe on a spherical surface.

4.4 Evaluation of Metallic Nanowire Conductivity

4.4.1 Anomaly of Aluminum Nanowire

The scanning topography image and microwave image of three metallic nanowire samples, Al, Ag, and Cu, were measured simultaneously by M-AFM, as shown in Fig. 4-3, 4-4 and 4-5. It is observed that the microwave image corresponds to the topography image clearly, which confirms that this coaxial probe can emit microwave. The average output voltage along the center line of each strip or nanowire were extracted as the

criterion of the intensity of reflected microwave, which can avoid the measurement error caused by the instability near the boundary. The output voltages versus the standard conductivity of respective materials are shown in Fig. 4-6(a), (b) and (c). Here, as the thicknesses of the film and strips on the substrate are 300 nm and the diameters of all the nanowires are more than 200 nm, size effect of conductivity is not considered. The standard conductivities are referred from the values of corresponding bulk materials [5,6]. Since the microwave signal strongly depends on the tip-sample distance and microwave transmission line, the error bar of the averaged reflected voltage signal mainly comes from the small change of standoff distance and transmission line impedance of different scanning. One abnormal phenomenon to be noted is the discordance of the Al nanowire. According to Eqs. (4-4), (4-15) and (4-16), the reflected voltage signal depends on the conductivity of the material monotonously. However, although the true conductivity of Al is lower than that of Au and higher than that of Pt, the measured reflected voltage signal of the Al nanowire is higher than that of both Pt substrate and Au strip, as shown in Fig. 4-6(a). This is because the curved surface of the nanowire generates a trumpet-like image charge that is more concentrated under the tip, as shown in Fig. 4-2, and thus generates a stronger reflected wave than the plane surface of the strip dose. In evaluation, the different near-field distribution of the plane surface and curved surface causes k_{wire} in Eq. (4-16) is slightly higher than k_{sub} in Eq. (4-15).

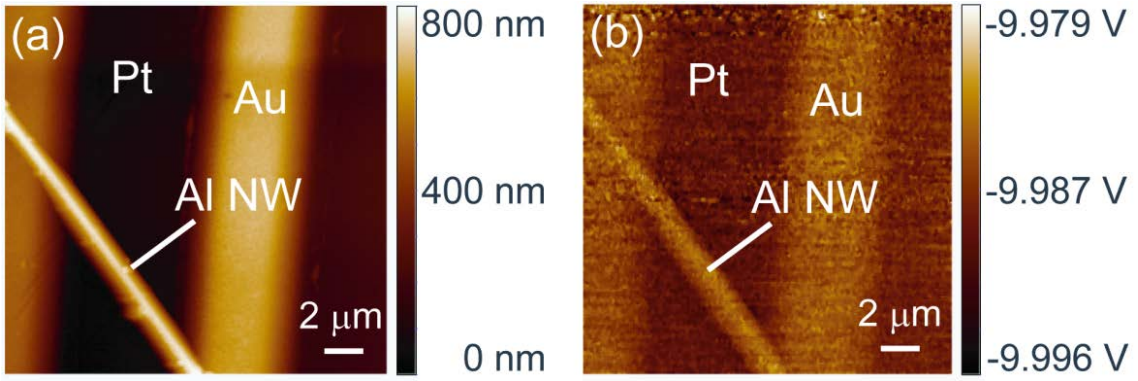

Figure 4-3: The topography and microwave images of the Al nanowire on the Pt/Au substrate.

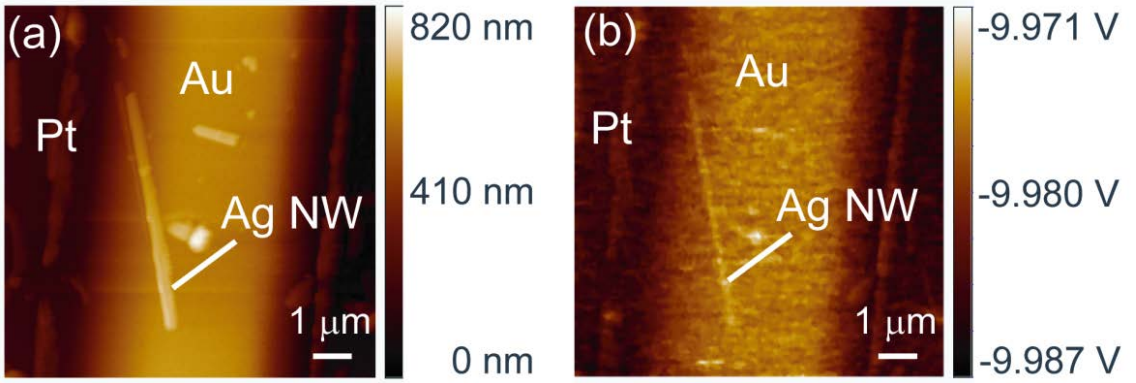

Figure 4-4: The topography and microwave images of the Ag nanowire on the Pt/Au substrate.

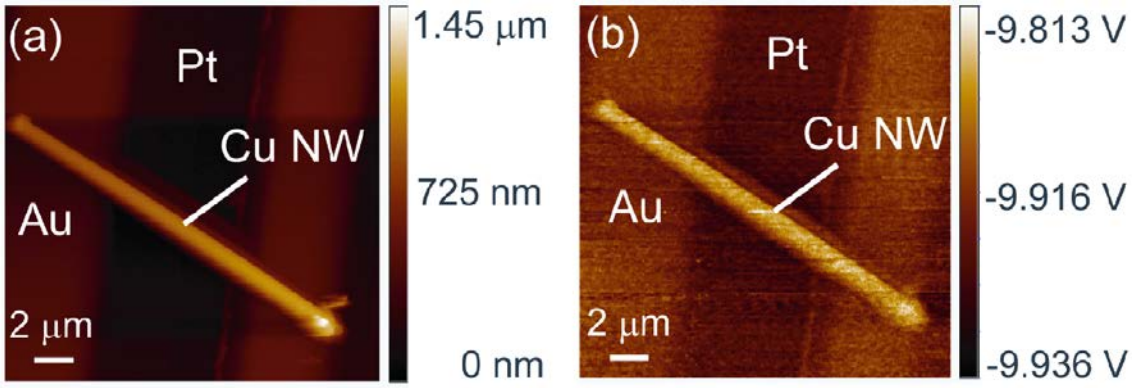

Figure 4-5: The topography and microwave images of the Cu nanowire on the Pt/Au substrate.

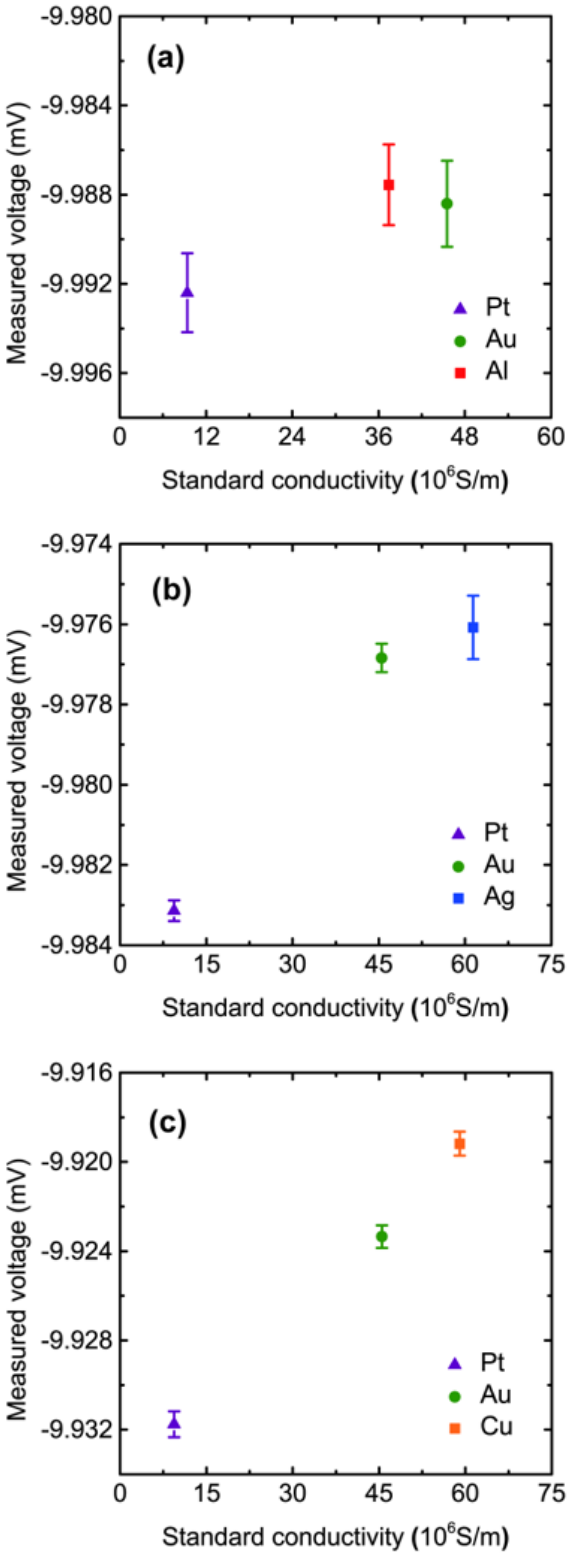

Figure 4-6: Reflected voltage signals of the Al (a), Ag (b), and Cu (c) nanowire samples and Pt/Au substrate, with respect to their standard conductivities.

4.4.2 Quantitative Evaluation Results

In terms of quantitative evaluation, we first calculate k_{sub} and k_{wire} based on the parameters of the tip. Then, the measured voltage can be converted to reflection coefficient by calibration using Eqs. 4-15 and 4-16. Finally, the conductivity of sample can be obtained from reflection coefficient by Eq. 4-4.

According to Eqs. (4-17) and (4-18), k_{sub} of the substrate is calculated to be 1.56070×10^{10} m^{-2} and k_{wire} of the three nanowire samples are 1.56138×10^{10} m^{-2} for Al, 1.56083×10^{10} m^{-2} for Ag and 1.56133×10^{10} m^{-2} for Cu, respectively. Here, w_{i1} was determined to be 5 nm according to the beam size of FIB etching; w_{o1} was determined to be 250 nm according to the aperture size of the tip; z_0 was determined to be 5 nm based on the force curve measurement. Using the standard conductivities and reflected voltage signal of Pt substrate and Au strip, the two undetermined parameters k_1 and b_0 of each measurement were calibrated using Eqs. (4-4) and (4-15). Subsequently, $|\Gamma|^2$ of Al, Ag and Cu nanowire, can be determined from their measured output voltages by Eqs. (4-16). The results are shown in Fig. 4-7(a), (b) and (c) with the $|\Gamma|^2$ of Au and Pt as comparison versus their standard conductivities, respectively. From these results it is confirmed that the reflection coefficient on the surface of the sample and substrate depends on the conductivity of materials monotonously after the near field factor k_{sub} and k_{wire} is stripped. Therefore, the semi-near-field model is demonstrated to be appropriate for the description of the electric field distribution of M-AFM probe.

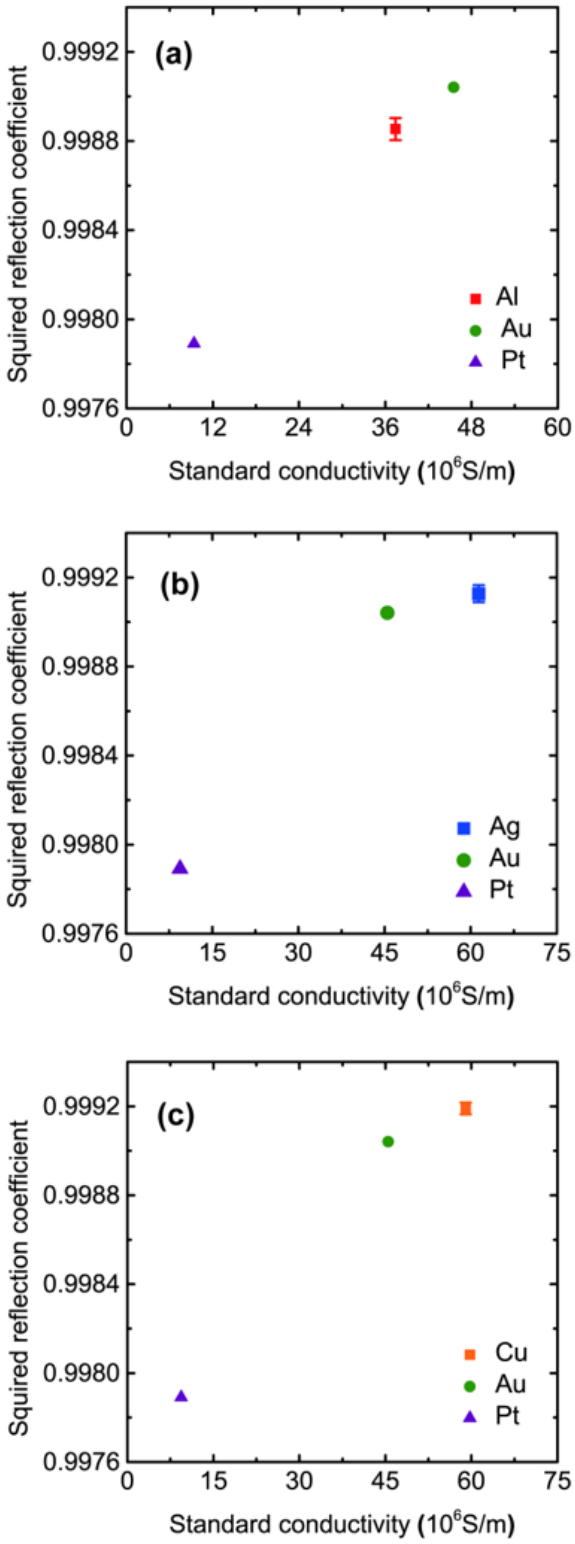

Figure 4-7: Evaluated $|\Gamma|^2$ of the Al (a), Ag (b), and Cu (c) nanowire samples compared with the theoretical $|\Gamma|^2$ values of Au and Pt.

Further, the conductivities of the three nanowire samples can be calculated from their surface reflection coefficient using Eq. (4-4). The evaluated results are shown in Fig. 4-8 versus their standard values. The deviation of the evaluated conductivities from the standard values for Al, Ag, and Cu nanowires are 14.21%, 10.26%, and 8.57%, respectively. The reasons of the deviations come from both theoretical reason and experimental reason. Firstly, the spatial distribution of the microwave was calculated based on a quasi-static charge model. In near field condition, as part of the electrical interaction between the charges on the tip and the sample, the reflected wave should also impact the charge distribution on the tip. It was omitted in this model and the charge density was assumed to be constant for simplification. Secondly, the experimental reason is that the shape of the fabricated tip is not as regular and symmetric as we designed because it is nearing the resolution limit of wet etching and FIB etching, which also impacts the true distribution of microwave.

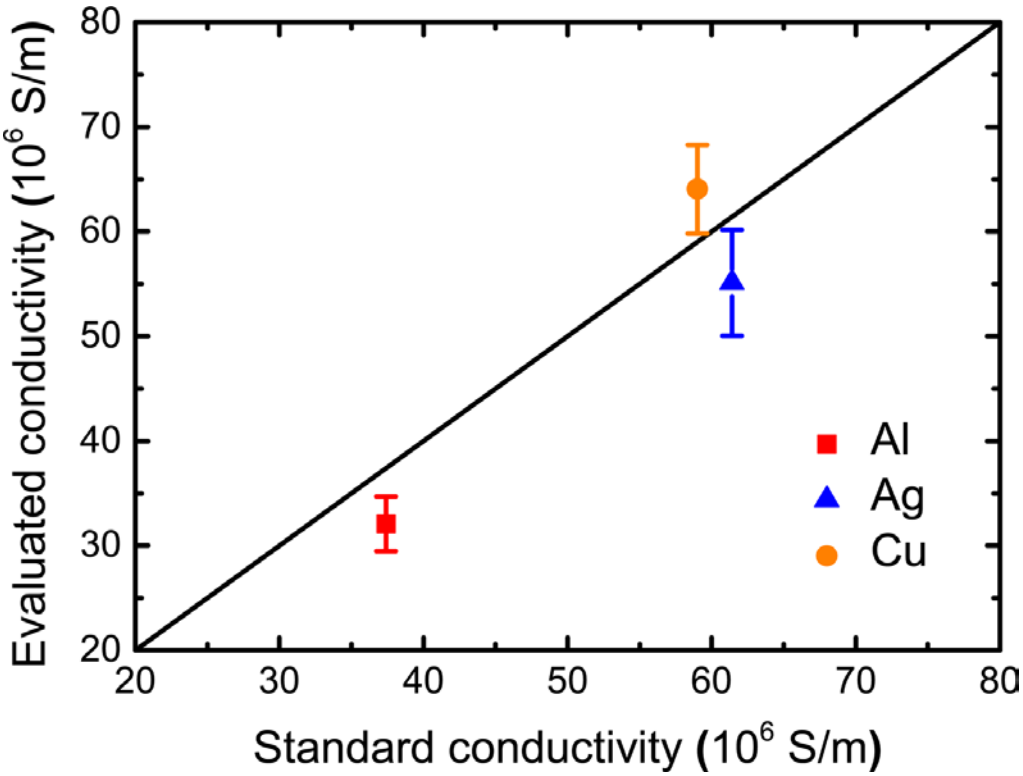

Figure 4-8: Evaluated conductivities of the Al, Ag, and Cu nanowires compared with their standard values.

4.5 Summary

In this study, a novel coaxial probe with high sensitivity was fabricated by wet etching and FIB etching. Using this coaxial probe the topography image and reflected microwave image of Al, Ag, and Cu nanowires were simultaneously obtained under non-contact mode of M-AFM. The measurement was conducted on a Pt substrate with Au strips for calibration. A semi-near-field model based on the image charge method and reflection coefficient was established to describe the spatial distribution and conductivity dependence of a microwave between the tip and sample. This is essential for non-contact quantitative measurements and may overcome the impact of nanowire diameter on measurement results. Through the calibration technique and expressions of theoretical model, for the first time, the non-contact local conductivity evaluation of metallic nanowires was quantitatively achieved within a single scan. This indicates that M-AFM is a promising in-situ method for the characterization of one-dimensional nanomaterials.

References

1) Y. Ju, T. Kobayashi, and H. Soyama. Development of a nanostructural microwave probe based on GaAs. *Microsyst. Technol.* **14**, 1021-1025 (2008).
2) Y. Ju, M. Hamada, T. Kobayashi, and H. Soyama. A microwave probe nanostructure for atomic force microscopy. *Microsyst. Technol.* **15**, 1195-1199 (2009).
3) R. P. Feynman, R. B. Leighton, and M. Sands. The Feynman Lectures on Physics: Mainly Electromagnetism and Matter Vol. 2. *Addison-Wesley, Reading* (1977).
4) D. M. Pozer. Microwave Engineering 2nd ed. *Wiley, New York* (1998).
5) R. A. Serway, and J. W. Jewett. Principles of physics. *Saunders College Pub, Fort Worth* (1998).
6) R. A. Matula. Electrical resistivity of copper, gold, palladium, and silver. *J. Phys. Chem. Ref. Data* **8**, 1147 (1979).

Chapter 5 Theoretical Analysis and Simulation of Near-Field Microwave Distribution for M-AFM Probes

5.1 Problems of Plane Wave Model and Necessity of Simulation

As mentioned in the previous chapters, during the measurement of M-AFM, the distance between the sample and probe (less than 10 nm) is much shorter than the wave length of microwave (about 3 mm). In this near-field case, a non-negligible challenge of noncontact evaluation by M-AFM is that a very small variation of the distance between the tip and sample (even as small as 1 nm) may vastly impact the intensity of microwave applied on the sample. However, the plane wave model cannot express an intensity change caused by a distance change at a scale much smaller than the wave length. Besides the inaccurate description of spatial distribution, another important problem is that in plane wave model and near-field model the dependence of reflected microwave and transmitted microwave on electrical property of sample materials are different. It is essential especially for the quantitative evaluation of dielectric materials. In experiment, it is rather difficult to evaluate the electrical field distribution of reflected microwave near the tip of the probe within a range of several tens of nanometer. It is also impossible to measure the transmitted field inside the sample. Therefore, the simulation result of M-AFM probe using commercial software ANSYS HFSS in finite element method (FEM) are expected to provide indispensable information to improve the theoretical model and probe design for M-AFM.

5.2 Theoretical Analysis and Modeling

5.2.1 Theoretical Model

In M-AFM, the probe is designed as the combination of AFM probe and the wave guide [1,2]. The slit structure probe corresponds to the parallel plate wave guide while the coaxial structure probe corresponds to the coaxial wave guide. For both types of probe, by covering the surface with gold film the microwave is confined inside the probe until emitted from the aperture at the end of the tip. The schematic of the microwave distribution of the two types of probe in plane wave model and near field model are shown in Fig. 5-1 and 5-2. In plane wave model, the microwave is regarded as electromagnetic field with no divergence, and the reflected microwave and transmitted microwave are obtained from boundary condition on the sample surface. In near-field model, however, as mentioned in the previous chapters, the incident microwave and reflected microwave are regarded as the electric field of charges on the tip and the polarization charges on the sample, respectively. In addition, in the same opinion, the transmitted wave which is inside the sample can be regarded as the superposition of the electric field of the charges on the probe and on the sample. In order to demonstrate that the near field model can provide a more accurate description of the spatial distribution of electric field, the electric field calculated by charges on the tip and sample would be compared with the simulation result of FEM. To make the theoretical model more accurate, the electric field will be calculated by integration of charge element instead of simplified point charge.

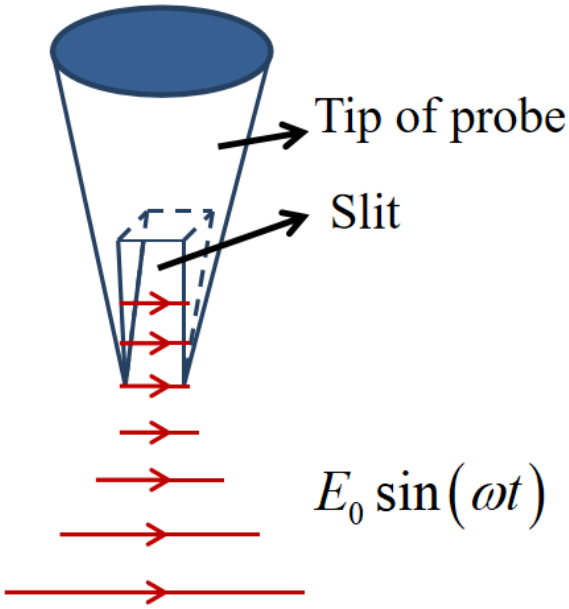

Figure 5-1: The schematic of plane wave distribution of slit probe.

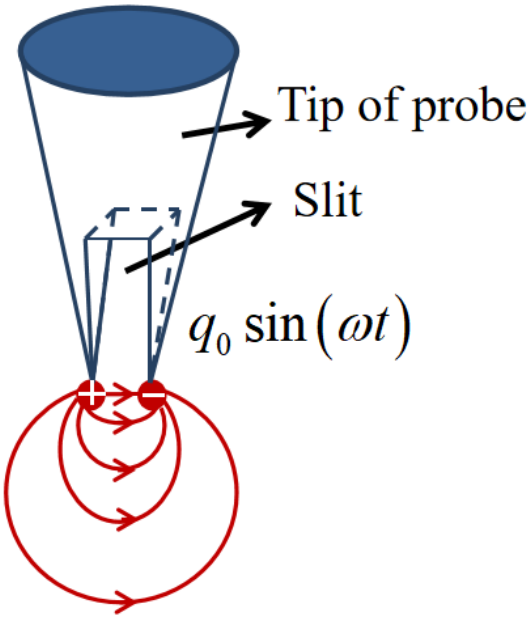

Figure 5-2: The schematic of near-field distribution of slit probe.

5.2.2 Simulation Principle and Modelling for Probes

The simulation in this research is based on finite element method (FEM), which is a numerical calculation method widely used in physics and engineering problems. The basic idea of the method is to mesh the space to be simulated into a finite number of elements. For every element, the values of the simulated physical quantity at the nodes are related by the liner approximation of the governing equation. For electromagnetic simulation in this thesis, the simulated physical quantity is intensity of electric field and the governing equation is Maxwell equations. In this way, a continuous differential equation with infinite degree of freedom is converted into discrete linear equations with finite degree of freedom. Combining with the boundary condition, the values at the nodes can be solved. The values inside every element can be obtained by the interpolation of the values at the nodes. In this research, the simulation was conducted using commercial software ANSYS HFSS.

The modelling of the two probes are as shown in Fig. 5-3 and 5-4. Since these models are axisymmetric, we only simulated the right half of the probes and insured the symmetry with a perfect electric symmetry boundary in the middle. The other boundaries were set to be absorbing boundary to simulate the infinite space. In the simulation of both types of probes, the gold films were modeled as hollow pyramids which corresponded to the shapes of their tips. The height of pyramid was 10 μm and the length of the top side was 5 μm. In order to simulate the actually finite area of the apex of the tip, the pyramid was modeled as a frustum and the length of the base side was set to be 50 nm. The thickness of the gold film, according to the fabrication of the probes, was also set to be 50 nm. The cross section view of x-z plane of the two tips are shown in Fig. 5-5. Here the origin of the coordinate is located at the center of the base of the frustum pyramid. For the slit probe, the pyramid was divided into two parts with a 50 nm wide slit in the middle. The two sides of the tip serve as the two electrodes of the wave guide. For the coaxial probe, in the center of the base a 50 nm × 50 nm square aperture was modeled. Moreover, another gold frustum was modeled inside the hollow pyramid probe. The length of the top side and base side were set to be 4 μm and

10 nm, respectively. The two frustums serve as the inner conductor and outer conductor of the coaxial probe. For both simulations, the whole model was included in a 10 μm × 10 μm × 12 μm vacuum cuboid and the boundary of environment were set as radiation boundary. When the electrical field distribution in the presence of a sample was investigated, the sample was modeled as a plane material as wide as the radiation boundary with a uniform permittivity. Fig. 5-6 shows the meshing of the simulations. Although the meshes were generated automatically by ANSYS HFSS preprocessor software package, since we were only interested in the near-field area near the tip and the interface, the sample and air area were separately modeled near the interface to obtain more detailed and accurate simulation results. For both types of probe, the size of mesh were limited within 0.1 μm and 0.2 μm in area B, C and area A, D, respectively, as shown in Fig. 5-5 and 5-6. In the simulation with sample, the boundary between B and C would be the interface between air and sample. Wave port signal was applied from the top base of the hollow pyramid and the frequency and power were 94 GHz and 0.1 mW (-10 dBm), respectively, corresponding to the microwave signal transmitted into the tip from the cantilever of the probe. Here, it should be pointed out that the exact magnitude of the input signal power is meaningless because the loss of signal within the practical wave guide and M-AFM probe cantilever can hardly be evaluated. Therefore, experimentally the power of microwave have to be calibrated with known materials, which means in the simulation results as long as the relative values of electrical field are enough to investigate the near field distribution of microwave.

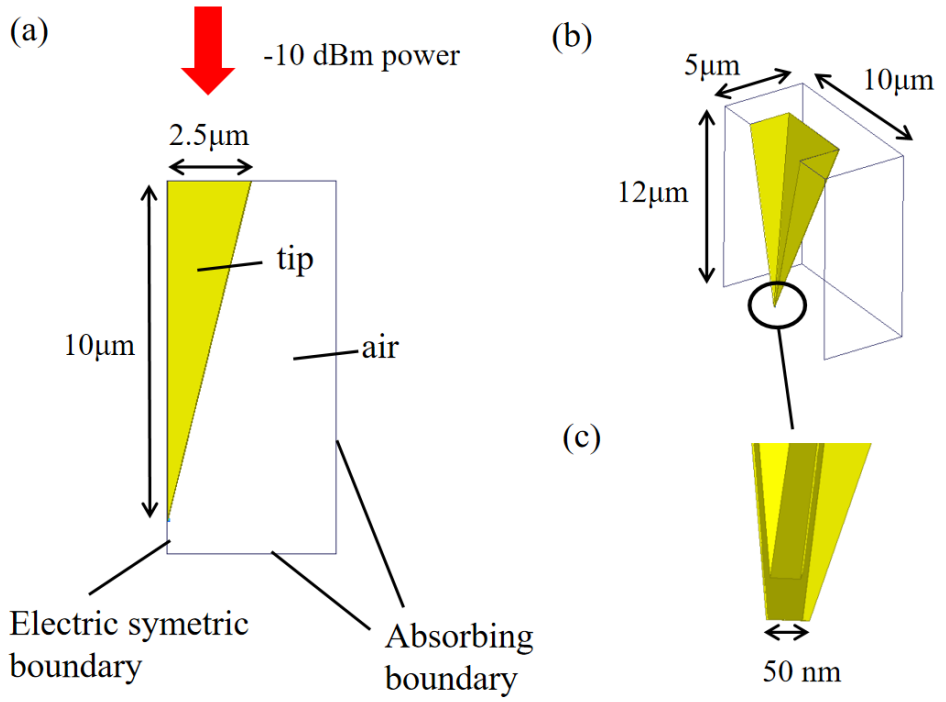

Figure 5-3: The modeling of the slit probe: (a) the side view of the tip model; (b) the 3D view of the tip model; (c) the enlarged view of the end of the tip model.

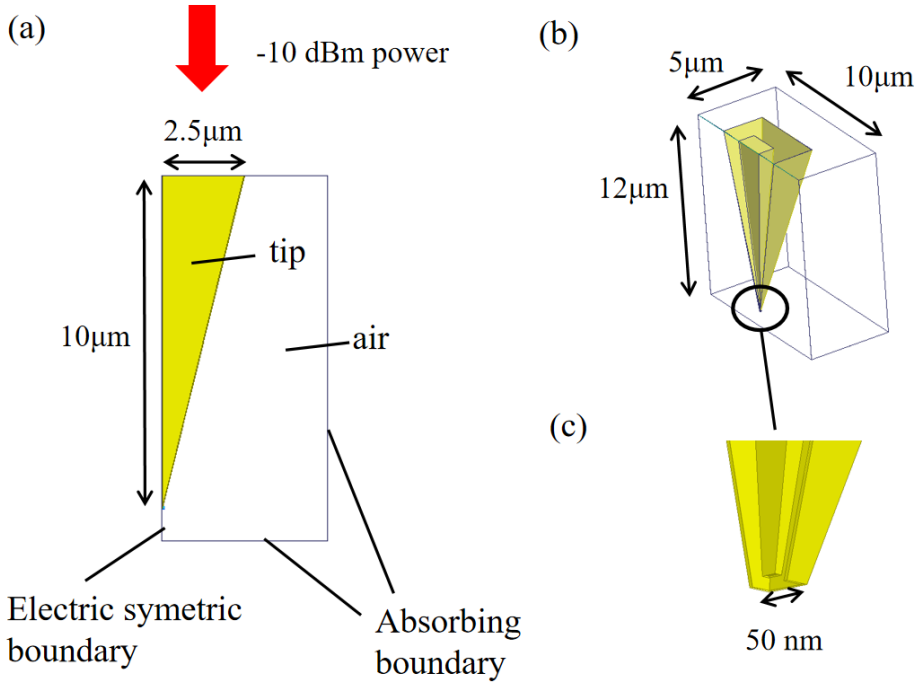

Figure 5-4: The modeling of the coaxial probe: (a) the side view of the tip model; (b) the 3D view of the tip model; (c) the enlarged view of the end of the tip model.

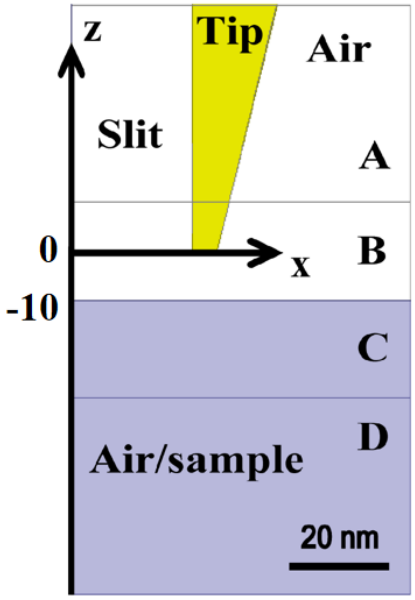

Figure 5-5: The coordinate and space division of the modeling.

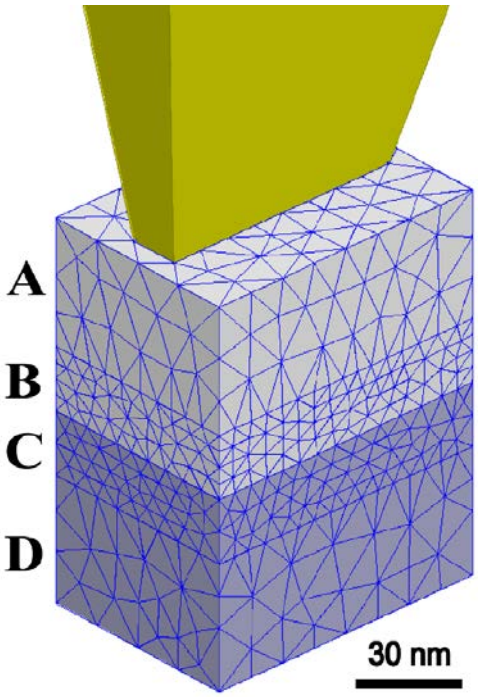

Figure 5-6: The mesh of the modeling.

5.3 Electric Field Distribution in Absence of a Sample

5.3.1 Simulation Results of Slit Probe

First, the near-field microwave distribution without a sample for the silt probe was investigated. The simulation result on $y = 0$ plane is shown in Fig. 5-7. As explained in Chapter 2, in near-field range which is far smaller than the wavelength, phase difference can be omitted. Therefore, we are only interested in the amplitude, and the simulation result here and all the following results in this thesis are the peak values of the electric field. From this result, it can be observed that within the range of the silt the strongest electric field appears at the inner side of the tip and the weakest appears at the central of the slit. This is not consistent with the plane wave model which should have a uniform field intensity. Neither dose this result correspond to a sphere wave model which should have a strongest field intensity in the center of the slit. Therefore, the distribution of near-field microwave should be described as field generated by charges on the tip and sample, rather than electromagnetic wave with no divergence.

In near-field model, the electric field of microwave is regarded as the quasi-static field of the charges on the tip at every instant. These charges have the same phase with the microwave. Therefore, we can calculate the spatial distribution of amplitude of this field and compare with the simulation result. Here, the charge on the inner surface and on the base surface are considered. There is almost no charge exist on the outer surface, and this part is omitted. The densities of surface charge on both inner surface and base surface are approximated to be uniform as σ for simplification. We can take the distribution of electrical field on the $y = 0$ plane as an example to compare the calculation result of near-field model with simulation result. According to the symmetry, the component along y direction of electrical field at any point (x_0, z_0) on the $y = 0$ plane is zero. Thus, only the component along x direction and z direction need to be calculated. For the charge on the base surface the electric field along x direction and z

direction are expressed by Coulomb law as

$$E_x^{\text{base}}\left(x_0, z_0\right) = \frac{\sigma}{4\pi\varepsilon_0}\int_{-y_1}^{y_1}\int_{x_1}^{x_2}\frac{x_0 - x}{\left[\left(x_0 - x\right)^2 + y^2 + \left(z_0 - z_1\right)^2\right]^{3/2}}\mathrm{d}x\mathrm{d}y \tag{5-1}$$

and

$$E_z^{\text{base}}\left(x_0, z_0\right) = \frac{\sigma}{4\pi\varepsilon_0}\int_{-y_1}^{y_1}\int_{x_1}^{x_2}\frac{z_0 - z_1}{\left[\left(x_0 - x\right)^2 + y^2 + \left(z_0 - z_1\right)^2\right]^{3/2}}\mathrm{d}x\mathrm{d}y\,, \tag{5-2}$$

respectively. Here x_1, x_2 and y_1 are the coordinate value of the base surface of the tip as shown in Fig. 5-8. Similarly, for the charge on the inner surface of the tip, the electrical field along x direction and z direction can also be calculated as

$$E_x^{\text{inner}}\left(x_0, z_0\right) = \frac{\sigma}{4\pi\varepsilon_0}\int_{-y_1}^{y_1}\int_{z_1}^{z_1+\Delta z}\frac{x_0 - x_1}{\left[\left(x_0 - x_1\right)^2 + y^2 + \left(z_0 - z\right)^2\right]^{3/2}}\mathrm{d}y\mathrm{d}z \tag{5-3}$$

and

$$E_z^{\text{inner}}\left(x_0, z_0\right) = \frac{\sigma}{4\pi\varepsilon_0}\int_{-y_1}^{y_1}\int_{z_1}^{z_1+\Delta z}\frac{z_0 - z}{\left[\left(x_0 - x_1\right)^2 + y^2 + \left(z_0 - z\right)^2\right]^{3/2}}\mathrm{d}y\mathrm{d}z\,, \tag{5-4}$$

respectively. Here z_1 and Δz are as shown in Fig. 5-8. Δz represents the length of the boundary area of the tip and it can be considered to be the same as the width of the slit. By calculating the electric field generated by the right side and left side of the tip using these formulas and summing them up, the total electric field can be obtained. The calculation results and simulation results of total field along x direction and z direction at $z_0 = -3\ \text{nm}$, $z_0 = -7\ \text{nm}$ and $z_0 = -12\ \text{nm}$ in the coordinate were compared

with each other, which is as shown by the solid lines and dashed lines in Fig. 5-9. Since we mainly aim at the spatial distribution, here the compared field intensity is the relative intensity, in which the field at point ($x_0 = 0$ nm, $z_0 = -3$ nm) is normalized as 1. For both directions, the near field calculation results correspond to the simulation results very well. It demonstrates that the near-field model do provide a precise description for the electric field distribution of slit structured M-AFM probe.

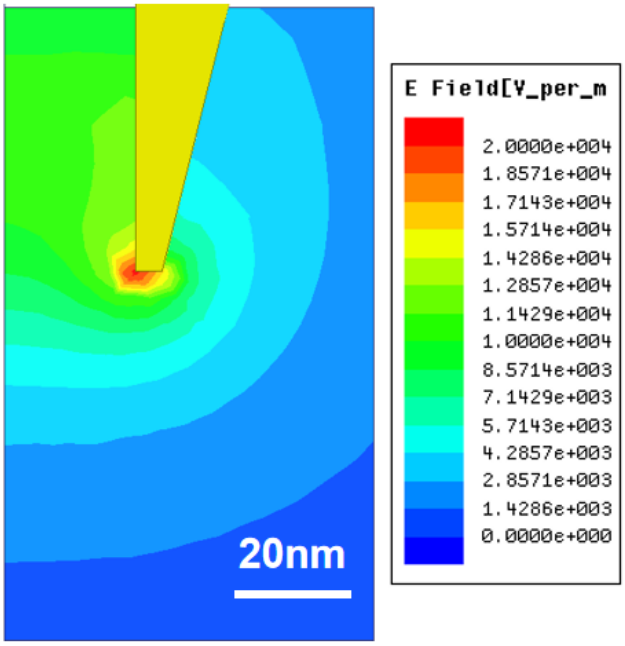

Figure 5-7: The simulation result of electric field distribution on y = 0 plane for slit probe.

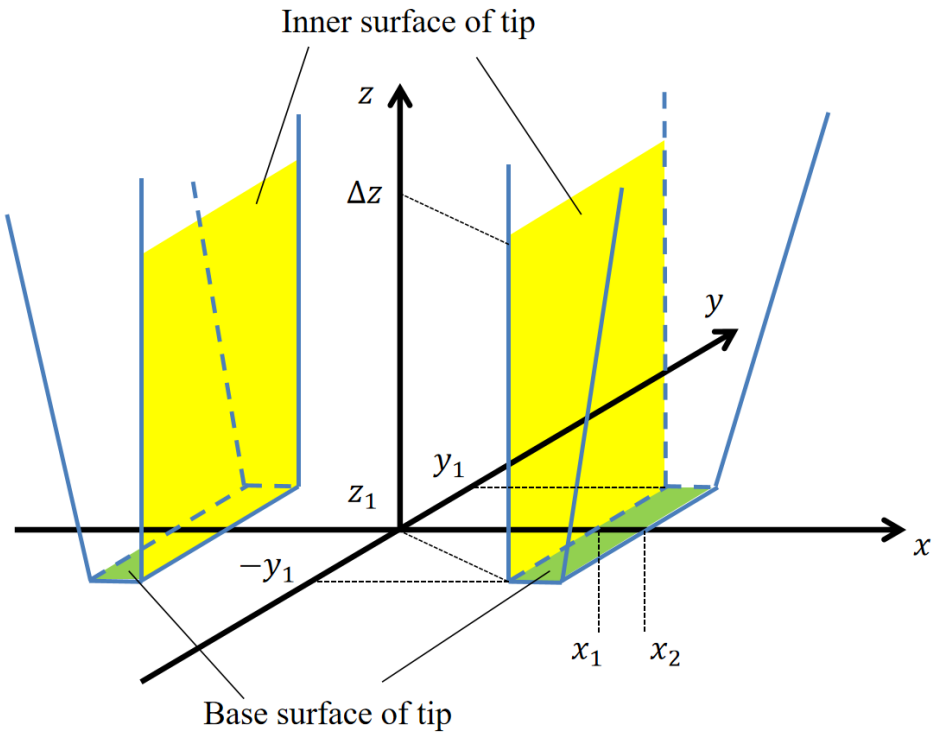

Figure 5-8: The schematic of the structure parameters used for near-field calculation of slit probe.

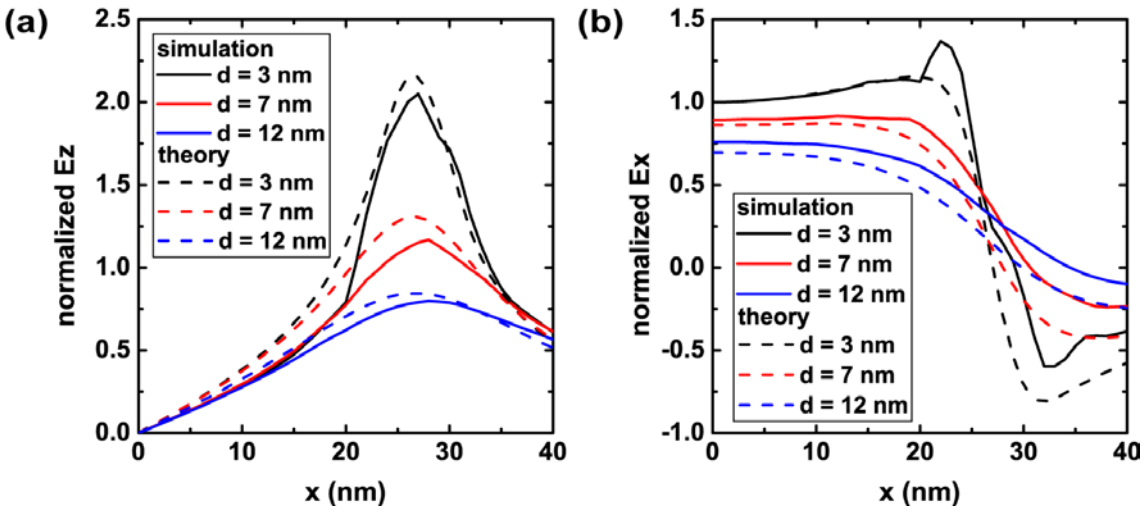

Figure 5-9: The Comparison of distribution of E_z and E_x obtained from EFM simulation and near-field model for slit probe.

5.3.2 Simulation Results of Coaxial Probe

For the coaxial probe, the near-field distribution of microwave without a sample was also simulated. The result on the $y = 0$ plane is as shown in Fig. 5-10. Different from the case of the slit probe, it is found that the strongest electric field appears at the central of the aperture and the weakest appears near the boundary. Another obvious distinction is that although the input power of the microwave for both probes are the same, the output intensity of electrical field emitted from coaxial probe is approximately 100 times higher than that emitted from the slit probe (see Fig. 5-7 and Fig. 5-10). This result provides direct evidence for the previous explanation for the higher sensitivity of coaxial probe. The coaxial probe has a more closed structure that can confine the microwave inside the gold film. The microwave propagating in the coaxial probe is at transverse electromagnetic (TEM) mode which has no cutoff frequency. These factors make the microwave be delivered more easily in the coaxial probe until emitted at the aperture of the tip, which results in a stronger emission power for coaxial probe and consequently lead to a higher measurement sensitivity.

Similarly, the electric field of coaxial probe can also be calculated using the charge at the boundary area of the inner conductor and outer conductor. For the outer conductor, the charge is mainly distributed on the inner surface and the base surface. Since we only discuss the boundary part of the tip, the slight tilt of the inner surface can be neglected. Thus, the inner surface is considered to be composed of two surfaces parallel to x-z plane and other two surfaces parallel to y-z plane. Therefore, the electric field at a certain point (x_0, z_0) of the $y = 0$ plane along x direction and z direction generated by the charge on x-z plane can be calculated as

$$E_x^{\text{x-z}}(x_0, z_0) = \frac{\sigma_1}{4\pi\varepsilon_0} \int_{-x_1}^{x_1} \int_{z_1}^{z_1+\Delta z} \frac{x_0 - x}{\left[(x_0 - x)^2 + y_1^2 + (z_0 - z)^2\right]^{3/2}} \mathrm{d}x\mathrm{d}z \qquad (5\text{-}5)$$

and

$$E_z^{\text{x-z}}(x_0, z_0) = \frac{\sigma_1}{4\pi\varepsilon_0}\int_{-x_1}^{x_1}\int_{z_1}^{z_1+\Delta z}\frac{z_0 - z}{\left[(x_0 - x)^2 + y_1^2 + (z_0 - z)^2\right]^{3/2}}\mathrm{d}x\mathrm{d}z\,, \qquad (5\text{-}6)$$

respectively. The component along y direction is still zero according to the symmetry. For the charge on the y-z plane, the electric field can be calculated as

$$E_x^{y-z}(x_0, z_0) = \frac{\sigma_1}{4\pi\varepsilon_0}\int_{-y_1}^{y_1}\int_{z_1}^{z_1+\Delta z}\frac{x_0 - x_1}{\left[(x_0 - x_1)^2 + y^2 + (z_0 - z)^2\right]^{3/2}}\mathrm{d}y\mathrm{d}z \qquad (5\text{-}7)$$

and

$$E_z^{y-z}(x_0, z_0) = \frac{\sigma_1}{4\pi\varepsilon_0}\int_{-y_1}^{y_1}\int_{z_1}^{z_1+\Delta z}\frac{z_0 - z}{\left[(x_0 - x_1)^2 + y^2 + (z_0 - z)^2\right]^{3/2}}\mathrm{d}y\mathrm{d}z\,, \qquad (5\text{-}8)$$

respectively. The structural parameters x_1, y_1, z_1 and Δz are as shown in Fig 5-11. Δz, the length of the boundary area of the tip, is considered to be the same as the width of the aperture. On the other hand, the base surface of outer surface is composed of two striped areas along y direction and other two striped areas along x direction as shown in Fig 5-11. The electric field on the $y = 0$ plane along x direction and z direction generated by the charge on the two parts can be calculated as

$$E_x^{\text{base-y}}(x_0, z_0) = \frac{\sigma_1}{4\pi\varepsilon_0}\int_{-x_1}^{x_1}\int_{y_1}^{y_2}\frac{x_0 - x}{\left[(x_0 - x)^2 + y^2 + (z_0 - z)^2\right]^{3/2}}\mathrm{d}x\mathrm{d}y\,, \qquad (5\text{-}9)$$

$$E_z^{\text{base-y}}(x_0, z_0) = \frac{\sigma_1}{4\pi\varepsilon_0}\int_{-x_1}^{x_1}\int_{y_1}^{y_2}\frac{z_0 - z}{\left[(x_0 - x)^2 + y^2 + (z_0 - z)^2\right]^{3/2}}\mathrm{d}x\mathrm{d}y\,, \qquad (5\text{-}10)$$

$$E_x^{\text{base-x}}(x_0, z_0) = \frac{\sigma_1}{4\pi\varepsilon_0}\int_{-y_1}^{y_1}\int_{x_1}^{x_2}\frac{x_0 - x}{\left[(x_0 - x)^2 + y^2 + (z_0 - z)^2\right]^{3/2}}\mathrm{d}x\mathrm{d}y \qquad (5\text{-}11)$$

and

$$E_z^{\text{base-x}}(x_0, z_0) = \frac{\sigma_1}{4\pi\varepsilon_0}\int_{-y_1}^{y_1}\int_{x_1}^{x_2}\frac{z_0 - z}{\left[(x_0 - x)^2 + y^2 + (z_0 - z)^2\right]^{3/2}}\mathrm{d}x\mathrm{d}y\,, \qquad (5\text{-}12)$$

respectively. σ_1 is the surface charge density on outer conductor and x_2, y_2 are structural parameter as shown in Fig 5-11. For the inner conductor, the charge is on the outer surface and the base. The electric field on $y = 0$ plane can be calculated using equations similar to Eqs. (5-5) - (5-8). Only one thing should be pointed out that the area of inner surface of outer conductor is 5 times larger than the surface of inner conductor. Therefore, according to the law of the conservation of the charge, the surface charge density on the surface of inner conductor, which is represented as σ_2, should be $5\sigma_1$. Finally, by summarizing the electric field of all the surface charges on the tip, the total electric field at $z = -3\,\text{nm}$, $z = -7\,\text{nm}$ and $z = -12\,\text{nm}$ were obtained and compared with the simulation result. The results were normalized in the same way as implemented for the slit probe, which is as shown in Fig. 5-12. It is also demonstrated for the coaxial probe that the near-field model can provide a relatively accurate quantitative description for the electric field distribution of microwave.

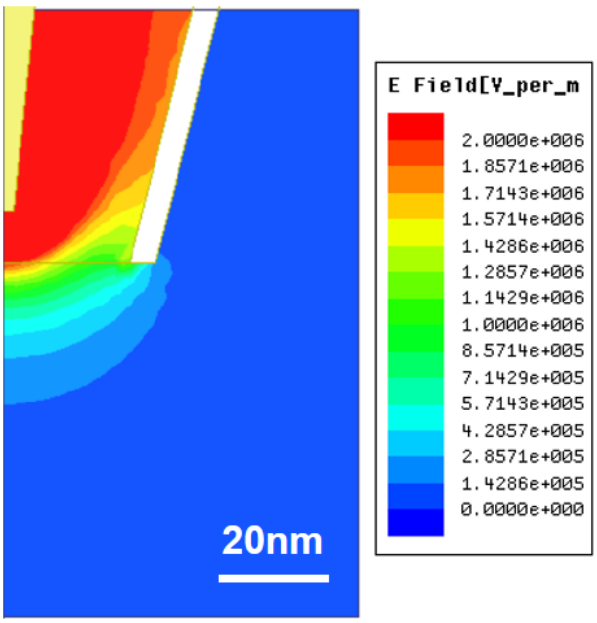

Figure 5-10: The simulation result of electric field distribution on y = 0 plane for coaxial probe.

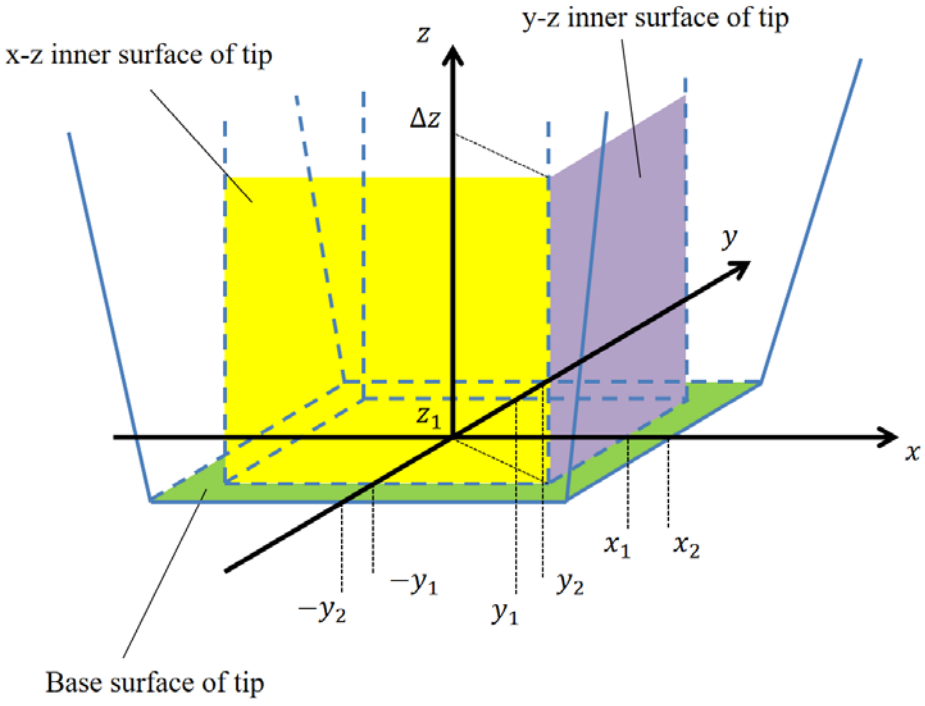

Figure 5-11: The schematic of the structure parameters used for near-field calculation of coaxial probe. To keep the legibility of the figure, only the x-z inner surface and y-z inner surface near us were marked, and the inner conductor was hided.

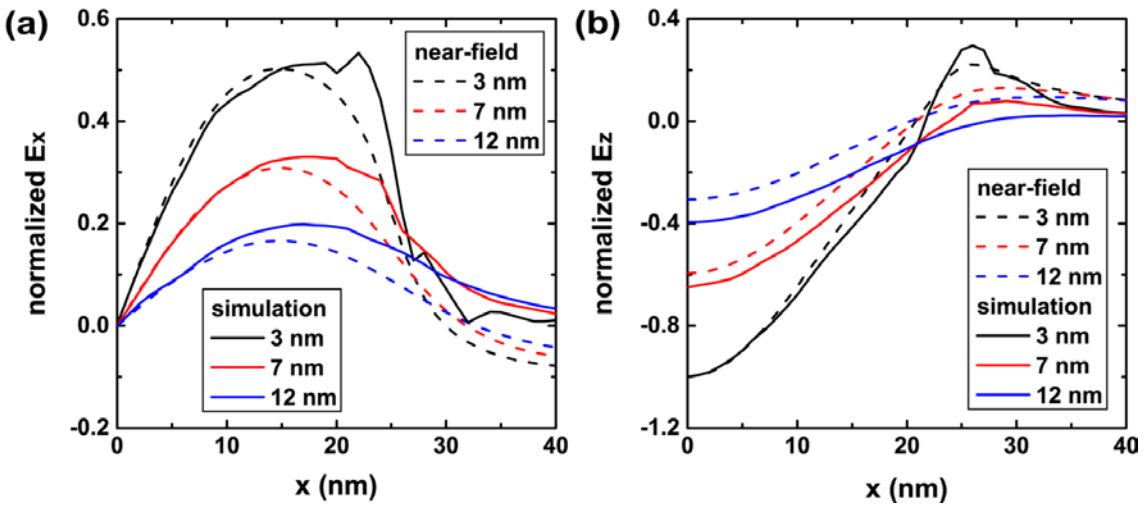

Figure 5-12: The Comparison of distribution of Ez and Ex obtained from EFM simulation and near-field model for coaxial probe.

5.4 Discussion for Microwave Emission Capability and Resolution

5.4.1 Size of Aperture

For both types of probe, the size of the slit or the aperture (we name it 'aperture' for both probes in the rest of this chapter) is a key parameter in relation with the capability of microwave emission. In order to determine the optimal size of the aperture, the electric field distribution of slit probe with 50 nm, 80 nm and 120 nm slit were simulated. For the coaxial probe, the simulation results with 50 nm×50 nm, 80 nm×80 nm and 120 nm×120 nm aperture were also obtained. For all simulations, the input power of microwave was 0.1 mW. As shown in Fig. 5-13 and Fig. 5-14, it is noted that for both slit probe and coaxial probe, the intensity of strongest electric field region is almost constant. It means that the reflected microwave caused by the emitted microwave is also the same, which in addition means that the sensitivity is almost

independent from the aperture size.

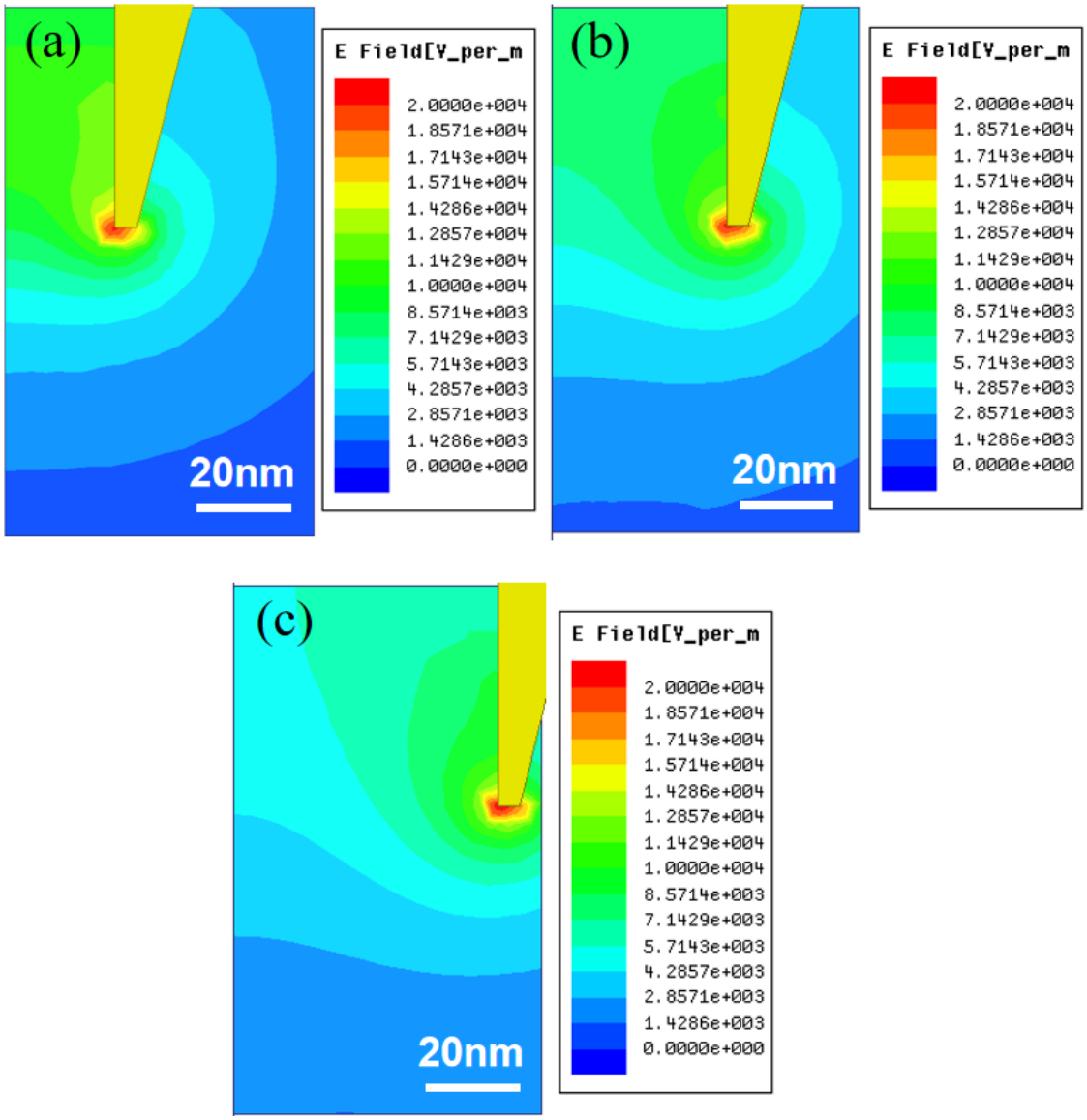

Figure 5-13: The simulation results of slit probe with different aperture size: (a) 50 nm; (b) 80 nm; (c) 120 nm.

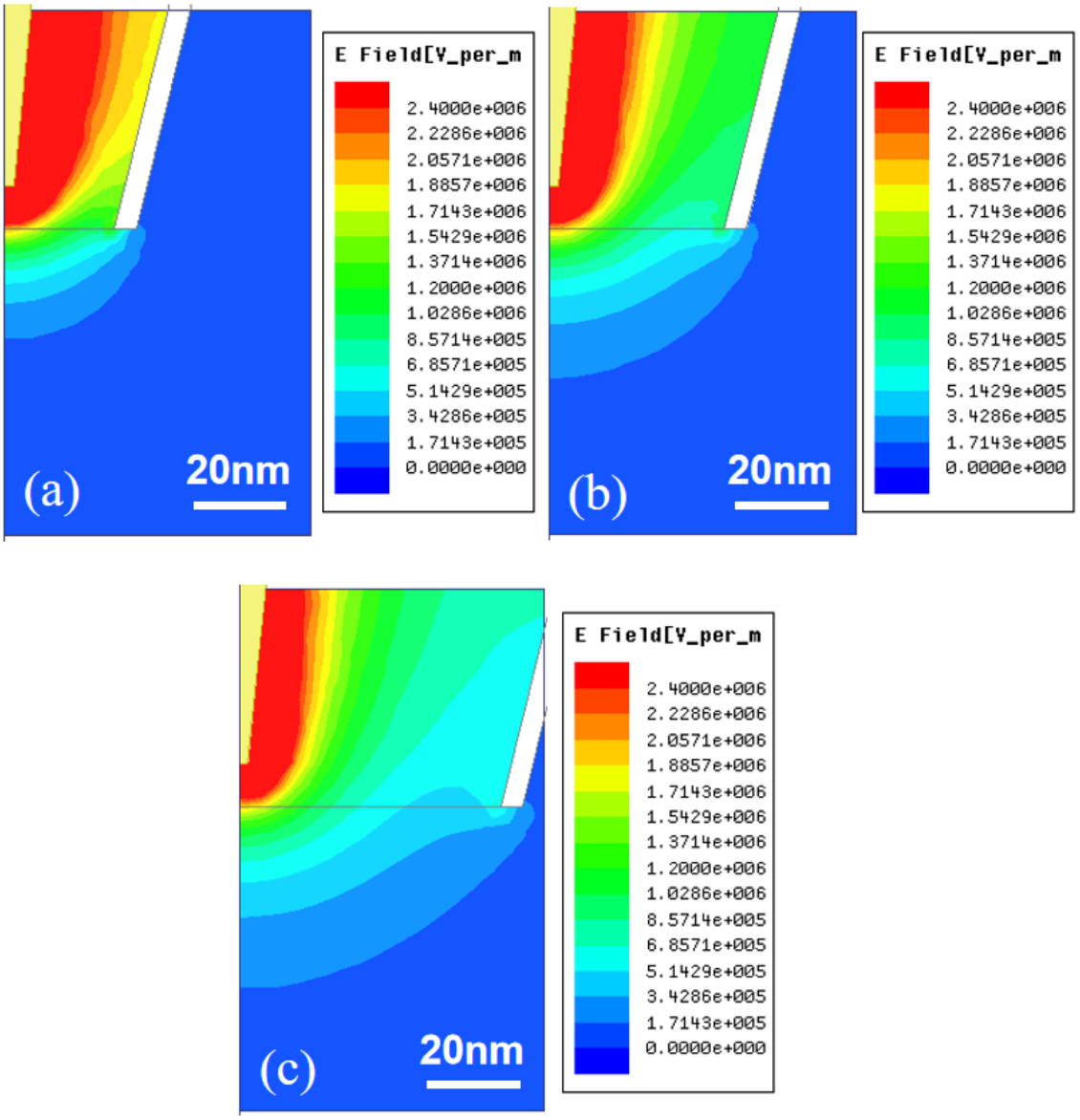

Figure 5-14: The simulation results of coaxial probe with different aperture size: (a) 50 nm; (b) 80 nm; (c) 120 nm.

On the other hand, the range of the electric field region is related with the microwave resolution of the probe. To quantify the resolution for discussion, an effective interaction region of the electric field need to be defined. The region near the point with strongest field intensity is considered to dominate the electromagnetic interaction between the tip and sample. Therefore, the effective interaction region of the electric

field can be defined as the region where the field intensity is more than half of the strongest intensity. The range of the effective interaction is defined as the microwave resolution. Using this definition, the resolution of the two probes were evaluated from simulation result, as marked in Fig. 5-15 and Fig. 5-16. For slit probe, the strongest field region moves with the increasing aperture and the highest resolution is the case that the slit is the smallest. For the case of coaxial probe, however, the strongest electric field region remains the same with the inner conductor, which means the resolution is not affected by the aperture size. This is an unusual result which is not consistent with most other scanning probe microscopies. The reason relies on the coaxial structure. The aperture size, which is the outer conductor only affects the weak boundary part of the field which almost does not change the resolution. However, since the strongest region stays with the inner conductor, as will be shown in the next section, the size of inner conductor affects the resolution obviously. In experiment, the fabrication limit of our FIB etching is 50 nm. Therefore, the upper limit of theoretical microwave resolution of slit probe is evaluated to be 70 nm. As a basis for the fabrication of M-AFM probes, the slit probe requires an aperture as small as possible for high resolution, while the coaxial probe is not affected.

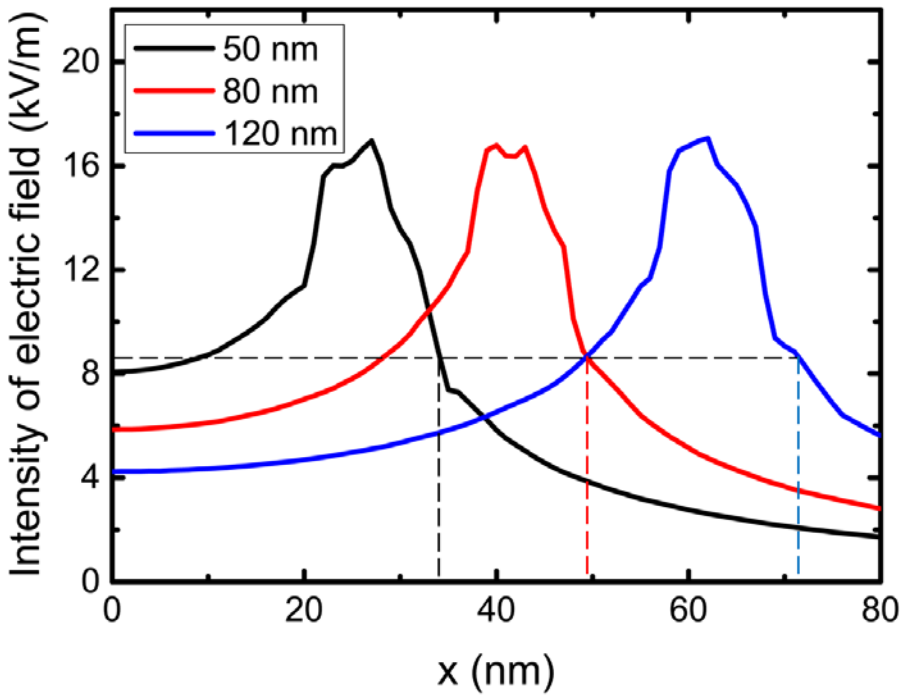

Figure 5-15: The Comparison of simulation results of field distribution at z = -3 nm for slit probe with different aperture size.

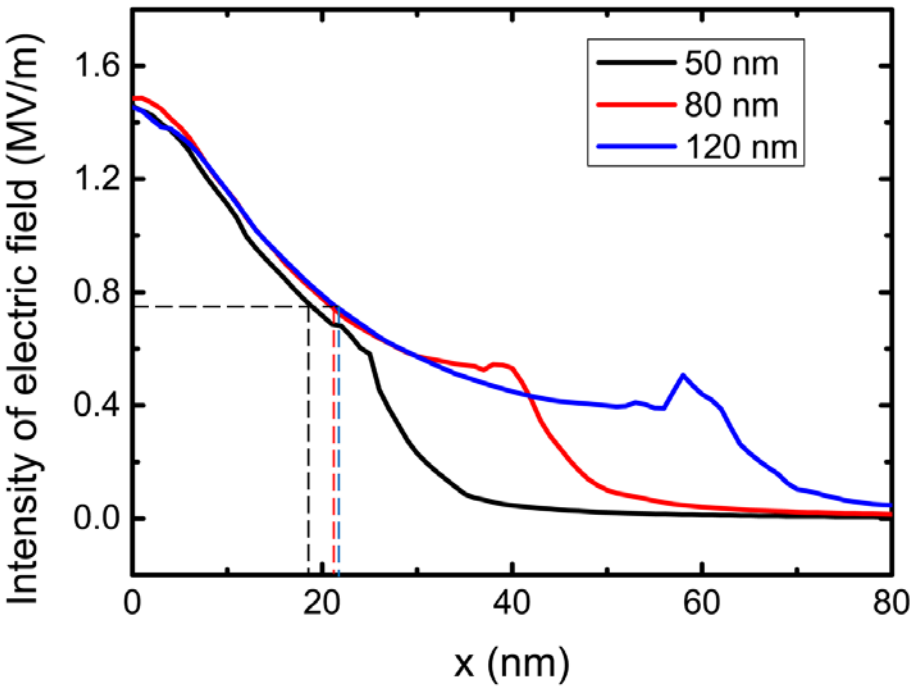

Figure 5-16: The Comparison of simulation results of field distribution at z = -3 nm for coaxial probe with different aperture size.

5.4.2 Thickness of Inner Conductor of Coaxial Probe

Since the sensitivity and resolution of the coaxial probe is almost independent from the outer conductor, we further investigated its field distribution with different inner conductors. Fig. 5-17 shows the simulation results of three coaxial probes, in which the thicknesses of the inner conductor are 5 nm, 10 nm and 20 nm, respectively. It is observed that on one hand the intensity of the electric field increases with the increasing thickness of the inner conductor, and on the other hand, the region that the electric field intensity is relatively strong also becomes wider. As mentioned in the above paragraph, the electric field region, which is described by effective interaction region, is related with the microwave resolution of the probe. Using this definition, the simulated electric field distributions under different inner conductor thickness in Fig. 5-17 were extracted and the resolutions were marked as shown in Fig. 5-18. It is confirmed that although the electric field intensity of emitted microwave which represents the sensitivity increases with increasing thickness, the resolution decreases slightly. Considering that the emitted electric field intensity of coaxial probe is much stronger than that of the slit probe, the resolution of coaxial probe is expected in priority. Therefore, the optimal thickness of inner conductor of a coaxial probe should be as small as possible.

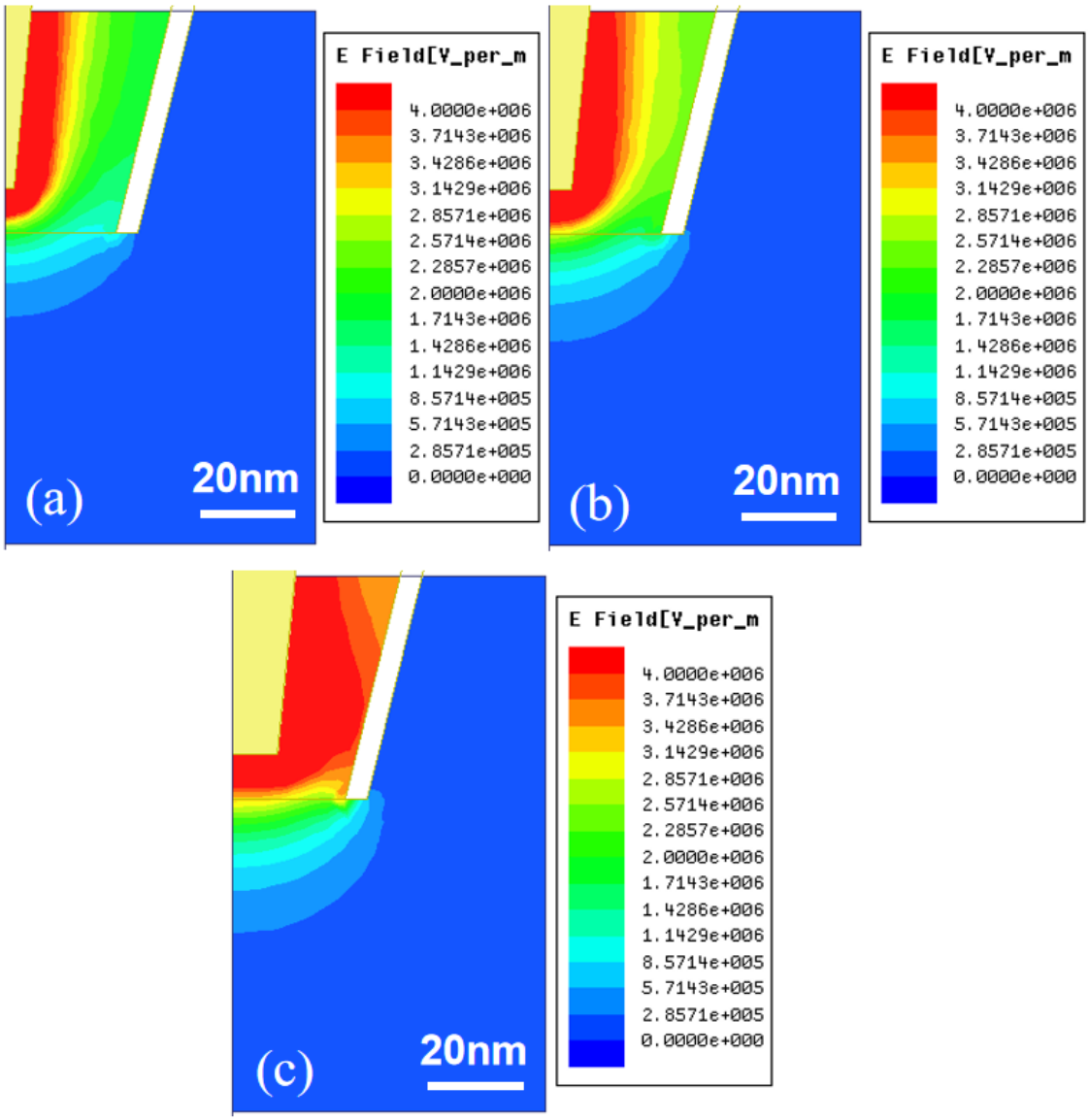

Figure 5-17: The simulation results of coaxial probe with different inner conductor thickness: (a) 5 nm; (b) 10 nm; (c) 20 nm.

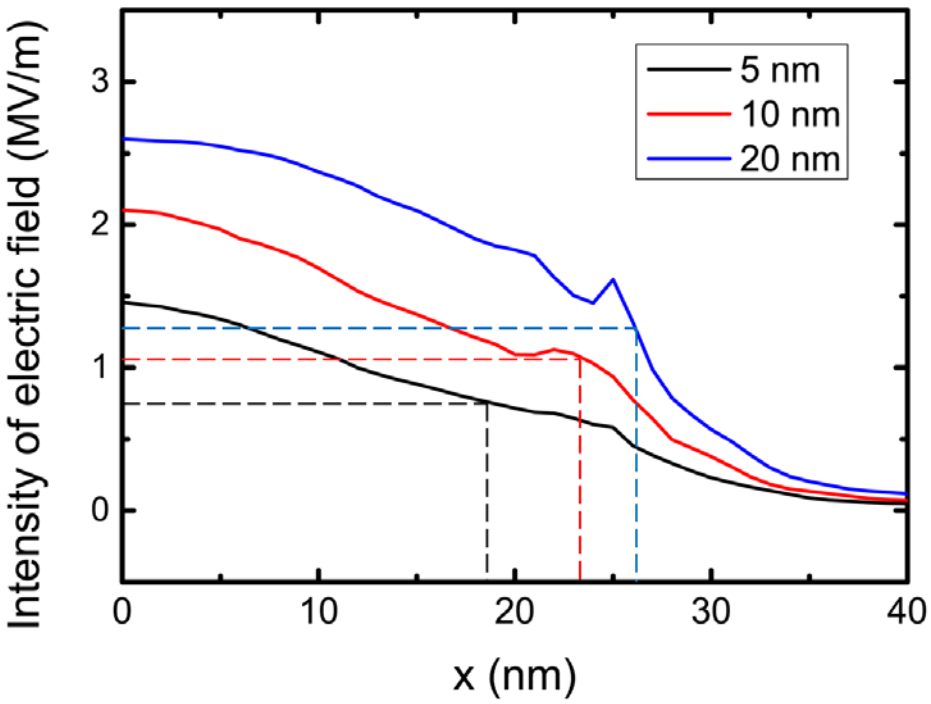

Figure 5-18: The Comparison of simulation results of field distribution at z = -3 nm for coaxial probe with different inner conductor thickness.

5.4.3 Length of Inner Conductor of Coaxial Probe

Besides the thickness of the inner conductor, the length of the inner conductor also impacts the electric field distribution. It can be noted that in the above simulations for coaxial probe, the inner conductor was modeled 10 nm shorter than the outer conductor. Referring to the reason, on one hand, in fabrication the inner conductor is almost impossible to be the same as or longer than the outer conductor because of the fabrication method. On the other hand, actually the length of the inner conductor strongly impacts the emitted microwave, and as can be demonstrated in the following section, equal length of inner and outer conductor may not be the optimal structure. The electric field distribution of microwave under the condition that the length difference between inner and outer conductor is 0 nm, 50 nm, and 100 nm were simulated and the

results are shown in Fig 5-19. In the case that the inner conductor is as long as the outer conductor, the distribution of the emitted microwave has two strongest points on the corner of the inner conductor. In the cases that the length difference is 10 nm and longer, the distribution has only one strongest point right in the center of the probe. Usually we prefer a distribution that the strongest point is in the center, because the part of sample right under the tip corresponds to the location of the tip, and for an uneven material it would be measured directly. If the distribution has several strongest points, the evaluated value would be the average value of these area, and the resolution would not be better. Referring to the emission power, it can be observed that with the increasing length difference between the inner and outer conductor, the emission power decreases. As shown in Fig. 5-19(c), when the difference comes to 100 nm, the emission power becomes weaker than that of the slit probe. As a conclusion, the optimal range of length difference should be controlled from 10 nm to 100 nm.

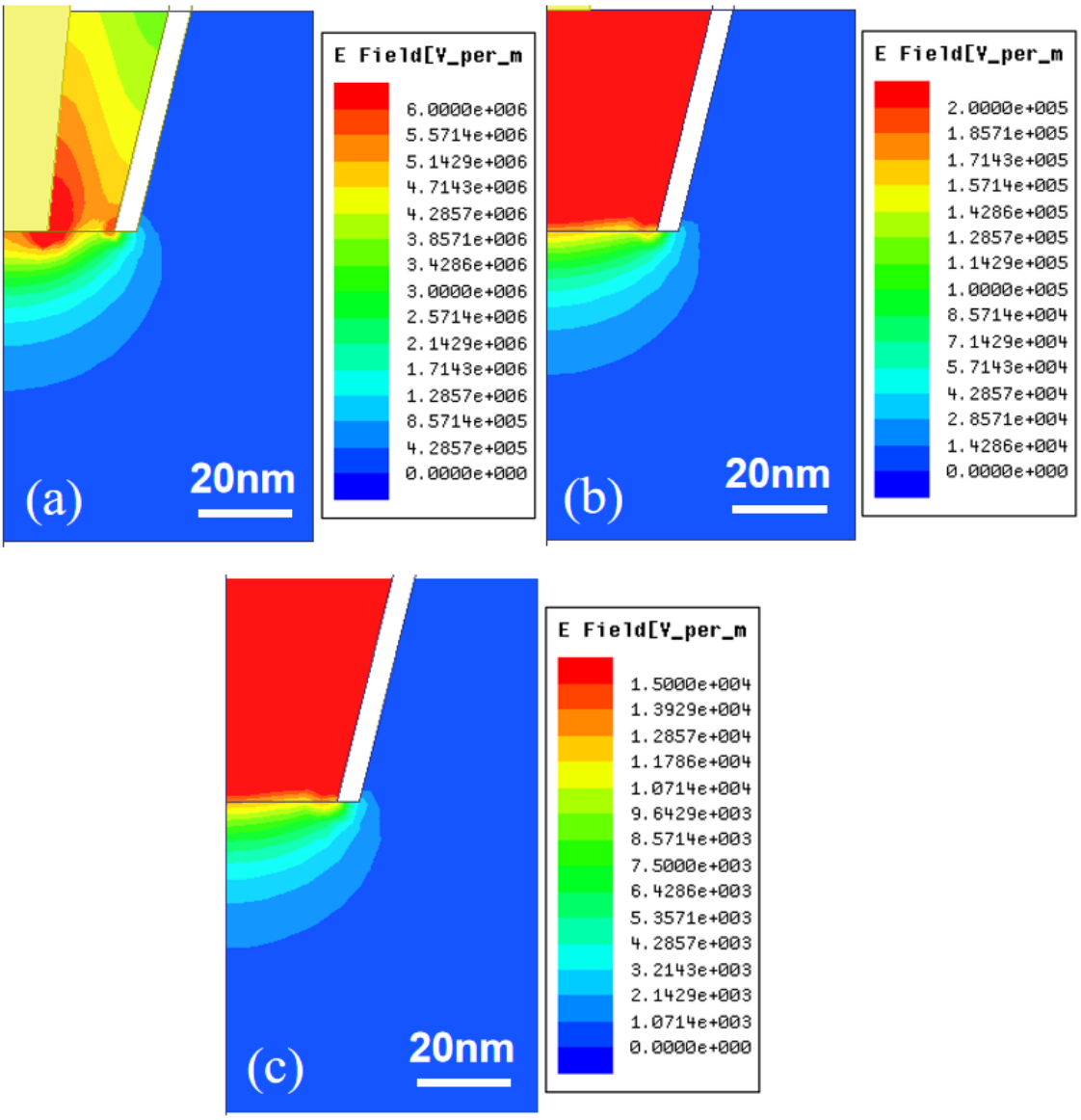

Figure 5-19: The simulation results of coaxial probe with different length difference between inner and outer conductor: (a) 0 nm; (b) 50 nm; (c) 100 nm.

5.4.4 Comparison between Slit Probe and Coaxial Probe

Based on the present information, the advantages of the two types of probes can be discussed. First, about the emission intensity of the microwave, with the same input power and the same size of aperture, the coaxial probe can be 100 times stronger than the slit probe because of the closed structure and TEM mode. Higher emission power results in more obvious response to different sample, which means the coaxial probe has a better sensitivity. This conclusion supports the experimental results of our previous research [3]. Second, since the slit probe has two strongest electric field points, the coaxial probe also has a better resolution than the slit probe. On the other hand, an advantage of slit probe is that the fabrication is much easier and more controllable than coaxial probe. For the coaxial probe, the length difference between inner and outer conductor is strictly limited in order to emit microwave. The alignment of the aperture, inner conductor and outer conductor is also difficult, which makes the yield very low. Another advantage for slit probe is that the theoretical model is simpler for calculation and less easily affected by the irregular caused by fabrication.

5.5 Electric Field Distribution with Dielectric Samples and Sample Permittivity Dependence

5.5.1 Different Sample Property Dependence between Near Field Model and Plane Wave Model

As mentioned in Section 4.1, the difference between plane wave model and near-field model is not only the spatial distribution, but also the sample electrical property dependence of reflected and transmitted microwave. The origin of the difference comes from the fact that, in plane wave mode the electric field is an alternating field excited by

magnetic field, while in near-field model the electric field is considered as an quasi-static field generated by charge and magnetic field is not considered. For metallic materials, the conductivity describes how easy it is for free charge to move. However, in near-field model the quasi-static field means the movement of charge is neglected and all metals instantly reach the same equilibrium state. Therefore, sample conductivity does not exist in near-field model because the approximation is too strict. We can only introduce the conductivity dependence of plane wave model to the near field model to build a semi-near-field model.

On the other hand, for dielectric materials, the permittivity describes the degree of polarization of bonded charge. Although both models include the permittivity of sample, different views of origin of electric field result in different permittivity dependence. According to the conclusion of electromagnetism, if a point charge q is placed over an infinite wide plane dielectric material and the electric field caused by q at a certain point inside the material is E_0, the resultant electrical field E_1 which is caused by q and its polarization charge at the same point inside the material can be represented as [4]

$$E_1 = \frac{2}{\varepsilon_r + 1} E_0, \tag{5-13}$$

where ε_r is the permittivity of the dielectric material. As explained in Section 4.2.1, E_0 and E_1 in Eq. 5-13 can be regarded as the incident wave and the transmitted wave in near-field model. Referring to the plane wave model, according to the conclusion of electrodynamics, when electromagnetic wave is vertically reflected by an infinite wide plane dielectric material, the relationship between transmitted wave E_1 and incident wave E_0 is given by [5]

$$E_1 = \frac{2}{\sqrt{\varepsilon_r} + 1} E_0, \tag{5-14}$$

In order to confirm whether the near-field model provides a more accurate permittivity dependence than the plane wave model as well, the electric field distribution with dielectric materials of a slit probe were investigated by simulation.

5.5.2 Results of Electric Field Distribution with Dielectric Sample

The electric field distribution with dielectric samples of different permittivity (ε_r =5, 10, 15, 20, 25, 30, 35) were simulated. Fig. 5-20 shows the results of ε_r =5, 15, 25 on the $y = 0$ plane. The distribution inside and outside the sample were shown with different color bar, respectively. In these simulations, the sample surface was located at $z = -10$ nm. In addition, the ratio of transmitted wave and incident wave E_1/E_0 at different ε_r were extracted and shown in Fig. 5-21. Here E_1 is the value of field at $z = -15$ nm of the simulations with samples of different permittivity, while E_0 is the value of field at $z = -15$ nm of simulation without sample ($\varepsilon_r = 1$). These points are fitted with the following equation:

$$E_1 = \frac{2}{\varepsilon_r^{\alpha} + 1} E_0 . \tag{5-15}$$

The fitting result, as shown by the red line in Fig. 5-21, turns out to be $\alpha = 0.848$. Although the result seems to be closer to the conclusion of near field model than the plane wave model, the deviation is still too obvious to be ignored. Comparing the distribution results shown in Fig. 5-20 and Fig. 5-7, it is noted that the strongest regions (red region) of these simulations move from the inner corner of the tip to the middle of the base surface. The value of the strongest intensity also increases with increasing sample permittivity. This implies that in the simulation results the emitted microwaves in the presence of different samples may not be exactly the same although the input powers were constant. Therefore, the E_0 in Eq. 5-15 also depends on ε_r.

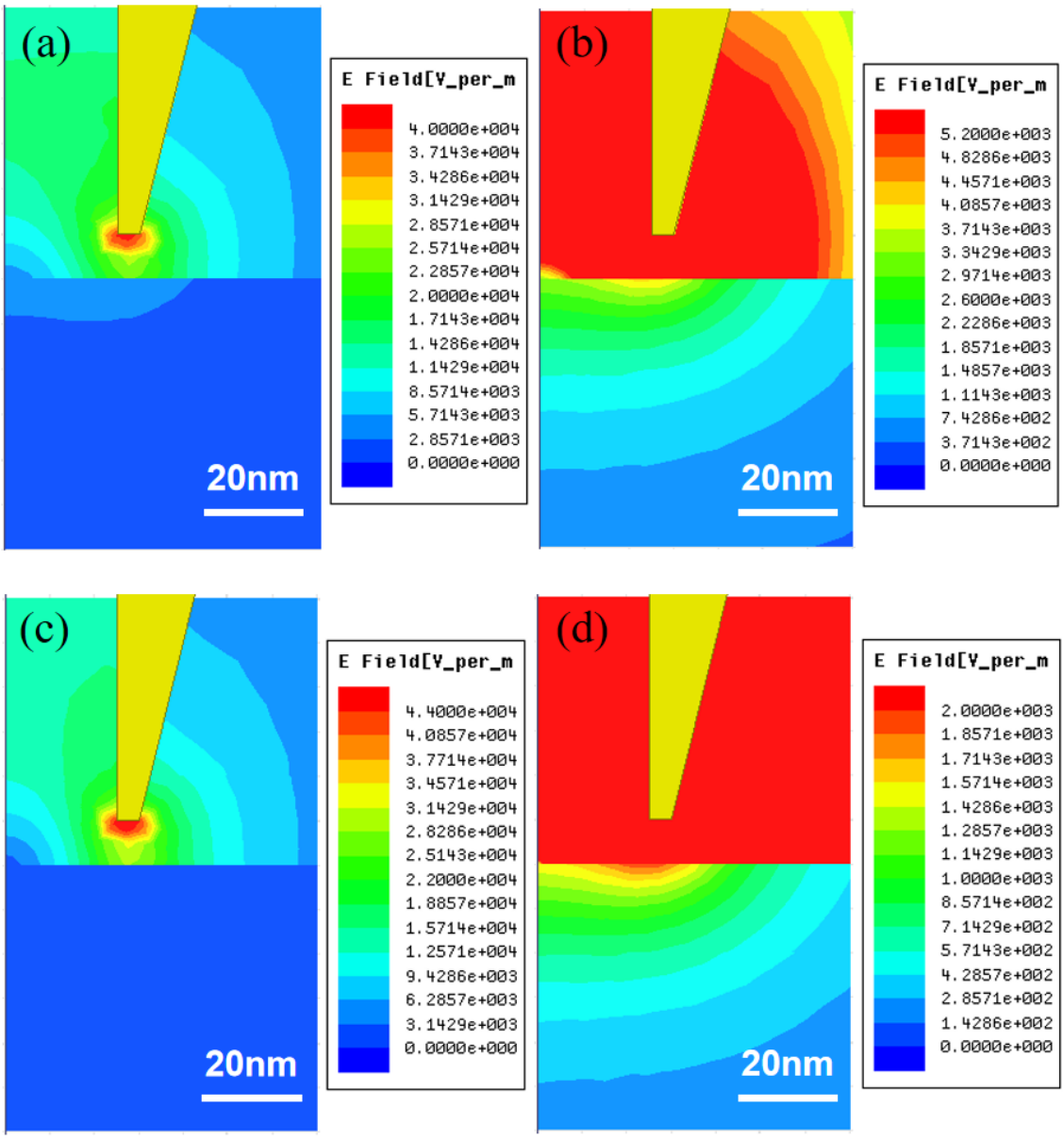
(a)
E Field[V_per_m
4.0000e+004
3.7143e+004
3.4286e+004
3.1429e+004
2.8571e+004
2.5714e+004
2.2857e+004
2.0000e+004
1.7143e+004
1.4286e+004
1.1429e+004
8.5714e+003
5.7143e+003
2.8571e+003
0.0000e+000
20nm
(b)
E Field[V_per_m
5.2000e+003
4.8286e+003
4.4571e+003
4.0857e+003
3.7143e+003
3.3429e+003
2.9714e+003
2.6000e+003
2.2286e+003
1.8571e+003
1.4857e+003
1.1143e+003
7.4286e+002
3.7143e+002
0.0000e+000
20nm
(c)
E Field[V_per_m
4.4000e+004
4.0857e+004
3.7714e+004
3.4571e+004
3.1429e+004
2.8286e+004
2.5143e+004
2.2000e+004
1.8857e+004
1.5714e+004
1.2571e+004
9.4286e+003
6.2857e+003
3.1429e+003
0.0000e+000
20nm
(d)
E Field[V_per_m
2.0000e+003
1.8571e+003
1.7143e+003
1.5714e+003
1.4286e+003
1.2857e+003
1.1429e+003
1.0000e+003
8.5714e+002
7.1429e+002
5.7143e+002
4.2857e+002
2.8571e+002
1.4286e+002
0.0000e+000
20nm

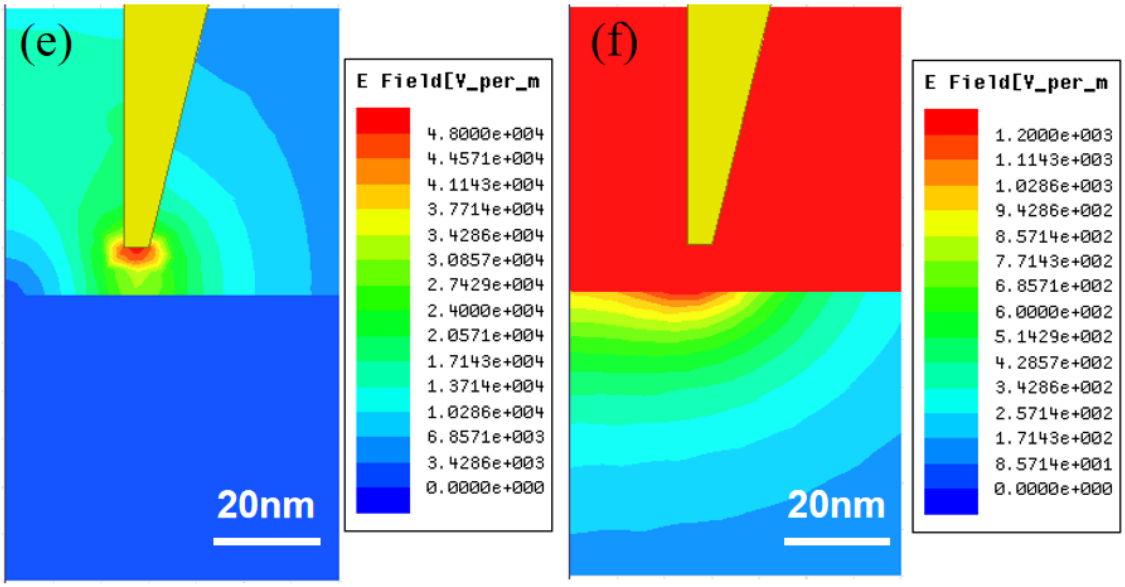

Figure 5-20: The simulation results of slit probe with different sample permittivity: (a), (b) $\varepsilon_r = 5$; (c), (d) $\varepsilon_r = 15$; (e), (f) $\varepsilon_r = 25$. The figures on the left and right are the same result with different color bar.

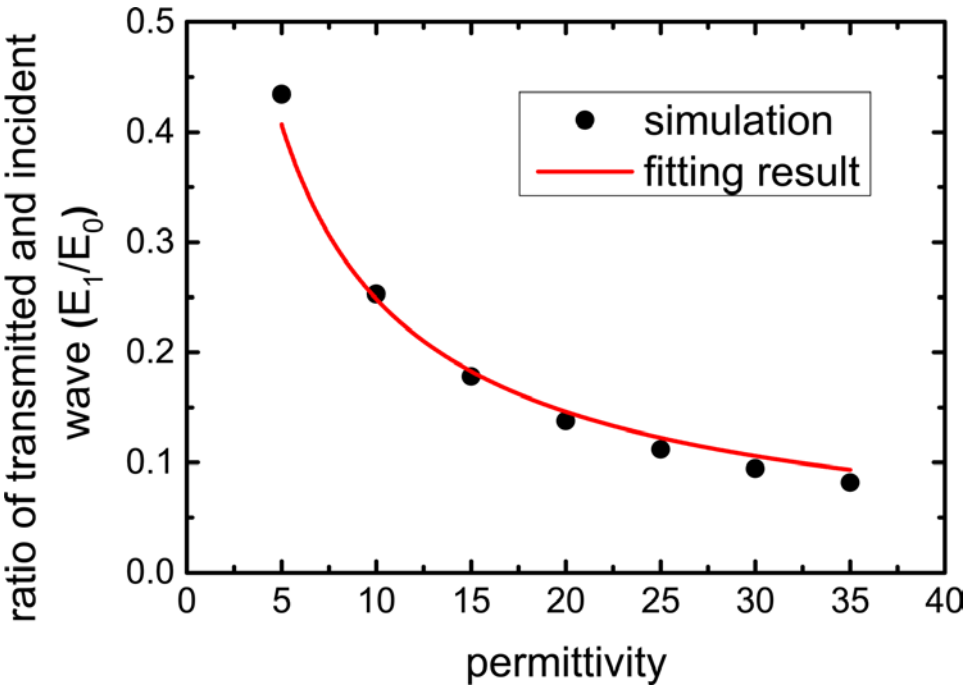

Figure 5-21: The simulation result of ratio of transmitted wave and incident wave depending on the sample permittivity.

As mentioned above, the polarization charge only exists on the surface of the sample ($z = -10$ nm), which means the electric field caused by the polarization charge is symmetric on the two sides of the sample-air interface (See Fig. 5-22 (b)). Therefore, we can eliminate the field of polarization charge and extract the incident wave along x and z direction by $E_x(z = -5\text{ nm}) - E_x(z = -15\text{ nm})$ and $E_z(z = -5\text{ nm}) + E_z(z = -15\text{ nm})$ for each simulation result. The normalized electric field distributions of each simulation processed by the formulas above are shown in Fig. 5-23. The violet dashed lines represent the theoretical calculation results of near-field model. They correspond to the simulation results when $\varepsilon_r = 1$, under which condition there is no polarization charge. With the sample permittivity increasing, the deviation from the $\varepsilon_r = 1$line becomes larger and larger, which demonstrates that the incident wave is gradually enhanced. Based on the near-field model, the reason of this enhancement phenomena can be understood as the reaction of polarization charge to the original charge on the tip. The sample with higher permittivity induces stronger polarization charge and stronger polarization charge also attracts the charge on the tip more heavily. Therefore, more charge accumulates at the boundary area of the tip and thus stronger incident wave is generated. The tip-sample electrical interaction is the basis for the evaluation of permittivity of materials, which was applied in the study of Chapter 2. It also corresponds to the experimental result that the microwave with 10 dBm source power has a lower attenuation than that with 5 dBm source power [6].

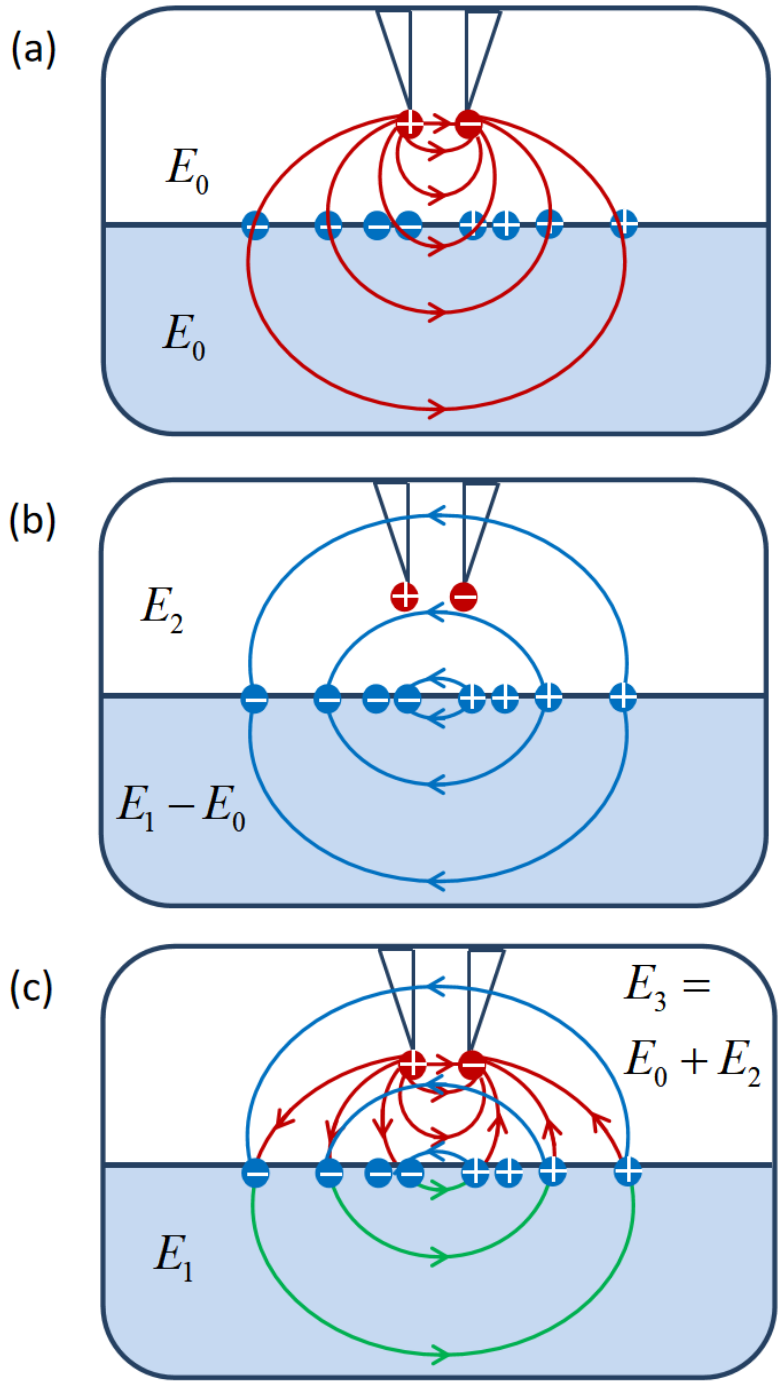

Figure 5-22: The schematics of field generated by original charge and polarization charge: (a) field of original charge, E_0 is equivalent to incident wave; (b) field of polarization charge, E_2 is equivalent to reflected wave and E_2 and E_1 - E_0 are symmetrical; (c) resultant field, E_1 is equivalent to transmitted wave.

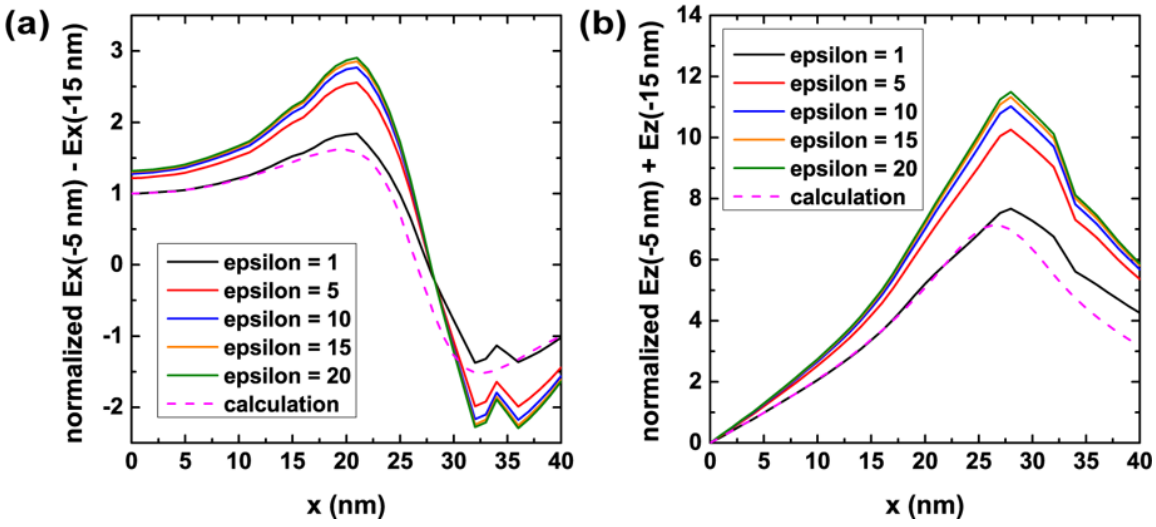

Figure 5-23: The results of electrical field distribution along x and z direction after eliminating the field of polarization charge.

Quantitatively, the average enhancement coefficients β from x = 0 to x = 40 nm of the simulations at each ε_r can be calculated from Fig. 5-23. Taking the enhancement effect into consideration, $E_1(\mathrm{z} = -15\ \mathrm{nm})/\beta E_0(\mathrm{z} = -15\ \mathrm{nm})$ is compared with the theoretical ratio of near-field model, i.e., $2/(\varepsilon_r + 1)$, which is shown in Fig. 5-24(a). It is demonstrated that permittivity dependence of the transmitted wave can be accurately described by the near-field model. Similarly, we can investigate the permittivity dependence of reflected wave. In the near-field model, the reflected wave E_2 is the electric field above the sample-air interface generated by the polarization charge. On the other hand, as explained above, transmitted wave E_1 is the resultant electric field inside the sample generated by the polarization charge and original charge (See Fig 5-22 (b), (c)). Therefore, according to the symmetry of the polarization field, E_2 at $z = -5\ \mathrm{nm}$ should be the same as $E_1 - \beta E_0$ at $z = -15\ \mathrm{nm}$. E_2 at $z = -5\ \mathrm{nm}$ can be obtained by $E_3 - \beta E_0$ at $z = -5\ \mathrm{nm}$, where E_3 is the values of resultant field of the simulations with samples of different permittivity (See Fig 5-22 (c)). The comparison of $E_3 - \beta E_0$ at $z = -5\ \mathrm{nm}$ and $E_1 - \beta E_0$ at $\mathrm{z} = -15\ \mathrm{nm}$ is as shown in Fig. 5-24(b). It is demonstrated that the reflected wave also corresponds to the near-field model.

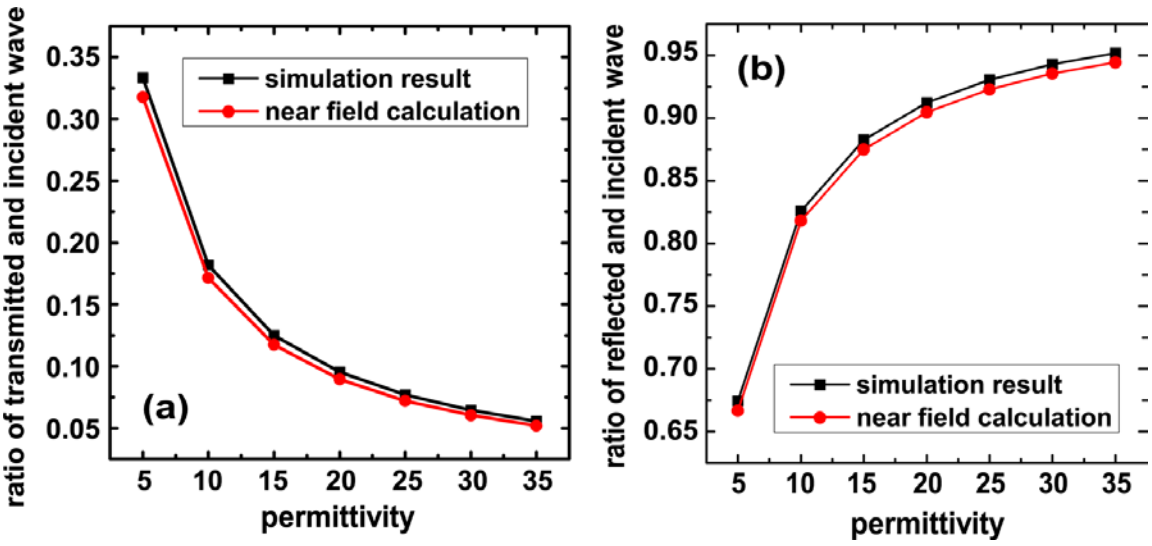

Figure 5-24: The permittivity dependence of the transmitted and reflected wave after correcting the incident wave.

5.6 Summary

The microwave distribution near the tip of the probe was simulated by FEM. The results correspond to the theoretical calculation result based on near-field model rather than plane wave model. The impact of size of aperture, thickness and length of inner conductor on the resolution and sensitivity were also discussed for the improvement of the probes. By analyzing the simulation results of the reflected wave and transmitted wave with different sample permittivity, the enhancement phenomenon of incident wave was discovered. After eliminating the enhancement effect, it was demonstrated that the permittivity dependence of reflected and transmitted microwave can also be successfully described by the near-field model.

References

1) Y. Ju, M. Hamada, T. Kobayashi, and H. Soyama, Microsyst. Technol. **15**, 1195-1199 (2009).
2) A. Hosoi, M. Hamada, A. Fujimoto, and Y. Ju, Microsyst. Technol. **16**, 1233-1237 (2010).
3) B. Tong, T. Hirabayashi, Y. Toku, Y. Morita, and Y. Ju. Non-contact local conductivity measurement of metallic nanowires based on semi-near-field reflection of microwave atomic force microscopy. *Appl. Phys. Express*. (2021) (in press).
4) R. P. Feynman, R. B. Leighton, and M. Sands. The Feynman Lectures on Physics: Mainly Electromagnetism and Matter Vol. 2. *Addison-Wesley, Reading* (1977).
5) D. M. Pozer. Microwave Engineering 2nd ed. *Wiley, New York* (1998).
6) B. Tong, M. Zhao, Y. Toku, Y. Morita, and Y. Ju. Local permittivity measurement of dielectric materials based on the non-contact force curve of microwave atomic force microscopy. *Rev. Sci. Instrum.* **90**, 033706 (2019).

Chapter 6 Conclusions

AFM, one of the most popular scanning probe microscopies, has been a powerful surface detection instrument with nanoscale resolution since its invention. With the development of nanotechnology and molecular biology, rapid, non-destructive measurement methods for various physical properties of nanomaterials and cells have become essential. Therefore, as an excellent measurement platform which has diverse measurement environments and evaluable materials, AFM has been integrated with different measurement techniques. For electrical property, although various functional AFMs have been developed, non-contact quantitative evaluation for intrinsic local permittivity and conductivity of samples have not been realized yet. Therefore, for this target, the studies in this thesis developed M-AFM, which mainly aimed at the expansion of its application and establishment of the theoretical framework for evaluation.

First, on the basis of the previous achievement about conductivity evaluation of bulk metallic material, M-AFM was developed to be applied to permittivity evaluation of dielectric materials. On the other hand, referring to the size of the evaluable sample, it was expanded from bulk samples to nanowire samples. As the experimental setup, two kinds of M-AFM probe were fabricated to meet different requirements. The slit probe has a simpler structure and is easier to be fabricated as designed. Thus, it usually has a higher resolution and is applied to the permittivity evaluation. The coaxial probe, however, has a higher sensitivity because of the more closed structure and no cutoff frequency. It was used for conductivity evaluation which has a smaller signal range. In addition, permittivity evaluation was implemented in non-contact force curve mode to obtain the distance dependence of near-field microwave. Different from dielectric material in which the bounded charge is polarized in different extent according to the permittivity, the free charge in metal can reach the same electrostatic equilibrium state. It makes the reflected microwave from different metals very close and the electric force difference can hardly be evaluated. Therefore, the conductivity evaluation was

implemented by measuring the reflection signal directly under non-contact scanning mode to improve the sensitivity.

As the theoretical basis of quantitative evaluation, the distribution of microwave between the tip and the sample was analyzed based on near-field approximation for both dielectric and metallic materials. In the previous plane wave model, the electric field is considered to be radiation field mutually excited with the magnetic field, and within the range far less than the wave length (near-field condition) the spatial distribution is uniform. In near-field model, the electric field is regarded as a quasi-static field generated by the field source charge on the tip at every instant. Therefore, the field calculated by Coulomb law can describe the spatial distribution. In addition, for metallic materials the reflection coefficient was also considered to establish a semi-near-field model, because thorough near-field model cannot describe the conductivity dependence. Also, the impact of sample shape on the field distribution was also discussed and corrected to apply this model to nanowire samples.

Since it is difficult to verify the theoretical field distribution model within the range of 100 nanometers in experiment, we simulated the probes based on finite element method (FEM). The simulation result of field distribution of both slit probe and coaxial probe correspond to the calculation result based on near-field model. Furthermore, the impact of probe structure on resolution and sensitivity were also studied by simulation. It was found that the aperture size determines the resolution of slit probe and is in no relation with the sensitivity. For coaxial probe, the resolution and sensitivity do not depend on the aperture but depend on the inner conductor. Although theoretically coaxial probe has a higher resolution and sensitivity than slit probe, usually the resolution of slit probe is better because the structure is easier to be fabricated as designed. Finally, the permittivity dependence of reflected wave and transmitted wave were investigated by simulation since the planed wave model and near-field model give different conclusions. After eliminating the enhancement effect, which is also an evidence of near-field charge interaction, the result supports near-field model.

In conclusion, the evaluation method for permittivity of dielectric materials and conductivity of metallic nanowires have been developed for M-AFM. Near-field model,

which can describe the important distance dependence of electric field between tip and sample, have been established and verified by FEM simulation. Through this research, M-AFM is proved to be a promising non-contact quantitative evaluation instrument for local permittivity and conductivity.

Acknowledgement

First of all, I would like to express my deep and sincere appreciation to my supervisor, Prof. Yang Ju, for the chance he provided me to study in this laboratory as a doctor student. His enlightening idea gave me inspiration and opened my mind. He taught me the valuable experience to do research and encouraged me to stick to the end. Even when I made a mistake and met trouble, he also helped me kindly. I would never forget the generous support in daily life, especially when I decided to find a job before getting the degree. I really appreciate Prof. Ju for everything he has done for me.

I would like to express my gratitude to Prof. Kenji Fukuzawa and Masahiro Arai. Thanks them for their professional suggestions on this research to make it more detailed.

I also want to say thanks to Prof. Yasuyuki Morita. When I felt confused, the advice and encouragement from him really helped me a lot. During the year that Prof. Ju was on a visit in Canada, Prof. Morita cared about my study and life as a foreign student, which made me forget the loneliness in a foreign country.

I am very grateful to Lecturer Yuhki Toku. In research, the discussions about details in the regular meetings always helped me timely to overcome the challenges. After research, the friendly free talks improved my Japanese and made me relax. Thanks to Lecturer Toku as my teacher and my friend.

Also, I appreciate the happy time I spent together with all the members in Ju lab, especially with Dr. Keyi Yan, Mr. Minji Zhao, Mr. Takahiro Hirabayashi and Mr. Shaojie Gu. The discussion with Mr. Yan about research, life and future always enriched my knowledge and inspired me a lot. Thanks to Mr. Zhao and Mr. Hirabayashi for their indispensable support and cooperation in research. Mr. Gu gave me great help after I left Ju laboratory for job. I wish everyone of Ju lab all the best.

Last but not least, I would like to thank my family for their patient support and understanding until I can get the degree.